NANO CALCITE ($CaCO_3$) PRODUCTION IN SEMI-BATCH BUBBLE REACTOR

A Thesis Submitted to
the Graduate School of Engineering and Sciences of
İzmir Institute of Technology
in Partial Fulfillment of the Requirements for the Degree of

MASTER OF SCIENCE

in Chemical Engineering

by
Eda ÜLKERYILDIZ

July 2013
İZMİR

We approve the thesis of **Eda ÜLKERYILDIZ**

Examining Committee Members:

Assoc. Prof. Dr. Ekrem ÖZDEMİR
Department of Chemical Engineering, İzmir Institute of Technology

Assist. Prof. Dr. Özgenç EBİL
Department of Chemical Engineering, İzmir Institute of Technology

Assoc. Prof. Dr. Yusuf SELAMET
Department of Physics, İzmir Institute of Technology

08 July 2013

Assoc. Prof. Dr. Ekrem ÖZDEMİR
Supervisor, Department of Chemical Engineering,
İzmir Institute of Technology

Prof. Dr. Fehime ÖZKAN
Head of the Department of
Chemical Engineering

Prof. Dr. R. Tuğrul SENGER
Dean of the Graduate School of
Engineering and Sciences

ACKNOWLEDGMENTS

The present M.Sc. thesis was undertaken at the Chemical Engineering Department of İzmir Institute of Technology (İzmir) and I would like to thank numerous people who became involved in many different ways.

First and foremost, I would like to thank my supervisor, Assoc. Prof. Dr. Ekrem ÖZDEMİR, who offered me this topic and provided me the best scientific support. I am especially grateful to him for his guidance combined with his participation which kept me motivated and always enthusiastic. I'm grateful to Assist. Prof. Dr. Sevgi KILIÇ ÖZDEMİR for her stimulating suggestions, encouragement, helps to complete this thesis.

This study was supported by the Research Council of Turkey, TUBTAK, through the project number 110M104, and I would like to thank TUBITAK for the financial support. In addition, I would like to thank the personnel in the Center for Materials Research of İzmir Institute of Technology, for their guidance, during the characterization of the produced particles.

Sincere thanks go to my sister, Evren ÜLKERYILDIZ and to my best friends, Gizem ACAR, Alper ŞAHİN, Esin GÖKMEN, Burak BAŞDAĞ, Berkin YILMAZ and Alptuğ ELİTEZ for their supports and encouragement. Special thanks go to my lab mates, Derya KÖSE, Sezen Duygu ALICI, Görkem TOPRAK and Umur AYAZ, also my office friends Gizem PAYER, Derya DÜZGÖREN, Emre DEMİRKAYA, Ahmet Uğur ÇİÇEK and Selcan ATEŞ.

My deepest gratitude goes to my parents, Şerife ÜLKERYILDIZ and Şevket ÜLKERYILDIZ, my grandmother, for their never-ending support.

ABSTRACT

NANO CALCITE ($CaCO_3$) PRODUCTION IN SEMI-BATCH BUBBLE REACTOR

Calcium carbonate ($CaCO_3$) has been widely used as filling material in many industries due to its low cost and enhancement in some of the physical properties of the composite materials. The main purpose of this study was to produce $CaCO_3$ particles by carbonation method in nano size, homogeneous size distribution and different morphologies. A semi-batch bubble reactor was designed in order to introduce carbon dioxide (CO_2) into the $Ca(OH)_2$ solution or its slurry with a controlled fashion. Different parameters such as stirring rate, $Ca(OH)_2$ concentration, CO_2 flow rate, and pulse CO_2 injection were examined. Also, jet flow was applied in the stirred tank reactor to prevent particles from aggregation. Conductivity and pH values of solutions were monitored during crystallization. Zeta potential values and average particle size were measured instantly by dynamic light scattering (DLS). Particles produced were separated by centrifugation, dried at 105 ^{o}C in an oven for 1 day, and characterized by the Scanning Electron Microscopy (SEM) for their morphology, and X-Ray diffraction (XRD) for their crystal structures. On the basis of XRD analysis, the main crystal form of precipitated particles was calcite. According to SEM images, elongated chain-like, cubical, and rectangular particles were achieved to be produced with particle size of about 200 nm to 400 nm.

ÖZET

YARI-KESİKLİ GAZ KABARCIK REAKTÖRDE NANO KALSİT ($CaCO_3$) ÜRETİMİ

Kompozit malzemelerin bazı fiziksel özelliklerini geliştirmesi ve düşük maliyeti nedeniyle kalsiyum karbonat ($CaCO_3$) dolgu malzemesi olarak birçok endüstride kullanılmaktadır. Bu çalışmanın temel amacı, karbonizasyon metodu ile ve nano boyutta, homojen boyut dağılımında ve farklı morfolojilerde $CaCO_3$ tanecikleri üretmektir. CO_2 gazının $Ca(OH)_2$ çözeltisi içine kontrollü bir şekilde enjekte edilmesi için yarı kesikli baloncuk reaktörü tasarlanmıştır. Karıştırma hızı, $Ca(OH)_2$ konsantrasyonu, CO_2 gaz debisi ve kesikli CO_2 enjeksiyonu gibi farklı parametreler incelenmiştir. Ayrıca taneciklerin agrege olmalarını önlemek için karıştırılan reaktöre jet akış uygulanmıştır. Kristalizasyon boyunca pH ve iletkenlik değerleri izlenmiştir. Ayrıca taneciklerin zeta potansiyel değerleri ve çözeltinin ortalama tanecik boyutu dinamik ışık saçılımı yöntemiyle anlık olarak ölçülmüştür. Üretilen tanecikler santrifüj yöntemi ile ayrılmış, 1 gün boyunca 105 ^{o}C etüvde kurutulmuş ve Taramalı Elektron Mikroskobu (TEM) ile morfolojik özellikleri, X-ışını kırınım (XRD) ile yapısal özellikleri karakterize edilmiştir. XRD ölçümlerine göre, bu taneciklerin kalsit olduğu anlaşılmıştır. TEM görüntülerine göre, zincir yapıda, kübik ve dikdörtgen şekillerinde, yaklaşık 200 nm ile 400 nm arasında nano taneciklerin üretimi başarılmıştır.

TABLE OF CONTENTS

LIST OF FIGURES

Figure **Page**

LIST OF TABLES

CHAPTER 1

INTRODUCTION

Calcium carbonate ($CaCO_3$) is an inorganic compound occurring in solid sediment in the world. $CaCO_3$ is mostly used as filling material or a pigment in various industries, such as pulp and papers, ceramics, dye, textile, rubber and plastics, cosmetics, biomaterials and magnetics. $CaCO_3$ exists in three crystal structure (polymorph): calcite, aragonite and vaterite. Calcite is the most stable form that has a rhombic structure while aragonite has a dendritic and vaterite has a spherical morphology. $CaCO_3$ finds different usage area in industrial applications depending on properties such as polymorph, particle size, surface area and chemical purity (Domingo, Loste, Gómez-Morales, García-Carmona, & Fraile, 2006; García-Carmona, Morales, & Clemente, 2003; López-Periago, Pacciani, García-González, Vega, & Domingo, 2010). Using filling natural will enhance the physical properties of composite material and decrease the produce cost (Gao, Liu, & Zhang, 2009; Hu, Dong, & Zhen, 2009; Xiaobo Liu, Zou, Cao, & Luo, 2007; Osman, Atallah, & Suter, 2004). For example, as shown in Figure 1.1 (Fu, Feng, Lauke, & Mai, 2008) the tensile yield strength of calcite-polypropylene (PP) composite material was shown to decrease significantly when the particle volume fraction was increased. As the particle size decreased, the decrease in the tensile yield strength was lower. Especially, when the particle size was in 10 nm, the tensile yield strength did not decrease; on the contrary, it was increased with the particle volume fraction. Therefore, it was understood that using nano particles in composite materials would enhance the physical properties of the composite materials.

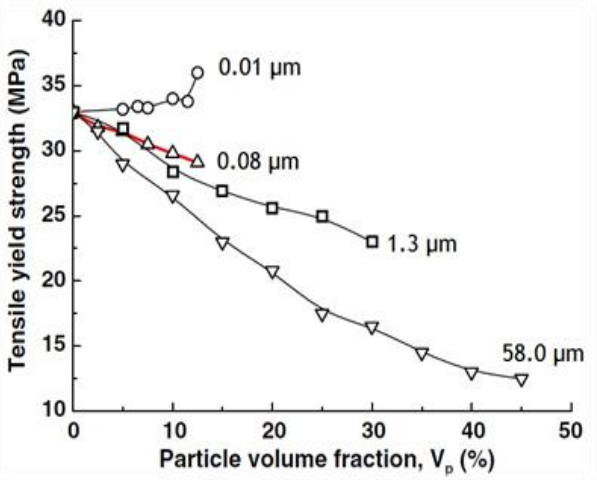

Figure 1.1. Effects of $CaCO_3$ size on strength of calcite-polypropylene composite (Source: Fu et al., 2008).

$CaCO_3$ can be obtained from natural sources by crushing, grinding and sieving processes respectively. However, the particles produced by crushing method were in micron sizes and particle size distribution was obtained as non-homogeneous. Also, these processes could increase the product cost with extra impurities. (Cho, Chang, Kil, Kim, & Jang, 2009; Sant'Anna, Souza, & Araujo, 2008).

Synthesis of $CaCO_3$ particles can be synthesized by two main methods. One of them is chemical method and the other is carbonization method (Domingo et al., 2006; García-Carmona et al., 2003). In chemical method, liquid-liquid reactants are used to produce a solid product, in two methods known as Kraft Pulping Method and Solution Method. For example, the solutions of calcium chloride ($CaCl_2$) and sodium carbonate (Na_2CO_3) are mixed with each other and then precipitated $CaCO_3$ is produced in the solution. However, the $CaCO_3$ product in solution method is produced in micron sizes. (Casanova & Higuita, 2011; Guo, Yu, & Cheng, 2006; Wan et al., 2009). In carbonization method, gas and liquid reactants are used to produce solid product. The solution of calcium hydroxide ($Ca(OH)_2$) is used as Ca^{2+} ion source is reacted with CO_2 gas which is used as CO_3^{2-} ion source. Nano $CaCO_3$ can most easily be produced by the carbonation method.

In carbonation method, reactive crystallization of $Ca(OH)_2$-CO_2-H_2O was experienced by using some different processes such as batch process, sono-chemical process, sol-gel process, reverse microemulsion process and supercritical chemical process. According to reactor type, process parameters such as temperature, stirring rate, supersaturation and the presence of additives, the size and morphology of the

precipitated $CaCO_3$ particles were investigated. Calcite are generally produced by bubbling of CO_2 through a $Ca(OH)_2$ solution (Ariyaprayoon, leela-Adisorn, & Supsakulchaı, 2009; Bastakoti, Guragain, Yokoyama, Yusa, & Nakashima, 2011; Domingo et al., 2006; García-Carmona et al., 2003; Matsumoto, Fukunaga, & Onoe, 2010; Tsutsumi, Nieh, & Fan, 1991; Varma, Chen, & Unnikrishnan, 2011). Although carbonization method has been used extensively for the synthesis of $CaCO_3$, a proven method could not be suggested for the production of calcite in nano size, homogeneous size distribution and different morphologies.

Therefore, the purpose of this study was to produce $CaCO_3$ in nano sizes, homogeneous size distribution and different morphologies.

CHAPTER 2

LITERATURE SURVEY

2.1. Calcite and Calcite Crystal Structure

Calcium carbonate is a well-known inorganic crystal material in nature. The anhydrous crystalline polymorphs of calcium carbonate ($CaCO_3$) are calcite (rhombohedral-scalenohedral structure), aragonite (dendritic- orthorhombic structure) and vatarite (spheroidal- hexagonal structure) (Bots, Benning, Rodriguez-Blanco, Roncal-Herrero, & Shaw, 2012; García Carmona, Gómez Morales, & Rodríguez Clemente, 2003; Varma et al., 2011; Xu, Wang, & Li, 2010). The hydrous crystalline polymorphs of calcium carbonate ($CaCO_3$) are calcium carbonate monohydrate, calcium carbonate hexahydrate (ikaite, $CaCO_3 \cdot 6H_2O$) and amorphous calcium carbonate (Bots et al., 2012; López-Arce, Gómez-Villalba, Martínez-Ramírez, Álvarez de Buergo, & Fort, 2011; Rodriguez-Blanco, Shaw, & Benning, 2008, 2011). Calcite has a trigonal structure due to the trigonal axis of calcium and carbon atoms of carbonate ions as shown in Figure 2.1. The most stable form of $CaCO_3$ is calcite at atmospheric temperature and pressure. Aragonite and vaterite forms are not stable but they can be transferred in the stable form of calcite. (Matsumoto et al., 2010).

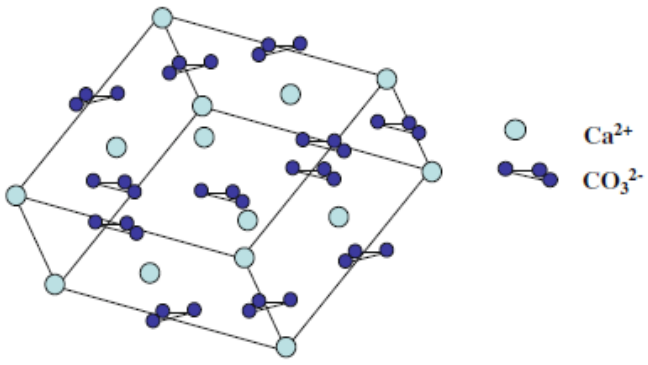

Figure 2.1. Crystalline structure of calcite in rhombic system

(Source: Kadota et al., 2011).

2.2. Usage of $CaCO_3$

According to particle morphology, $CaCO_3$ is used as filling material for a wide range of industrial process such as paper, rubber, paint, magnetic recording, textile, detergent, adhesive, plastic, cosmetic, etc. (Domingo et al., 2006; Wen, Xiang, & Jin, 2003). $CaCO_3$ particles are also used in new areas such as drug release from hollow nanospheres (Bastakoti et al., 2011), biomimetic applications as a biosensor due to the its biocompatible characteristic (Shan, Wang, Xue, & Cosnier, 2009), magnetite nanoparticle applications as a novel magnetically responsive material (Fakhrullin, Bikmullin, & Nurgaliev, 2009).

Although $CaCO_3$ particles in micron size have negative influence on polymeric materials, in submicron or nano size are generally preferred as reinforcing fillers in polymeric materials. For example, in polypropylene (PP) compound, the addition of nano calcite particles provides an increase in impact strength of polymer (Lam, Hoang, Quang, & Kim, 2009; Y. Lin, Chen, Chan, & Wu, 2010; K. Yang, Yang, Li, Sun, & Feng, 2006). The addition of nano calcite particles in high density polyethylene (HDPE) increases impact strength and heat capacity of material (Sahebian, Zebarjad, Khaki, & Sajjadi, 2009; Yuan et al., 2010). $CaCO_3$-polyester amide (PEA) composite material provides a significant rise in mechanical properties and hydrolysis of the polymer (Xiaobo Liu et al., 2007), $CaCO_3$-polystyrene (PS) increases Young's modulus and creep resistance of polymer (Gao et al., 2009). In poly vinyl chloride (PVC), $CaCO_3$ increases the tensile strength and elongation break point of the composite polymer (Hu et al., 2009; Q. Wang et al., 2007). There is a critical particle size of nano particles which is strongly affected the properties of the composite material. The tensile yield strength and the Young's modulus of PP-$CaCO_3$ composite were shown to increase with decreasing particle size of $CaCO_3$ particles (Fu et al., 2008).

2.3. $CaCO_3$ Production Methods

$CaCO_3$ particles can be obtained from natural sources by grinding and crushing processes (Cho et al., 2009) or from recycled materials like alkaline-solid waste such as fly-ash and alkaline paper mill waste (Montes-Hernandez & Renard, 2011). But the resultant products obtained from such processes have not in desired quality and purity (Sant'Anna et al., 2008).

Although there are many production methods of $CaCO_3$ nano-particles in literature, mainly two different methods are used: chemical method and carbonization method (Domingo et al., 2006). In chemical method, liquid-liquid reactants are used to produce solid product as in Kraft Pulping and Solution Methods. For example, the solutions of calcium chloride ($CaCl_2$) and sodium carbonate (Na_2CO_3) are mixed with each other and then precipitated $CaCO_3$ was synthesized in the solution. $CaCO_3$ particles in high quality and purity can be produced by chemical method in homogeneous size distribution. Although chemical method provides an easy to control of parameters and effect of additives, the produced particles were usually in micron sizes and it's difficult to produce particles not in nano sizes (Casanova & Higuita, 2011; Faatz, Gröhn, & Wegner, 2005; Guo et al., 2006; Martos et al., 2010; Wan et al., 2009). In carbonization method, gas-liquid reactants are contacted with each other to produce solid product. The solution of calcium hydroxide ($Ca(OH)_2$) or calcium chloride ($CaCl_2$) is used as Ca^{2+} ion source and CO_2 gas is used as CO_3^{2-} ion source. These two methods and the resulting products were summarized in Figure 2.2.

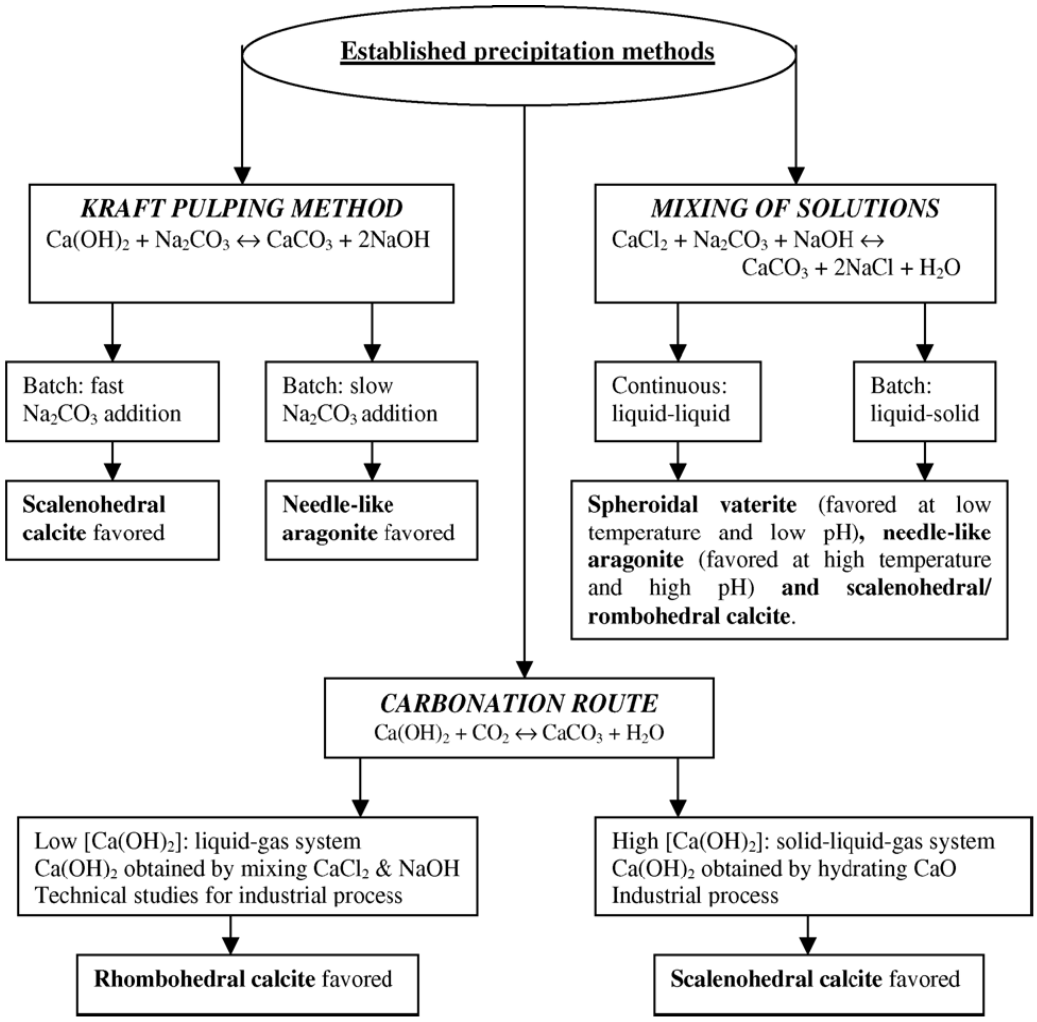

Figure 2.2. Main production methods of precipitation of $CaCO_3$ powders (Source: Domingo et al., 2006).

Carbonization method is a conventional method due to the low cost and availability of raw materials. Industry, carbonization method is the unique way to synthesize $CaCO_3$ particles in nano size with homogeneous size distribution (Ariyaprayoon et al., 2009; Domingo et al., 2006; Gu, Bousfield, & Tripp, 2006; López-Periago et al., 2010; Wen et al., 2003).

2.4. Types of Carbonization Methods

There are many carbonation methods to prepare nanoparticles reported and developed in the literature. They could be classified as reactive crystallization processes (J.-F. Chen, Wang, Guo, Xin-Ming, & Zheng, 2000; Matsumoto et al., 2010; Sun et al., 2011; Varma et al., 2011), sono-chemical processes (López-Periago et al., 2010; S. H. Sonawane et al., 2008), sol-gel processes (Plank et al., 2009), reverse-microemulsion processes (Kang, Hirasawa, Kim, & Choi, 2005; Tai & Chen, 2008) and supercritical chemical processes (López-Periago et al., 2010; Montes-Hernandez & Renard, 2011).

In reactive crystallization processes, $Ca(OH)_2$-CO_2-H_2O multiphase system is used to produce $CaCO_3$ nanoparticles. The mechanism of CO_2 transport to the gas–liquid interface, process parameters like temperature, concentration of reactants, stirring rate have been investigated by many researches. Also, mass transfer and crystal growth were tried to be controlled to obtain nanocrystal (R.-y. Lin, Zhang, & Bai, 2006).

In sonochemical process, ultrasonic agitation is used to obtain high conversion from $Ca(OH)_2$ to precipitated $CaCO_3$ particles. While reaction is continuous at high temperature and pressure, formation of a layer of $CaCO_3$ on the surrounding of the $Ca(OH)_2$ particles causes Ca^{2+} diffusion limitation. This limitation can be overcome by using different type of stirrer and different stirring rates. A sonicator probe is used with a gas distribution probe in reactor. Ultrasonic agitation application provides an efficient way of enhancing mass transfer between reactants. Also smaller particles were obtained in short times (López-Periago et al., 2010).

In sol-gel process, $CaCO_3$ particles were synthesized by reacting calcium oxide with carbon dioxide in the presence of methanol. The resulting product was alcogel. Then, it was dried with supercritical carbon dioxide to produce $CaCO_3$ aerogel. $CaCO_3$ aerogel formation was a three-step proces; primary $CaCO_3$ nanoparticles formation (5-20 nm), secondary particle formation by growing primary particles (spherical or fibre-like) and aggregation to the $CaCO_3$ gel (Plank et al., 2009).

In reverse microemulsion system, CO_2 was dissolved in an organic phase and diffused into the reverse micelles in the presence of $Ca(OH)_2$, then $CaCO_3$ particles were occured at the supersturation. The nucleation and growth took place during the formation of new $CaCO_3$ particles in the micelles (Tai & Chen, 2008).

In supercritical chemical system, accelerated carbonation process was achieved to obtain high yield $CaCO_3$ particles in a narrow particle size distribution by using supercritical carbondioxide ($scCO_2$)(López-Periago et al., 2010).

Among those, reactive precipitation was found to be a more useful technique industrially due to its low cost and suitability for the large scale processes. Reactive precipitation processes can be occurred in different ways according to reactor type. Typically, crystallization reactor which consists of constant temperature bath, a mixer, an electrical conductivity cell, a controller and a personal computer provided with a software (Kadota et al., 2011; R.-y. Lin et al., 2006; Ukrainczyk, Kontrec, Babić-Ivančić, Brečević, & Kralj, 2007). $Ca(OH)_2$ was suspended in distilled water and filled into the reactor. While $Ca(OH)_2$ solution was mixed, the temperature of aqueous suspension was controlled to reach the targeted temperature. After CO_2 injection into the reactor was started, crystallization was initiated. The pH and conductivity were monitored during the reaction with a pH and conductivity probe. CO_2 injection was continued to complete the reaction. Conductivity and pH values were started to decrease at this time. The reaction was stopped when the conductivity and pH were reached to near 0 mS/cm and 7, respectively. Precipitated $CaCO_3$ particles were separated and dried to analyze. The pH and conductivity were measured to control the reaction, SEM images were taken in order to observe morphology of particles, XRD patterns of produced material was analyzed in order to determine crystal composition, particle size distribution and zeta potential were measured to observe size and electric double layer around the particles. Some results and analysis were seen in Figure 2.3 (Kadota et al., 2011). As shown in the figure, at the beginning of the reaction, the sizes of crystals grows while conductivity slightly decreases. At the same time, pH nearly constant while zeta potential strongly increases. Then particle size continues to increase and zeta potential starts to decrease when the conductivity reached to near 7 mS/cm. At this time, very rapid reaction was observed. The crystallization was completed when the conductivity and pH reached to near 0 mS/cm and 7, respectively.

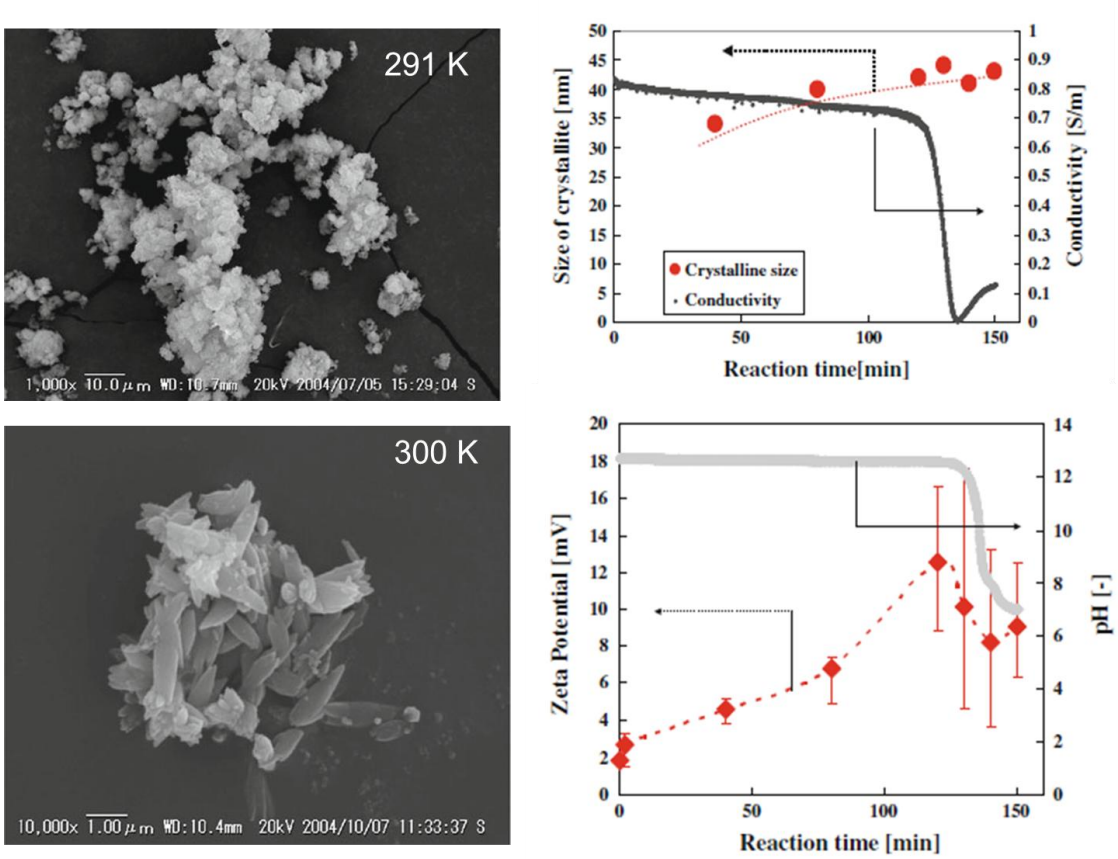

Figure 2.3. The change of particle size - conductivity and pH – zeta potential of particles during the reaction. SEM images represent the final product of reaction. (Source: Kadota et al., 2011).

Although there are many steps in $CaCO_3$ crystallization process, reaction mechanism can be divided into three steps. Namely, dissolution of $Ca(OH)_2$, CO_2 absorption in water and the reaction between Ca^{2+} and CO_3^{2-} ions (Montes-Hernandez, Fernández-Martínez, Charlet, Tisserand, & Renard, 2008; Varma et al., 2011).

1- Dissolution of $Ca(OH)_2$

$$Ca(OH)_{2(aq)} \longrightarrow Ca^{2+} + 2OH^-$$

2- CO_2 absorption in water

$$CO_{2(aq)} + H_2O \longrightarrow CO_3^{2-} + 2H^+$$

3- The reaction of Ca^{2+} and CO_3^{2-}

$$Ca^{2+} + CO_3^{2-} \longrightarrow CaCO_3^{o}{}_{(s)} \text{ (nuclei)}$$

$$CaCO_{3(s)} \text{ (nuclei)} \longrightarrow CaCO_{3(s)} \text{ (calcite)}$$

As soon as $Ca(OH)_2$ solid particles were dissolved in water Ca^{2+} and OH^- ions diffuse into the liquid film layer. On the other hand, CO_2 gas is diffused into liquid film layer from the gas film layer. This step is the slowest step and determines the reaction rate. After the dissolution at gas – liquid interface, CO_2 gas becomes CO_3^{2-} along with $2H^+$ ions were released into the liquid phase neutralizing $2OH^-$ ions released from the $Ca(OH)_2$ solution. The Ca^{2+} ions react with the CO_3^{2-} ions to form the $CaCO_3^{o}$ nuclei. Then, these primary $CaCO_3^{o}$ clusters constitute stable calcite crystals (R.-y. Lin et al., 2006). The overall reaction can be given as follows;

$$Ca(OH)_{2(aq)} + CO_{2(aq)} \longrightarrow CaCO_{3(s)} + H_2O_{(aq)}$$

In gas–liquid reactive crystallization process, the solution must be supersaturated to obtain a driving force between the ions for penetration. Supersaturation provides absorption of ions and chemical reaction for precipitation by overcoming gas-side and liquid-side resistances. It is possible to get calcite precipitates with desired morphology and size, by a perfect control of gas-side and liquid-side resistances. For that reason the key parameter of reactive crystallization process is to control the contact area and the contact time between the gas and liquid phases (Varma et al., 2011).

2.5. Reactors Used in $CaCO_3$ Production

The reactive crystallization reactors were fundamentally designed according to the control of parameters affecting the morphology and size of particles. These parameters could be temperature, concentration (or supersaturation of $Ca(OH)_2$), CO_2 flowrate and CO_2 percentage in the gas mixture, molar ratio of the reactants, strirring rate, stirring type, presence of additives, impurities, and presence of modifiers (Ukrainczyk et al., 2007). In order to optimize these parameters, many different rectors were used for nano $CaCO_3$ particle synthesis. Some of these were High Gravity Rotating Reactor (HGRR) (J.-F. Chen et al., 2000; Sun et al., 2011; Varma et al., 2011), Coutte-Taylor Reactor (Jung, Kang, Kim, & Choi, 2000), Hyrodynamic Cavitation Reactor (Shirish H. Sonawane et al., 2010), Microporous-dispersion reactor (Jiang et al., 2011; Wu, Wang, Zhu, & Wang, 2007) and Semi-batch Bubble Reactor (Kadota et al., 2011; Kontrec, Ukrainczyk, Babić-Ivančić, & Kralj, 2011; Matsumoto et al., 2010; Ukrainczyk et al., 2007).

High Gravity Rotating Reactor (HGRR) which is shown in Figure 2.4 was used to minimize the contact area for the mass transfer between the gas and liquid reactants. Control of contact area and contact time of reactants and the turbulent flow in the reactor will provide to synthesis of nano $CaCO_3$ particles by inhibiting crystal agglomeration with a shear force. This system is not suitable for industry due to the high electrical consumption and high cost.

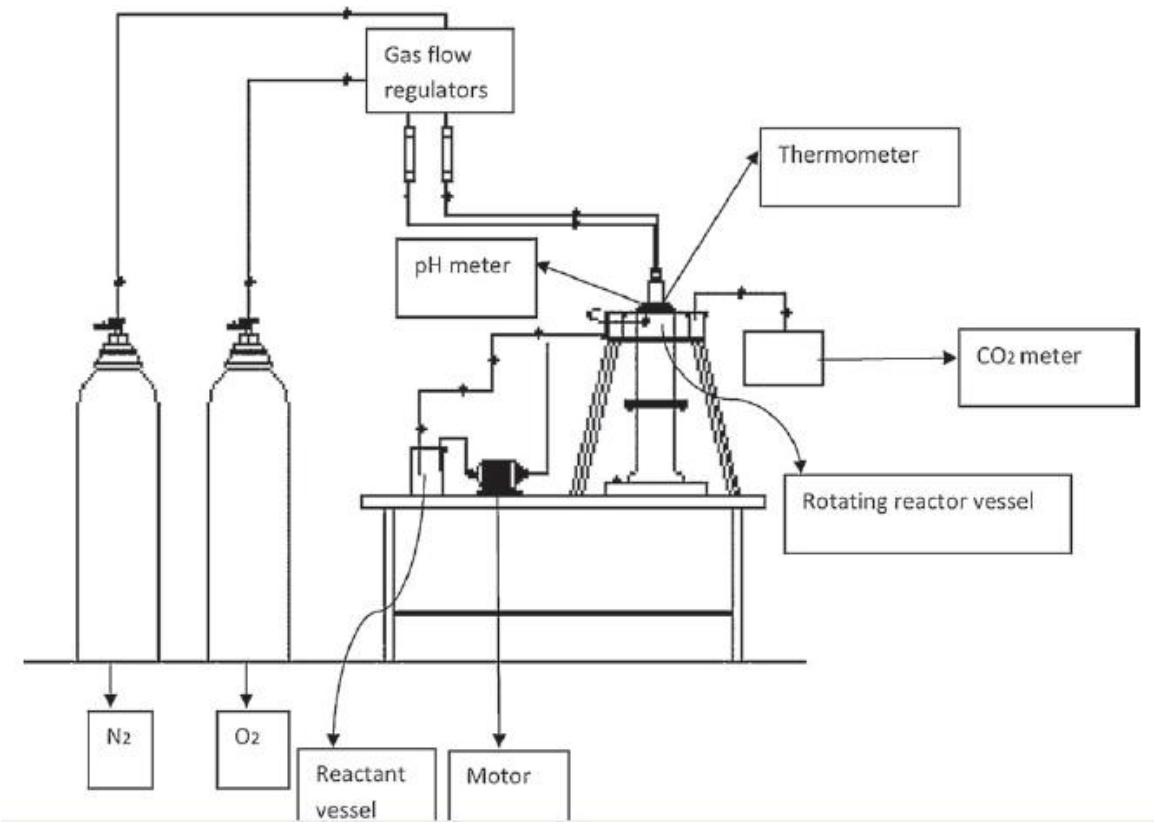

Figure 2.4. A High Gravity Rotating Reactor
(Source: Varma et al., 2011).

The Microporous-Dispersion Reactor was shown in Figure 2.5. It was used to disperse the gas phase into the flowing or static continuous liquid phase by pressure through a micropore membrane. The micropore materials can be a metal or organic membrane and sintered on a ceramic or glass plate. Mass transfer between the reactants is controlled by small bubbles which offer a greater area of exposed gas–liquid system, improving the mass transfer coefficient and enhancing the mixing and reaction rates (Wu et al., 2007).

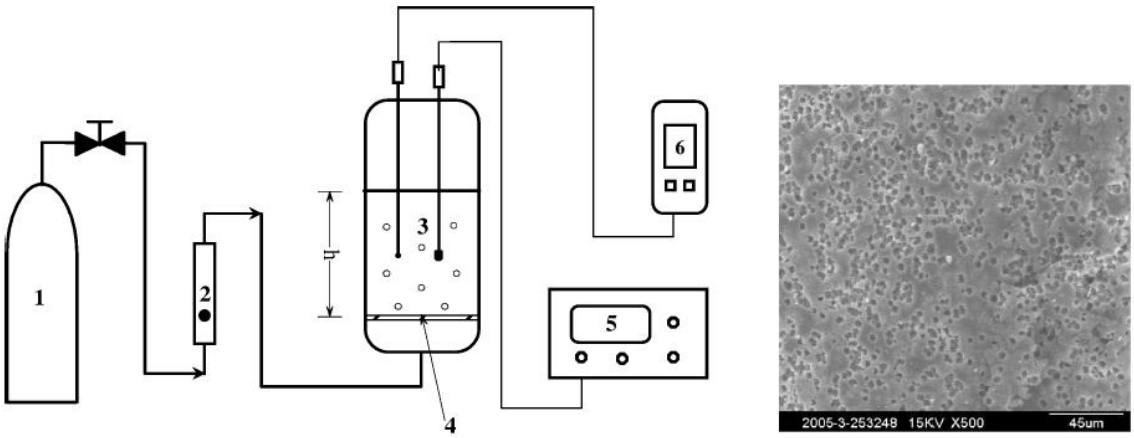

Figure 2.5. Shematic illustration of A Microporous-Dispersion Reactor. (1)Mixed gas, (2)Flow-meter, (3)Microporous dispersion reactor, (4)Microporous plate (as seen in SEM image), (5)Electrical conductivity meter, (6)pH meter (Source: Wu et al., 2007).

In order to produce monodisperse nano size $CaCO_3$ particles, mass transfer between the reactants can be controlled by the small bubbles in a Semi-batch Bubble Reactor as shown in Figure 2.6. This reactor was used in gas-liquid reactive crystallization processes (Varma et al., 2011).The micron-scale bubble generation is also called as micromixing technique. In $Ca(OH)_2$-CO_2-H_2O multiphase carbonization system, this technique provides to maintain perfect mixing and a rapid mass transfer between reactants. The size of bubbles is the most important parameter to influence on mass transfer and reactive absorption. Minimizing of bubble size provides an increase in the gas–liquid interfacial area, an increase residence time of the bubbles with decreasing lifting force and interactions at the gas–liquid interface due to the electric charge on the bubble surface (Matsumoto et al., 2010).

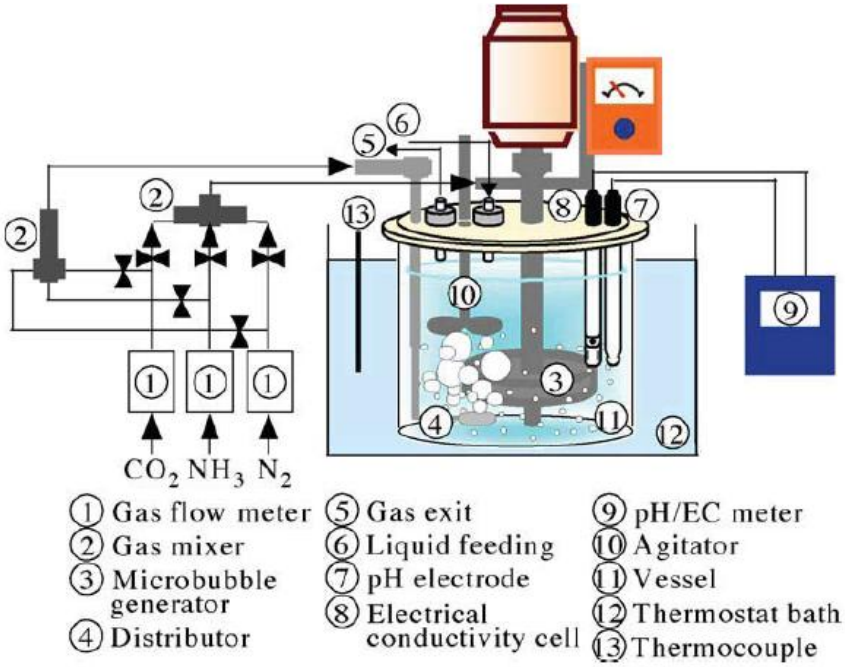

Figure 2.6. Semi-batch (or semi-continuous) Bubble Reactor.
(Source: Matsumoto et al., 2010).

The SEM images of $CaCO_3$ particles obtained from a high gravity rotating reactor, a microporous-dispersion reactor and semi-batch (or semi-continuous) bubble reactor were shown in Figure 2.7. As shown in the figure, all particles were produced in nano size (~50 nm) with homogeneous size distribution. For this purpose, production of nano calcite particles is possible by using bubble reactor in low process cost.

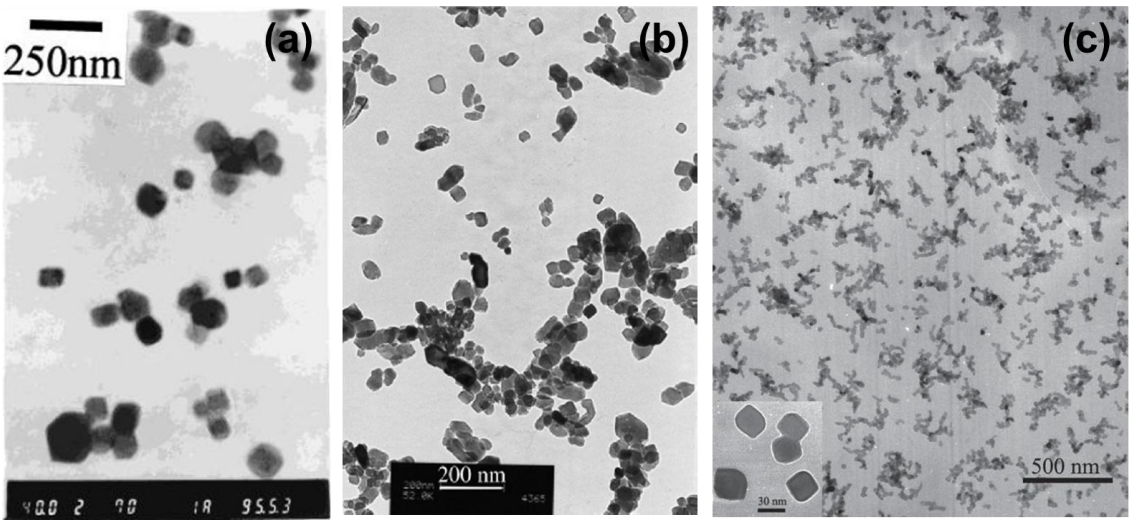

Figure 2.7. Precipitated calcite particles produced from (a) A High Gravity Rotating Reactor. (Source: J.-F. Chen et al., 2000), (b) Microporous-Dispersion Reactor. (Source: Wu et al., 2007) and (c) Bubble Reactor. (Source: Hari et al., 2006).

2.6. $CaCO_3$ Production in Bubble Reactor

There are parameters affecting directly or indirectly the particle size and morphology in bubble column reactor. The particle morphology of $CaCO_3$ particles depends directly on the temperature, supersaturation of $Ca(OH)_2$, CO_2 flowrate, bubble size, stirring rate of slurry and the presence of additives. Additives can be used as two different purposes in the slurry; inhibit the crystal growth, and to modify the particle morphology (Guo et al., 2006).

The crystallization temperature is a very important parameter for determining the polymorph of $CaCO_3$ particles. While fine rhombic calcite particles were obtained at 291 K in a range from 100 nm to 200 nm, spindle granular particles were obtained with a length of 1.0–1.5 μm and a width of 0.3–0.5 μm at 300 K (Kadota et al., 2011). Also, rhombohedral-calcite particles (1 μm) were produced at 35 ^{o}C, spindle granular particles (0.5 μm) were produced at 45 ^{o}C (Kontrec et al., 2011). Rhombohedral-spherical particles (0.3–0.5 μm) were produced at 20 ^{o}C, rhombohedral- truncated prismatic particles (1 μm) were produced at 35 ^{o}C and scalenohedral particles (1–1.5 μm) were produced at 50 ^{o}C (Ukrainczyk et al., 2007).

CO_2 flow rate or molar ratio is another important parameter to influence the morphology of the particles. While spindle-like aggregated particles (0.2–0.8 μm) were obtained at 5 dm^3/min of CO_2 flow rate, rhombohedral cubic individual particles (0.2 μm) were obtained at 0,3 dm^3/min of CO_2 flow rates (Ukrainczyk et al., 2007). Besides, fine rhombic calcite particles (100 to 200 nm) were produced at a CO_2 flow rate of 10 L/min; spindle granular particles were obtained with a length of 1.0–1.5 μm and a width of 0.3–0.5 μm at CO_2 flow rate of 2 L/min (Kadota et al., 2011). In another study, specific surface area of produced ultrafine particles was decreased when CO_2 flow rate was increased (Wu et al., 2007). Additionally, CO_2 in the gas phase was injected into the slurry at varying percentages in N_2 gas such as 20 %, 30 %, 33.3 % and 50 % to control the CO_2 within the reactor (X. Chen et al., 2010; Hari et al., 2006; Kadota et al., 2011; Sun et al., 2011).

In the bubble reactor, the crystallization between gas and liquid reactants was influenced by CO_2 gas bubble size considering that reaction occurred at the bubble surface. Because of this reason, bubbles size was an important parameter for bubble reactor. Minimizing of bubble size provided an increase in the gas–liquid interfacial area, which caused to produce particles with different morphologies. For example, while vaterite and aragonite were obtained as dominant product from 40 μm bubble size of CO_2-N_2-NH_3 mixture; calcite and vaterite were obtained as dominant product from 2000 μm bubble size of CO_2-N_2-NH_3 mixture (Matsumoto et al., 2010). In another study, hollow and large (5 μm) calcite and aragonite particles were produced from 10 μm bubble size of CO_2 gas (Hadiko, Han, Fuji, & Takahashi, 2005). For the minimization of particle size, bubble size should be decreased.

The morphology and size distribution of particles were influenced mostly by the $Ca(OH)_2$ concentration and supersaturation of the system (Ukrainczyk et al., 2007). While rhombohedral fine particles (50 nm) were obtained with 0.01 mol/L $Ca(OH)_2$; rhombohedral aggregated particles (1 μm) were obtained with 0.2 mol/L $Ca(OH)_2$ (Ariyaprayoon et al., 2009). And also, rhombohedral-scalenohedral particles (0.03–0.5 μm) were obtained with 3,7 mM $Ca(OH)_2$; rhombohedral-spindle-like particles (1–1.5 μm) were obtained with 11,11 mM $Ca(OH)_2$ solution (Ukrainczyk et al., 2007).

In order to produce nano calcium carbonate particles, some additives were used as dispersion agents to control the particle size. These control agents must be flexible, highly charged molecules and may have selective electrostatic interactions for providing a driving force for adsorption. This range was given from electrostatic to highly specific

recognition of crystal faces caused by structural and stereochemical compatibility (Varma et al., 2011). Recently, polyacrylic acid, oleic acid, stearic acid, phosphonic acids, poly(ethylene oxide)–poly(propylene oxide)–poly(ethylene oxide), heparin, ethylene glycol, mono-ethylene glycol, anionic and ionic dextran, pesticide validamycin, a solid ionic liquid, EDTA, lecithin liposome are used as an organic template to control the nucleation and growth of particles (C. Y. Chen, Xia, & Wang, 2010; Flaten, Seiersten, & Andreassen, 2010; Ibrahim et al., 2012; Jiang et al., 2011; Konopacka-łyskawa & Lackowski, 2011; Kontrec et al., 2011; Q. Liu, Wang, & Xiang, 2008; XinRong Liu, Zhu, Shao, & Yang, 2010; Qian et al., 2010; Wan et al., 2009; X. Yang et al., 2009; Ye & Chen, 2011).

In order to obtain novel particles, some modifiers were also used to produce new product for new usage areas. Hollow $CaCO_3$ nanospheres which have advantages of light weight, and have unique optical properties as filler and have the capability of encapsulating materials such as nutrition or drugs, were produced by adding poly (styrene, acrylic acid, ethylene glycol) for using in drug release due to the biocompatibility of $CaCO_3$ (Bastakoti et al., 2011; Watanabe et al., 2009). Nano hydrophobic $CaCO_3$ which is a significant building block of natural hard tissues such as bones and teeth and also have excellent properties in paints, inks, papers and plasticizers, were produced by stearic acid at room temperature via carbonization method in the presence of polyethylene glycol phosphate (X. Chen et al., 2010). In another study, hydrophobic $CaCO_3$ production could be achieved by dodecanoic acid or oleic acid and heptadecafluorodecyl-trimethoxysilane via chemical method (C. Wang, Piao, Zhai, Hickman, & Li, 2010; Xu et al., 2010). Magnetically responsive $CaCO_3$ microcrystals were produced by co-precipitation of calcium carbonate in the presence of citrate-stabilized iron oxide nanoparticles (Fakhrullin et al., 2009).

The comparisons of recent studies according to some parameters were summarized in Table 2.1. As shown in the table, fine rhombic and cubic calcite particles could be produced at low temperatures without using any additives in bubble reactor.

Table 2.1. Summary of recent studies for nano calcite production by a bubble reactor.

Production method	**Reactor**	**Additives**	**Temperature**	**Product**	**Reference**
$Ca(OH)_2$-CO_2-H_2O %100 CO_2	Bubble Column Reactor	- Citric acid - Sodium metaphosphate - Polyacrylic Acid	25 ^oC- 35 ^oC	Aggregated cubic calcite (130 nm-40 nm)	(Varma et al., 2011)
$Ca(OH)_2$-CO_2-H_2O %20 CO_2+%80 N_2	Bubbling gas mixture though aqueous slurry	Dextran (anionic and ionic)	35 ^oC- 45 ^oC	Spindle-like + aggregated cubic calcite (80 nm- 10 nm)	(Sun et al., 2011)
$Ca(OH)_2$-CO_2-H_2O %30 CO_2+%70 N_2	Semi-batch Bubble Column Reactor	-	18 ^oC- 27 ^oC	Fine rhombic calcite at low temperature, Large spindle calcite at high temperature (100 nm-200 nm)	(Kadota et al., 2011)
$Ca(OH)_2$-CO_2-H_2O $CO_2/NH_3/N_2$ mix	Semi-batch Bubble Reactor	Nitric acid (HNO_3) Ammonia hydroxide (NH_4OH)	25 ^oC	Calcite Vaterite Aragonite	(Matsumoto et al., 2010)
Pure $Ca(OH)_2$-CO_2-H_2O CO_2/ N_2 =1:2 (molar)	Bubbling gas mixture though aqueous slurry	Stearic acid (SA) Polyethylene glycol phosphate (PGP)	At room temperature 22 ^oC	Nano-chain and Nano-rod $CaCO_3$ particles (40 nm)	(X. Chen et al., 2010)
$Ca(OH)_2$-CO_2-H_2O Air	Bubbling air though aqueous slurry	-	At room temperature 22 ^oC	Tiny rhombohedral calcite (1 μm)	(Ariyaprayoon et al., 2009)

(cont. on next page)

Table 2.1. (cont.)

$CaCl_2$-CO_2-H_2O pure CO_2	Bubbling gas mixture though aqueous slurry	-	17 ^oC- 28 ^oC	Hollow-spherical $CaCO_3$ particles (1 μm)	(Watanabe et al., 2009)
$Ca(OH)_2$-CO_2-H_2O CO_2/N_2 mix	Semi-continuous bench scale bubble reactor	-	20 ^oC- 35 ^oC- 50 ^oC	Calcite at low temperature, spindle-like calcite at high temperature (0.02 μm- 2 μm)	(Ukrainczyk et al., 2007)
Pure $Ca(OH)_2$-CO_2-H_2O CO_2/N_2=1:3 (volumetric)	Bubbling gas mixture though aqueous slurry	-	At room temperature 22 ^oC	Monodispersed cubic calcites (30-26 nm)	(Hari et al., 2006)
$CaCl_2$-CO_2-H_2O pure CO_2	Bubbling CO_2 gas though aqueous slurry	NH_3 $MgCl_2$ HCl	27 ^oC	Hollow calcite and vaterite (5 μm)	(Hadiko, Han, Fuji, & Takahashi, 2006)
$CaCl_2$-CO_2-H_2O pure CO_2	Bubbling CO_2 gas though aqueous slurry	NH_3	27 ^oC	Hollow calcite and vaterite (5 μm)	(Hadiko et al., 2005)
$Ca(OH)_2$-CO_2-H_2O	Bubble Column with outer jacket	-	25 ^oC	Plate- like calcite (2.5 μm)	(Wen et al., 2003)

2.7. Mechanism of $CaCO_3$ particle formation

Although many researchers have been trying to find a $CaCO_3$ crystallization mechanism, there has not been suggested a certain formation mechanism as of today. There are an extensive research have been conducted on this topic. Some mechanisms suggest that there are mainly three steps in $CaCO_3$ formation mechanism; nucleation by ionic attachments and crystal growth. At the beginning of the precipitation ionic attachments of Ca^{++} and $CO_3^{=}$ occurs and creates ionic clusters due to the mass transfer between reactants and primary particles. The number of clusters increases by time and

agglomerated clusters merges to produce $CaCO_3$ nuclei. After the nucleation, particles grow and stable $CaCO_3$ crystals are produced (Domingo et al., 2006).

According to the classical crystallization theory, nucleated clusters will occur by the ions and they produce the nucleus. When these nucleuses reach a critical size, the crystal structure starts to form and grow by adding new ions into the crystal structure. $CaCO_3$ nucleuses are not stable and they can be oriented in a certain direction to form crystals (Gebauer, Volkel, & Colfen, 2008). But, the classical theory was replaced by a novel theory. According to the recent theory, amorphous crystalline particles occur before the crystallization. Crystallization takes place over ionic clusters. Also, stable nucleus is formed in nano sizes. They come together by time and became larger aggregates. These elongated structure reoriented in the aggregated lattice and converted into the crystal from (Gebauer et al., 2008).

The growth rate of $CaCO_3$ crystals is highly depended on the activity ratio of ions solution, which corresponds to the solubility value in equilibrium, defined as Ca^{2+}/CO_3^{2-}. The ratio of ions is directly depends on the relative attachment of ions in the lattice onto growth sites at the crystal surface (Wolthers, Nehrke, Gustafsson, & Van Cappellen, 2012). For example, excess Ca^{2+} species ($Ca^{2+}/CO_3^{2-} > 1$) lead to poor conversion as well as the production of agglomerated particles as a result of the small amount of dissolved CO_2 needed to produce CO_3^{2-} ions and the available Ca^{2+} ions from the $Ca(OH)_2$ dissolution in water (Ibrahim et al., 2012)**.**

It was believed in this thesis that the growth of particles could be inhibited and $CaCO_3$ particles could be produces in a semi-batch stirred bubble reactor in nano sizes, homogeneous size distribution and different morphologies.

CHAPTER 3

MATERIALS AND METHODS

3.1. Materials

Chemicals such as calcium hydroxide ($Ca(OH)_2$), calcium carbonate ($CaCO_3$) were purchased from Merck. $Ca(OH)_2$ was purchased with a purity of 96 % of which 3 % was $CaCO_3$ and 1 % was other impurities (mainly % 0.05 of Na, K, Fe, Sr; % 0.5 of Mg; % 0.01 of $SO4^{=}$, and % 0.005 of Cl^{-}). Calcium carbonate ($CaCO_3$) was purchased with a purity of 98.5 %-100.5 %. Sodium chloride (NaCl) was purchased from Sigma Aldrich with a purity of 99 %. CO_2 gas was purchased from Güneş Gas AŞ, Turkey, with a purity of 99.99 %. Deionized water (DI) was obtained with a MilliQ (Millipore-Elix UV5/ Milli-Q) water purification system to a purity of 18.2 μohm at 25 ^{o}C.

3.2. Methods

3.2.1. Stability Study of $CaCO_3$ in $Ca(OH)_2$

The dissolution of $Ca(OH)_2$ and $CaCO_3$ were conducted in a tree neck reactor at room temperature as shown in Figure 3.1. Conductivity and pH values were measured by Thermo Orion 5 star pH meter with pH and conductivity probes. All data were saved and monitored with a Thermo Star Neviagator 21 software program. Initially, 250 mL of DI water were placed in the three neck reactor and stirred at 550 rpm on a magnetic stir bar. Both pH and conductivity were monitored for about 15 min. Then, a 0.0185 g of $Ca(OH)_2$ were added in the pure water in order to prepare a 1 mM of $Ca(OH)_2$ solution. Both pH and conductivity were monitored during the dissolution for about 30 min. In about 15 min of stirring, about 1 ml of sample were withdrawn from the solution into a UV cuvette and size and size distribution were measured with a particle size analyzer (Malvern ZS model). A 1 ml of sample was also withdrawn from the solution into a zeta cell and zeta potential values were obtained. At least three

measurements were conducted on the same sample and reported their average value. In order to increase the $Ca(OH)_2$ concentration, a 0.037 g, 0.0375 g, 0.092 g, 0.092 g, 0.093 g, 0.185 g, 0.371 g, and 0.926 g of $Ca(OH)_2$ powder were added subsequently into the solution to obtain 3 mM, 5 mM, 10 mM, 15 mM, 20 mM, 30 mM, 50 mM, and 100 mM of $Ca(OH)_2$ solutions, respectively. At the end of each addition, both particle size distribution and zeta potential measurements were conducted.

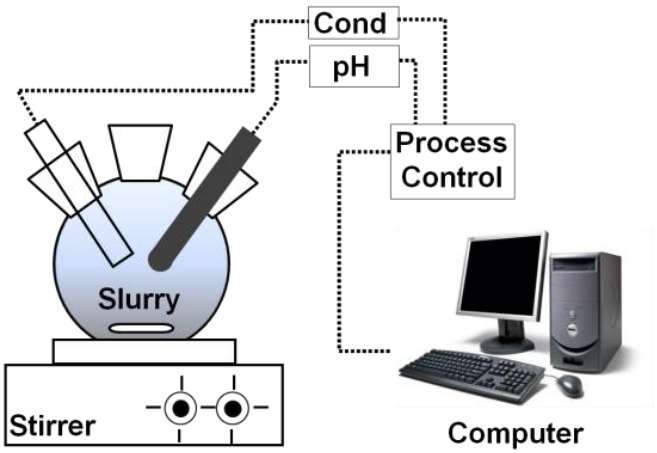

Figure 3.1. A of three neck glass reactor for the stability study of $CaCO_3$ in $Ca(OH)_2$ solution.

The same procedure was conducted for the dissolution of $CaCO_3$: A 250 ml of DI water were placed in the three neck reactor and stirred at 550 rpm on a magnetic stir bar. Both pH and conductivity values were monitored on-line with the software of Thermo Orion pH-meter. Then, a 0.025 g of $CaCO_3$ powder was added to the DI water to obtain a 1 mM of $CaCO_3$ solution. After about 15 min of stirring, a 1 ml of sample was withdrawn to measure the particle size distribution and another 1 ml of sample was withdrawn from the reactor to conduct the zeta potential measurements. In order to increase the $CaCO_3$ concentration, a 0.05 g, 0.05 g, 0.125 g, 0.125 g, 0.125 g, 0.250 g, 0.501 g, and 1.151 g of $CaCO_3$ powder were added subsequently into the solution to prepare a 3 mM, 5 mM, 10 mM, 15 mM, 20 mM, 30 mM, 50 mM, and 100 mM $CaCO_3$ solutions, respectively.

The dissolution of $CaCO_3$ in 10 mM of $Ca(OH)_2$ were conducted with the same procedure. Initially, a 10 mM of $Ca(OH)_2$ solution were prepared by adding 0.185 g of $Ca(OH)_2$ powder into a 250 ml of DI water by stirring at 550 rpm on a magnetic stir bar. Both pH and conductivity values were monitored. After equilibration, both particle size

distribution and zeta potential values were measured with the Malvern zeta sizer by withdrawing 1 ml samples for each. Then, a 0.1 g of $CaCO_3$ powder were added into the solution to obtain a 4 mM of $CaCO_3$ solution in 10 mM of $Ca(OH)_2$ solution. Both pH and conductivity values were monitored. After about 15 min, both particle size distribution and zeta potential were measured by withdrawing a 1 ml of samples for each. Subsequently 0.1 g of $CaCO_3$ powders were added into the solution in order to prepare a 8 mM, 12 mM, and 16 mM of $CaCO_3$ solutions, respectively, containing 10 mM of $Ca(OH)_2$ solution.

The dissolution of $Ca(OH)_2$ in 10 mM of $CaCO_3$ solution were also conducted with the same procedure. Initially, a 10 mM of $CaCO_3$ solution was prepared by adding 0.25 g of $CaCO_3$ powder into a 250 ml of DI water by stirring at 550 rpm on a magnetic stir bar. Both pH and conductivity values were monitored. After equilibration, both particle size distribution and zeta potential values were measured with the Malvern zeta sizer by withdrawing 1 ml samples for each. Then, a 0.1 g of $Ca(OH)_2$ powder was added in the solution to obtain a 5.41 mM of $Ca(OH)_2$ solution in 10 mM of $CaCO_3$ solution. Both pH and conductivity values were monitored. After about 15 min, both particle size distribution and zeta potential were measured by withdrawing a 1 ml of samples for each. Subsequently a 0.1 g of $Ca(OH)_2$ powder was added into the solution in order to prepare a 10.8 mM, 16.21 mM, and 21.62 mM of $Ca(OH)_2$ solutions, respectively containing 10 mM of $CaCO_3$ solution.

3.2.2. Effect of CO_2 Injection Levels

$CaCO_3$ crystallization was conducted in a stirred tank reactor by bubbling the CO_2 through the $Ca(OH)_2$ solution as shown in Figure 3.2. Both pH and conductivity were monitored by Thermo Orion 5 star pH meter with a pH and conductivity cell, respectively. All data were saved during the reactions with Thermo Star Neviagator 21 software program.

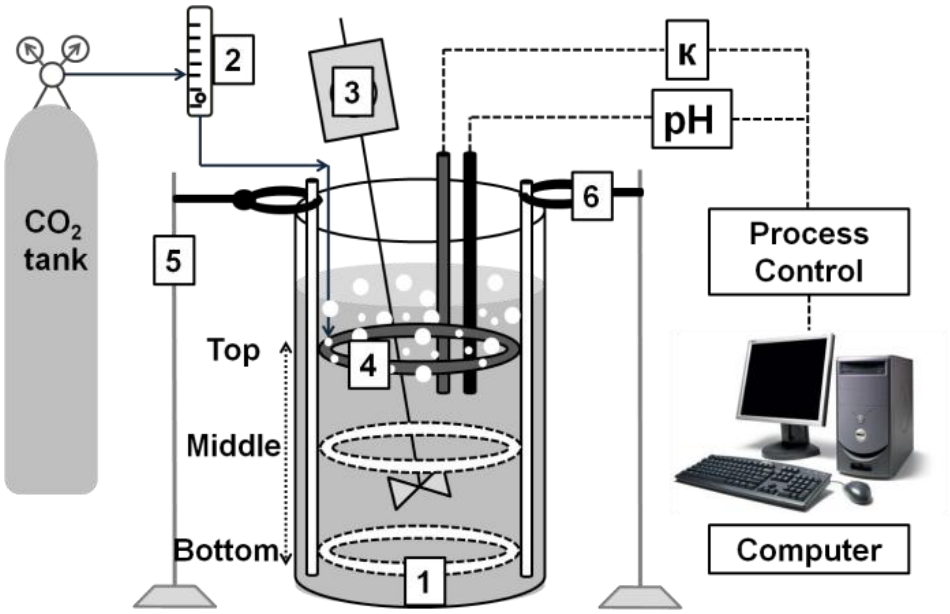

Figure 3.2. Schematic experimental Set-up of different circle pipe level: (1) bubbling reactor; (2) CO_2 flow meter; (3) mechanic stirrer; (4) plastic injection pipe with holes 0.5 mm in diameter; (5) supported sticks; (6) pipe holders.

Initially, 7 L of DI water were placed in the reactor and stirred at 750 RPM with a mechanic stirrer (wise Stir HS-100D from Wisd Laboratory Instrument). Both pH and conductivity values were recorded. Then, a 7.7797 g of $Ca(OH)_2$ were added in to the pure water to obtain a 15 mM of $Ca(OH)_2$ solution. The solution was agitated about 15 min to obtain a homogeneous $Ca(OH)_2$ solution. A CO_2 diffuser consisting of a circular pipe (1 cm diameter) with holes was placed and fixed into the reactor. The place of the gas diffuser was adjusted as shown in the figure, one at the bottom, one at the middle and one at the top. Stirring was kept constant at 750 rpm during the reaction. CO_2 was injected into the system with a 0.3 l/min flow rate through the holes of the circular pipe. About 45 ml of sample were withdrawn from the solution at 5,4,3,2,1 and near 0 mS/cm conductivity values for the SEM analysis. About 1 ml of sample was withdrawn and placed into a UV cuvette in order to measure the particle size and size distribution were measured with a particle size analyzer (Malvern ZS model). A 1 ml of sample was also withdrawn from the solution into a zeta cell and zeta potential values were obtained. Three measurements were obtained and conducted on the same sample and their average values were reported. Reaction was stopped when the pH was decreased to 7 or the conductivity value decreased to near 0 mS/cm. Precipitates were collected in a 50 ml falcon tube by centrifugation for 15 min at 9000 rpm (Hettich - Universal 320). All

samples were dried at 105 ◦C in an oven (Viseven-Won 105) for 12 h. Then, they were placed into vacuum oven (Nuve- EV 018) at 80 ^{o}C before SEM and XRD characterizations.

Parameters such as the stirring rate at 500 rpm, 750 rpm and 1000 rpm were studied in this system.

3.2.3. Effect of NaCl

Calcite crystals were produced by carbonization method in the presence of NaCl. 15 mM $Ca(OH)_2$ solution was prepared by addition of 3.334 gr $Ca(OH)_2$ powders in a 3 L ultra-pure water and stirred at 600 rpm for 30 min before the CO_2 injection. Also, 0.021 gr and 2.629 gr of NaCl were added into each $Ca(OH)_2$ solutions. After the circular pipe was placed and fixed at the top of the reactor, CO_2 was injected into the system with a 0.4 l/min flow rate and stirred at 600 rpm during the experiments. Both pH and conductivity were monitored by Thermo Orion 5 star pH meter with a pH and conductivity cell, respectively. All data were saved during the reactions with Thermo Star Neviagator 21 software program. Particle size and size distribution were measured with a particle size analyzer (Malvern ZS model). Also, zeta potential values were obtained. After reaction was stopped, precipitates were collected from centrifugation for 15 min at 9000 rpm (Hettich - Universal 320). All samples were dried at 105 ◦C in an oven (Viseven-Won 105) for 12 h. Then they were placed into vacuum oven with (Nuve- EV 018) at 80 ^{o}C until suitable for SEM and XRD characterizations.

3.2.4. Effect of Single CO_2 Bubbling on $CaCO_3$ Crystallization

Effect of single CO_2 Bubbling on $CaCO_3$ Crystallization was investigated by designing a reactor as shown in Figure 3.3. 15 mM $Ca(OH)_2$ solution was prepared by addition of 7.7797 gr $Ca(OH)_2$ powders in 7 L ultra-pure water and stirred 750 rpm for 30 min before the CO_2 injection. CO_2 injection was allowed to travel to the surface of the solution by only a single bubble. In this case, only certain amount of CO_2 was allowed to diffuse out into the solution. Also, as shown in the figure, the tank reactor containing $Ca(OH)_2$ solution was stirred at 600 rpm with a mechanical stirrer.

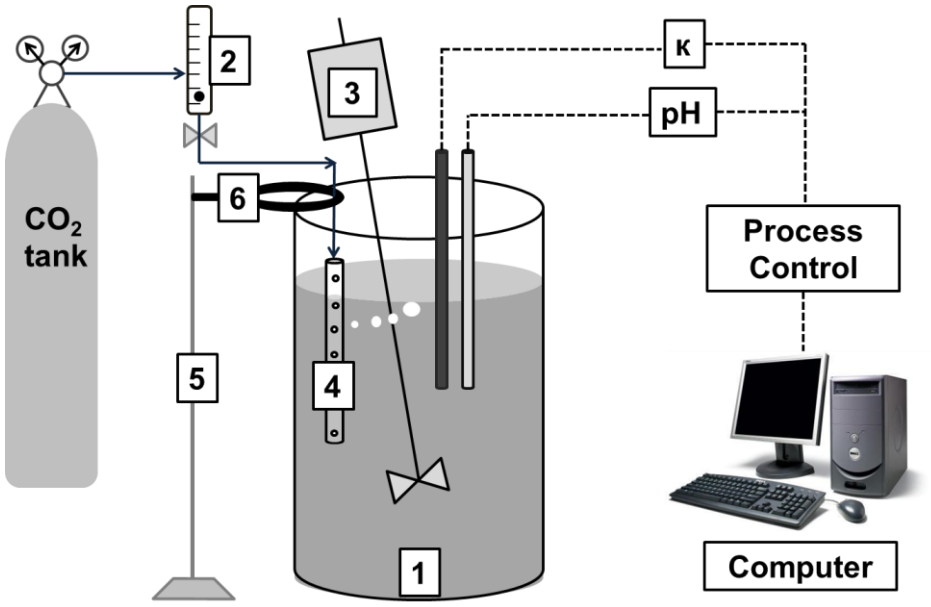

Figure 3.3. Experimental set up for investigation single CO_2 bubbling on $CaCO_3$ Crystallization. (1) bubbling reactor; (2) CO_2 flow meter; (3) mechanic stirrer; (4) perforated glass rod 1.5 mm in diameter; (5) supported stick; (6) holder.

Both pH and conductivity were monitored by Thermo Orion 5 star pH meter with a pH and conductivity cell, respectively. All data were saved during the reactions with Thermo Star Neviagator 21 software program. Particle size and size distribution were measured with a particle size analyzer (Malvern ZS model). Also, zeta potential values were obtained. After reaction was stopped, precipitates were collected from centrifugation for 15 min at 9000 rpm (Hettich - Universal 320). All samples were dried at 105 ◦C in an oven (Viseven-Won 105) for 12 h. Then they were placed into vacuum oven with (Nuve- EV 018) at 80 ^{o}C until suitable for SEM and XRD characterizations.

3.2.5. Partially Bubbled Stirred Tank Reactor

A new reactor called as Partially Bubbled Stirred Tank Reactor was designed as shown in Figure 3.4. As shown in figure, a helix pipe with holes was placed on the top right corner of the stirred tank, which was called the crystallization reaction. The purpose of such design is to produce nano $CaCO_3$ particles in the small crystallization region and transfer them quickly to the CO_2 free area, which was called the stabilization region, where we proposed that the $CaCO_3$ particles were to stabilize by the $Ca(OH)_2$ solution.

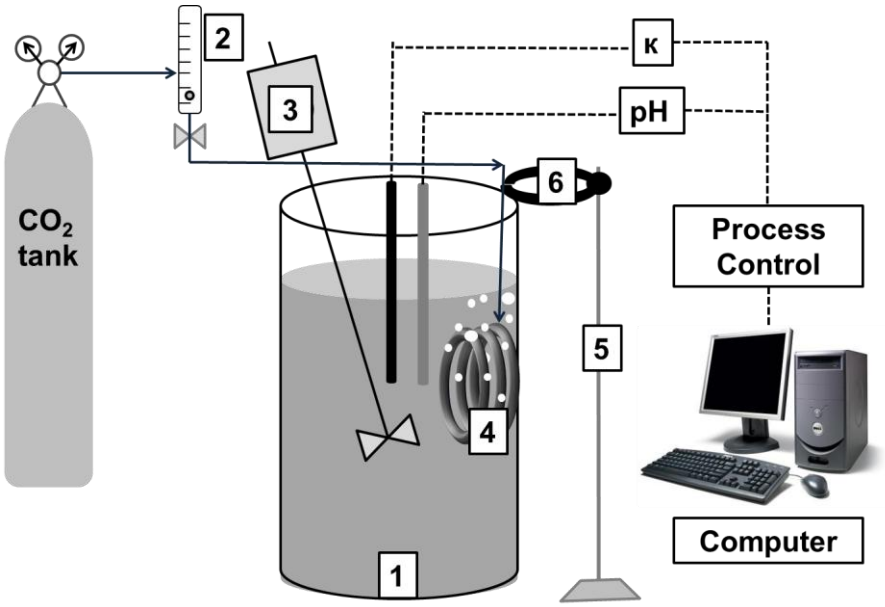

Figure 3.4. Partially Bubbled Stirred Tank Reactor (1) bubbling reactor; (2) CO_2 flow meter; (3) mechanic stirrer; (4) helix pipe with holes 0.5 mm in diameter; (5) supported stick; (6) holder.

A 15 mM of $Ca(OH)_2$ solution was prepared by addition of 7.7797 gr $Ca(OH)_2$ powders in 7 L ultra-pure water and stirred 750 rpm for 30 min before the CO_2 injection. CO_2 injection was applied by helix pipe with holes. CO_2 was injected into the system with a 0.3 l/min of flow rate. Both pH and conductivity were monitored by Thermo Orion 5 star pH meter with a pH and conductivity cell, respectively. All data were saved during the reactions with Thermo Star Neviagator 21 software program. Particle size and size distribution were measured with a particle size analyzer (Malvern ZS model). Also, zeta potential values were obtained. After reaction was stopped,

precipitates were collected from centrifugation for 15 min at 9000 rpm (Hettich - Universal 320). All samples were dried at 105 ◦C in an oven (Viseven-Won 105) for 12 h. Then they were placed into vacuum oven with (Nuve- EV 018) at 80 ^{o}C until suitable for SEM and XRD characterizations.

Different parameters such as stirring rate, slopped stirring, CO_2 injection flow rate, pulsation effect of the CO_2 injection, $Ca(OH)_2$ concentration, and effect of jet flow on the circular pipe were investigated in this system.

3.2.6. Effect of CO_2 Flow Rate on $CaCO_3$ Production

CO_2 flow rates of 80, 220 ve 420 ml/min were tested with a continuous mode. CO_2 was also injected into the $Ca(OH)_2$ solution with a pulsation mode at a 80 ml/min, slower injection rate and at 420 ml/min, a faster injection rate, with a pulsation interval of 5 min and 10 sec, respectively. The experimental conditions of pulsation mode were listed in Table 3.1.

Table 3.1. Experimental conditions of pulsation mode.

CO_2 flow rate (ml/min)	**Concentration of $Ca(OH)_2$ (mM)**	**Stirring (rpm)**	**Δt_{CO2} injection for pulsation**	**Δt waiting**
80	15	750	5 min	10 min
420	15	750	10 sec	5 min

3.2.7. $Ca(OH)_2$ Concentration Effects on $CaCO_3$ Production by Pulsed CO_2 Injection

Effect of $Ca(OH)_2$ concentration on $CaCO_3$ production was investigated at the experimental conditions as given in Table 3.2. CO_2 was injected into the system at 420 ml/min, and the stirring rate was kept constant at 750 rpm.

Table 3.2. Experimental conditions of different $Ca(OH)_2$ concentration sets.

Set	**Concentration (mM)**	**Mass of $Ca(OH)_2$ (gr)**	**Δt_{CO2} injection for pulsation**	**Δt waiting**
1	5	2.5932	1 sec	1 min
2	15	7.7797	2 sec	5 min
3	30	15.5594	5 sec	1 min
4	50	25.9324	15 sec	45 sec

3.2.8. Effect of Jet Flow on the Circular Pipe

In order to facilitate the transfer of newly formed nano $CaCO_3$ particles into the $Ca(OH)_2$ solution, a jet flow assembly was designed as shown in figure 3.5. As shown in the figure, $Ca(OH)_2$ solution was withdrawn from the stabilization section at the bottom of the tank by a pump and injected onto the helix pipe as the crystallization region through a nozzle to create a jet flow aiming to move all the newly generated particles in the crystallization region to the stabilization region. The solution was 12 L, CO_2 flow rate was 420 ml/min and stirring rate was 600 rpm.

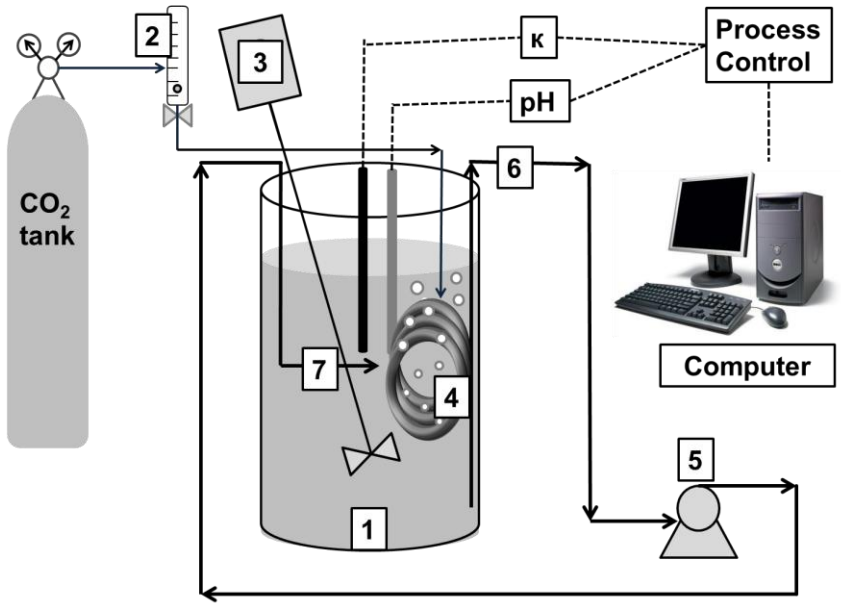

Figure 3.5. New experimental set up for obtaining jet flow in the reactor: (1) Bubbling reactor; (2) CO_2 flow meter; (3) mechanic stirrer; (4) helix pipe with holes 0.5 mm in diameter; (5) centrifugal pump; (6) $Ca(OH)_2$ solution pipe; (7) Jet flow in the reactor.

Both pH and conductivity were monitored by Thermo Orion 5 star pH meter with a pH and conductivity cell, respectively. All data were saved during the reactions with Thermo Star Neviagator 21 software program. Particle size and size distribution were measured with a particle size analyzer (Malvern ZS model). Also zeta potential values were obtained. After reaction was stopped, precipitates were collected from centrifugation for 15 min at 9000 rpm (Hettich - Universal 320). All samples were dried at 105 ◦C in an oven (Viseven-Won 105) for 12 h. Then they were placed into vacuum oven with (Nuve- EV 018) at 80 ^{o}C until suitable for SEM and XRD characterizations.

3.3. Characterization of the Particles

Experiments were conducted under the same conditions, but changing the parameter of interest to be studied. Both pH and conductivity were monitored by Thermo Orion 5 star pH meter with a pH and conductivity cell, respectively. All data were recorded during the crystallization with Thermo Star Neviagator 21 software program. Particle size and size distribution were measured with a particle size analyzer (Malvern ZS model). Also, zeta potential values were obtained. After reaction was

stopped, precipitates were collected from centrifugation for 15 min at 9000 rpm (Hettich - Universal 320). All samples were dried at 105 ◦C in an oven (Viseven-Won 105) for 12 h. Then they were placed into vacuum oven (Nuve- EV 018) at 80 ^{o}C before SEM and XRD characterizations.

3.3.1. SEM Analysis

The morphologies of $CaCO_3$ crystal particles were analyzed by using scanning electron microscope (SEM) fitted with a field emission source (Philips XL 30 S FEG), operating at an accelerated voltage of 3 kV. Before the SEM analysis $CaCO_3$ crystals were coated with gold on copper sample stubs with conducting carbon tape by Sputter Coater (Emitech K550X). $CaCO_3$ crystals were coated at 15 milliamps current and under $6x10^{-2}$ mbar vacuum during 1.5 min.

3.3.2. Particle Size & Zeta Potential Measurements

The particle size, particle size distribution and zeta potential of $CaCO_3$ crystal particles were analyzed by Dynamic Light Scattering (DLS) method with Zeta Sizer (Malvern ZS-model). DLS analysis was conducted by filling $CaCO_3$ solution in low volume disposable sizing cuvette and zeta potential analysis was conducted by filling $CaCO_3$ solution in clear disposable zeta cell.

3.3.3. XRD Analysis

The X-ray powder diffraction (XRD) measurements were carried out using a modified computer-controlled Philips X'Pert Pro X-ray diffractometer. The crystal structure was determined using Cu Ka radiation (45 kV and 40 mA) equipped with a diffracted-beam monochromatic-accelerating detector. The $CaCO_3$ crystal powder was packed into a zero background sample holder. The packed powder was introduced to detector as received. The weight of sample was not important and varied. The diffraction pattern was recorded for 2θ in the range of 10^{o}-80^{o}. X-ray patterns were also used to determine crystal size from the broardening of the diffraction line at half the line

of maximum intensity. References XRD peaks of $CaCO_3$ nanoparticles are given in Figure 3.6.

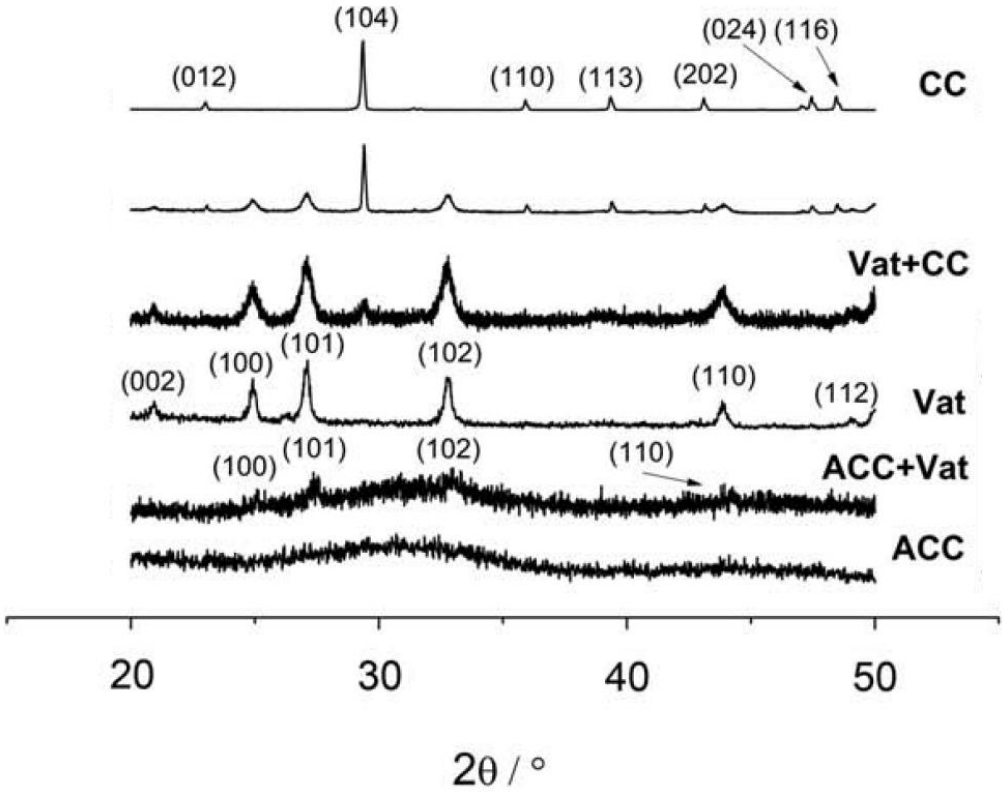

Figure 3.6. Typical XRD pattern of the $CaCO_3$ nanoparticles (ACC: Amorphous Calcium Carbonate, CC: Calcium Carbonate, Vat: Vaterite). (Source: Rodriguez-Blanco et al., 2011).

CHAPTER 4

RESULTS AND DISCUSSION

4.1. Stability of $CaCO_3$ in $Ca(OH)_2$

Mechanism of crystal formation and transformation at different polymorphs of $CaCO_3$ into calcite are still not clear to many researchers. The $CaCO_3$ crystallization process is highly depended on its surface charge because $CaCO_3$ particles occur by ionic reactions. The morphological properties of $CaCO_3$ can be controlled by the interatomic charges between molecules (Gu et al., 2006).

Effect of $Ca(OH)_2$ concentration on the precipitation of $CaCO_3$ was investigated. In order to explain the electrochemical interactions between these particles the zeta potential and the average particle size must be known. For this purpose, four experimental studies were conducted to determine the zeta potential and average particle size in the solutions with different concentrations. First, commercial $Ca(OH)_2$ powder was added into distilled water and different concentration were prepared by subsequent addition of another solid $Ca(OH)_2$ powders. In the second experiment, different concentrations $CaCO_3$ slurries were prepared. In the third experiment, $CaCO_3$ powder was added subsequently into a 10 mM of $Ca(OH)_2$ solution. Similar experiment was repeated by subsequent addition of $Ca(OH)_2$ powder into a 10 mM of $CaCO_3$ slurry. Zeta potential and average particle size for each steps were measured after stabilization.

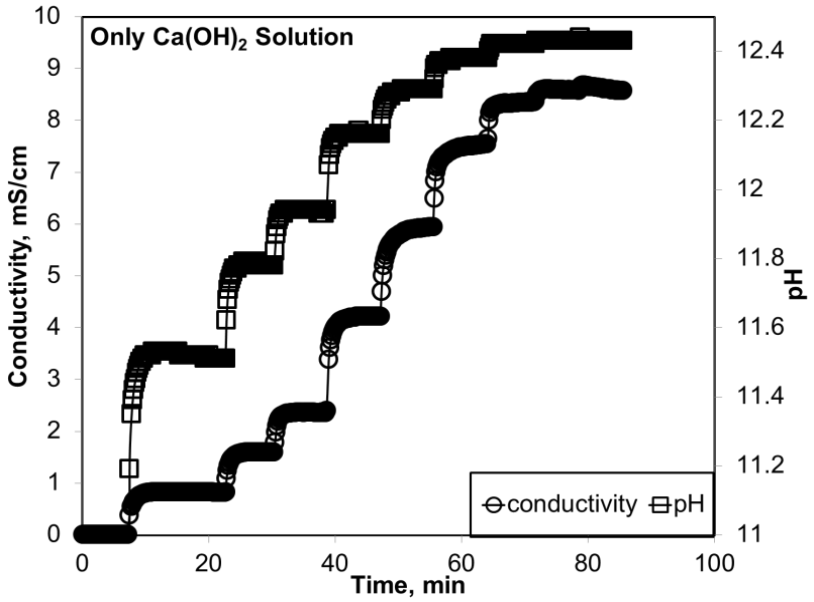

Figure 4.1. Conductivity and pH change of sequential addition of commercial $Ca(OH)_2$.

Figure 4.1 shows pH and conductivity values for the commercial $Ca(OH)_2$ powders, which were prepared by subsequent addition of $Ca(OH)_2$ powder into the distilled water. The conductivity and pH of the solution was increased proportionally with increasing $Ca(OH)_2$ concentration. The conductivity and pH values were nearly constant at 8.6 mS/cm and 12.5, at high $Ca(OH)_2$ concentrations. But, the theoretical solubility of $Ca(OH)_2$ is 0.116 g/100 ml (~23.5 mM) at 20 °C (Lieth, 1977). Zeta potential and average particle size distribution in $Ca(OH)_2$ solution were measured instantly by the Zeta Sizer. As shown in Figure 4.2, below 20 mM (around the solubility limit) of $Ca(OH)_2$ solution, particle size was measured nearly 200 nm and zeta potential was around +30 mV. This means that when $Ca(OH)_2$ is dissolved in solution, the Ca^{2+} ions are coated on the particles surface. Above 20 mM of $Ca(OH)_2$ solution, a sharp increase was observed in average particle size while zeta potential was decreasing. This could be explained by the dissolution of $Ca(OH)_2$ powder at concentration below the solubility limit, and the solid junk particles at concentration above the solubility limit.

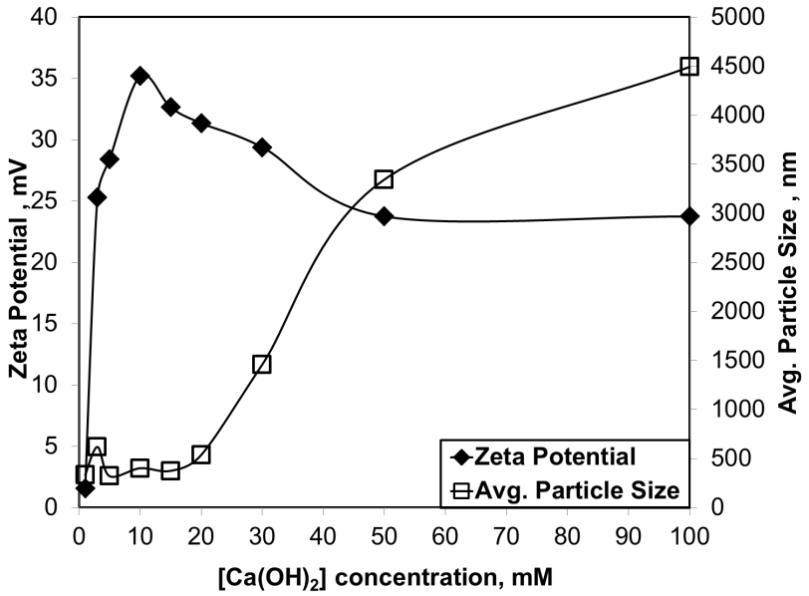

Figure 4.2. Zeta potential and average particle size change of sequential addition of commercial $Ca(OH)_2$.

It should be noticed that there are still particles of about 250 nm in the $Ca(OH)_2$ solution, where all $Ca(OH)_2$ was expected to dissolve. These particles could come from the impurity as the $CaCO_3$ particles; however, as can be seen in Figure 4.3, the $CaCO_3$ in impurity is in micron sizes. Therefore, it could be suspected that these nano particles could be generated in the $Ca(OH)_2$ solution at the very early stages of dissolution. These particles could be $CaCO_3$ or $(Ca^{++})(OH^{-})(CO_3^{=})$ clusters.

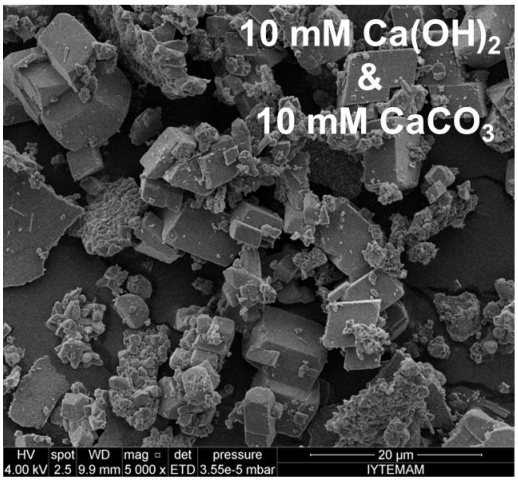

Figure 4.3. SEM image of the $CaCO_3$ impurity in $Ca(OH)_2$ solution.

The conductivity and pH values were shown in Figure 4.4 for the commercial $CaCO_3$ powder. The conductivity of the $CaCO_3$ solution was shown to increase upon the subsequent addition of $CaCO_3$ but, the pH was nearly constant. When the $CaCO_3$ concentration increases in solution, Ca^{++} ion concentration increases, and finally conductivity increases. But, this increase was remained at a very narrow range due to the low solubility of $CaCO_3$. The theoretical solubility of $CaCO_3$ is 0.0013 g/100 ml (~0.15 mM) at 25°C. (Aylward;, Findlay;, Findlay;, & Aylward, 1999).

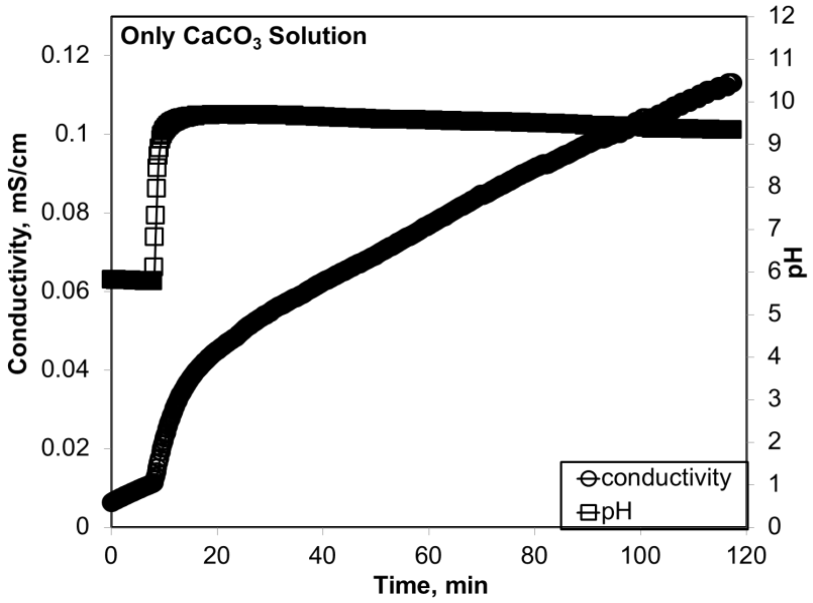

Figure 4.4. Conductivity and pH change of sequential addition of commercial $CaCO_3$.

Zeta potential and average particle size for the $CaCO_3$ slurry were given in Figure 4.5. At low concentrations, the zeta potential for the commercial $CaCO_3$ was measured negative sign at about -16 mV at 1 mM, about -5 mV at 10 mM, about 0 mV at 20 mM and positive, about +5 mV to +10 mV at higher concentrations. This means that when $CaCO_3$ is dissolved in aqueous solution the CO_3^{2-} ions seems to cover mostly the particles surfaces; therefore, the zeta potential was measured to be negative. Average particle sizes were measured about 1 μm to 2 μm although SEM images showed particles about 5 μm in size. The particle size was lower about 500 nm at low $CaCO_3$ concentration at about 1 mM and increased as the concentrations were increased. This could indicate the setting of larger particles and suspension of smaller particle in the cuvette during the measurements.

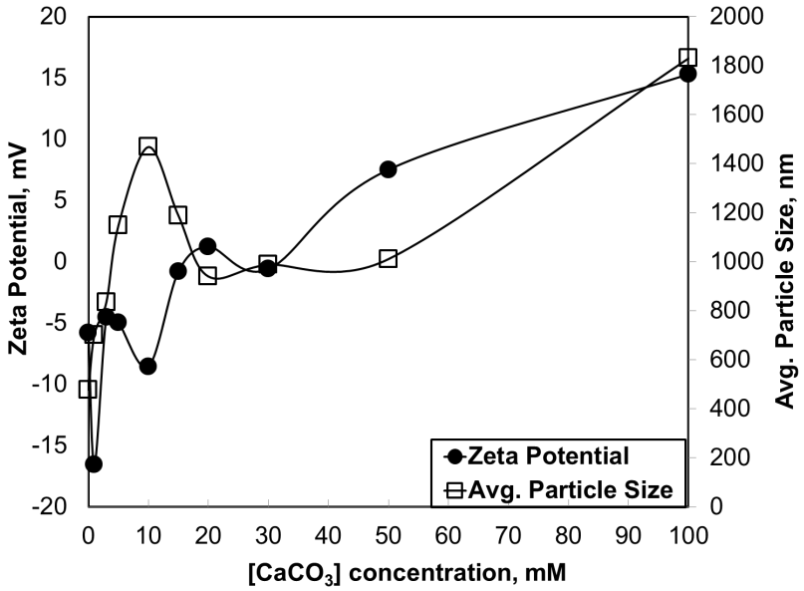

Figure 4.5. Zeta potential and average particle size change of sequential addition of commercial $CaCO_3$.

Figure 4.6 shows the pH and conductivity values during subsequent addition of $Ca(OH)_2$ powder into a 10 mM $CaCO_3$ slurry. The conductivity and pH of solution was raised proportionally with adding $Ca(OH)_2$ into the solution. When the $Ca(OH)_2$ concentration increases, Ca^{++} ion concentration increases, and finally conductivity increases in solution.

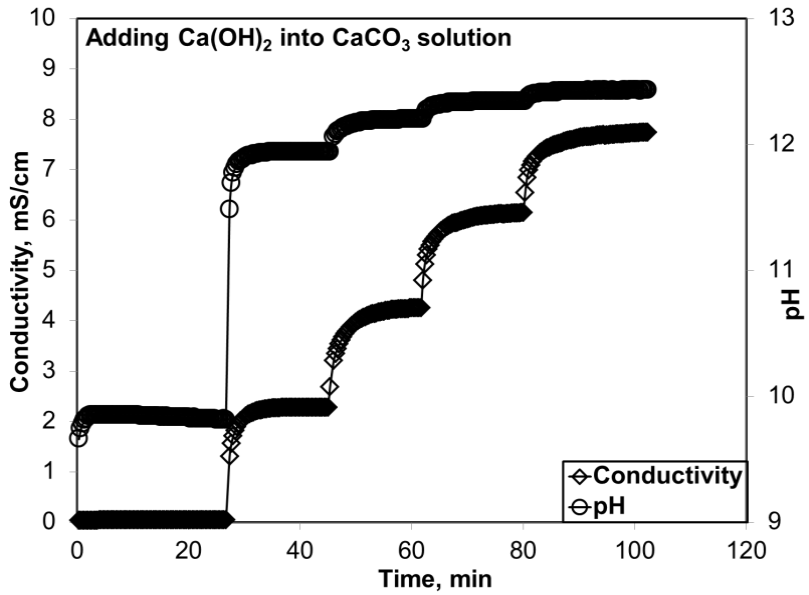

Figure 4.6. Conductivity and pH change of sequential addition of $Ca(OH)_2$ into 10 mM of [$CaCO_3$] solution.

The zeta potential and average particle size during the subsequent addition of $Ca(OH)_2$ powder into the 10 mM of $CaCO_3$ slurry was shown in Figure 4.7. Before the addition of $Ca(OH)_2$, zeta potential of 10 mM of $CaCO_3$ solution was negative at -16 mV and the average particle size was about 2,4 μm. As soon as $Ca(OH)_2$ powder was added into the solution, a sharp increase in zeta potential was observed to about +40 mV and the average particle size decreased to 250 nm. This result supports that when $Ca(OH)_2$ is dissolved in the solution, the Ca^{2+} ions are dominant, which could coated the $CaCO_3$ particle surface.

When $Ca(OH)_2$ concentration is less than its solubility limit, it is expected that all the $Ca(OH)_2$ should be dissolved. In fact, when looking at the figure, this is true. However, this idea is not supported by the SEM images of the $CaCO_3$ particles of about 5 μm in size present in solution. But, it is possible that the $CaCO_3$ particles were suddenly settled and measured valued were due to the $Ca(OH)_2$ dissolution. The settling of $CaCO_3$ particles were probably enhanced by the presence of $Ca(OH)_2$ in the solution.

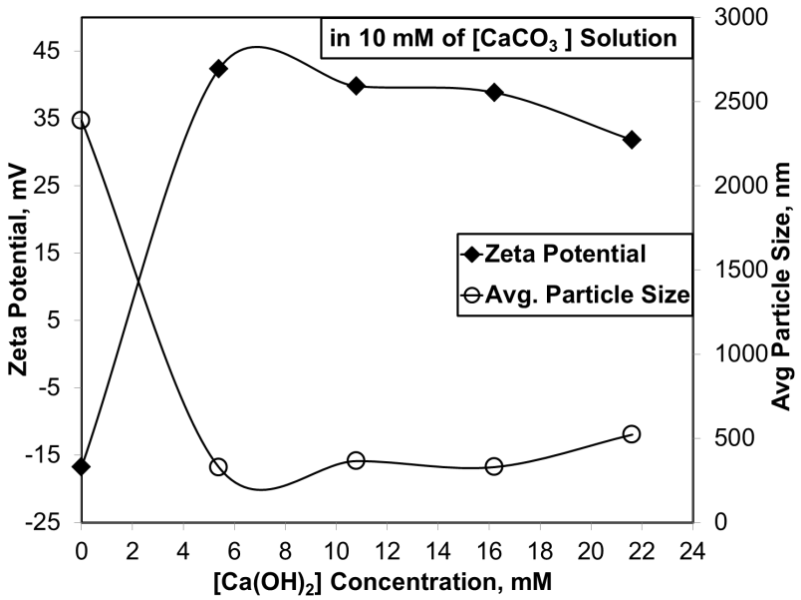

Figure 4.7. Zeta potential and average particle size change of sequential addition of $Ca(OH)_2$ into 10 mM of [$CaCO_3$] solution.

Figure 4.8 shows the pH and conductivity values during subsequent addition of the commercial $CaCO_3$ powders to a 10 mM of $Ca(OH)_2$ solution. Both pH and conductivity were not much affected during the addition of commercial $CaCO_3$ in the 10 mM of $Ca(OH)_2$ solution.

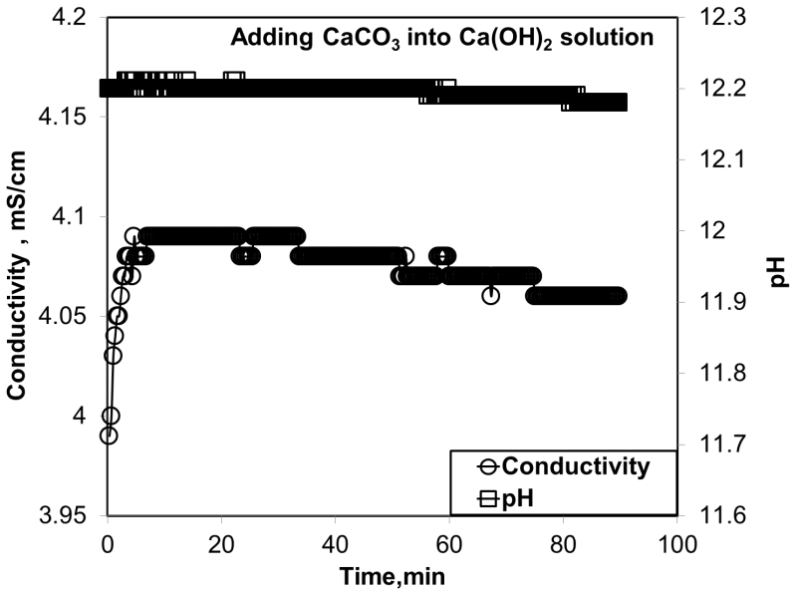

Figure 4.8. Conductivity and pH change of sequential addition of $CaCO_3$ into 10 mM of $Ca(OH)_2$ solution.

Figure 4.9 shows the zeta potential and average particle size of particles measured during the subsequent addition of $CaCO_3$ into 10 mM of $Ca(OH)_2$ solution. Before addition of $CaCO_3$, the $Ca(OH)_2$ had a positive zeta potential which was nearly +40 mV and an average particle size of 300 nm. Both zeta potential and average particle size were not affected much by the addition of $CaCO_3$ powders in the 10 mM of $Ca(OH)_2$ solution, although about 5 μm of $CaCO_3$ particles were added in the solution. This could indicate settling of larger $CaCO_3$ particles while suspending small clusters in the solution.

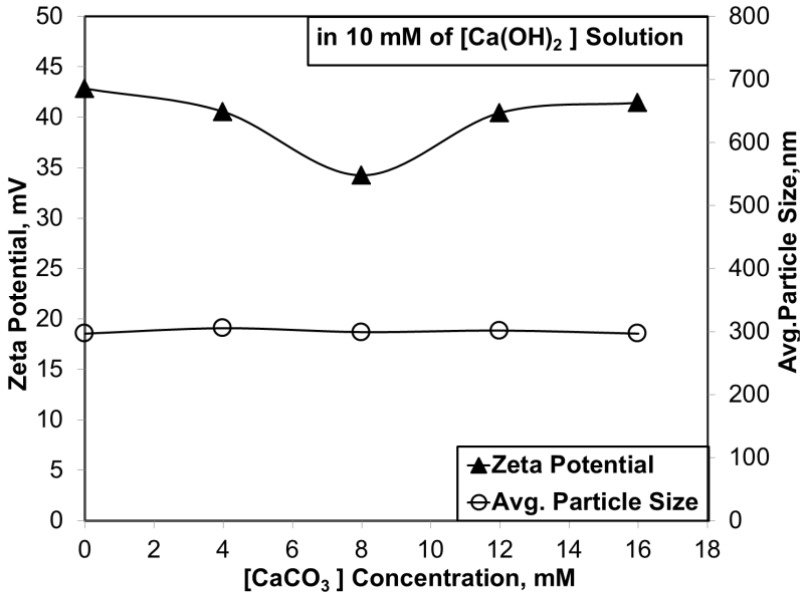

Figure 4.9. Zeta potential and average particle size of sequential addition of $CaCO_3$ into 10 mM of $Ca(OH)_2$ solution.

Figure 4.10 shows the SEM images of commercial $CaCO_3$ and $Ca(OH)_2$ powders and also, particles in their 10 mM mixtures. As shown in the figure, commercial $CaCO_3$ particles are chain like cubical particles of sizes larger than 10 μm. Commercial $Ca(OH)_2$ powder was observed amorphous form. When the mixture of 10 mM $CaCO_3$ and 10 mM $Ca(OH)_2$ precipitates were compared, it can be easily seen that the surfaces of the $CaCO_3$ particles were covered by the amorphous $Ca(OH)_2$ indicating that $Ca(OH)_2$ solution can interact with the $CaCO_3$ particles in solution. Therefore, $Ca(OH)_2$ can act as a stabilizer in the $CaCO_3$ crystallization.

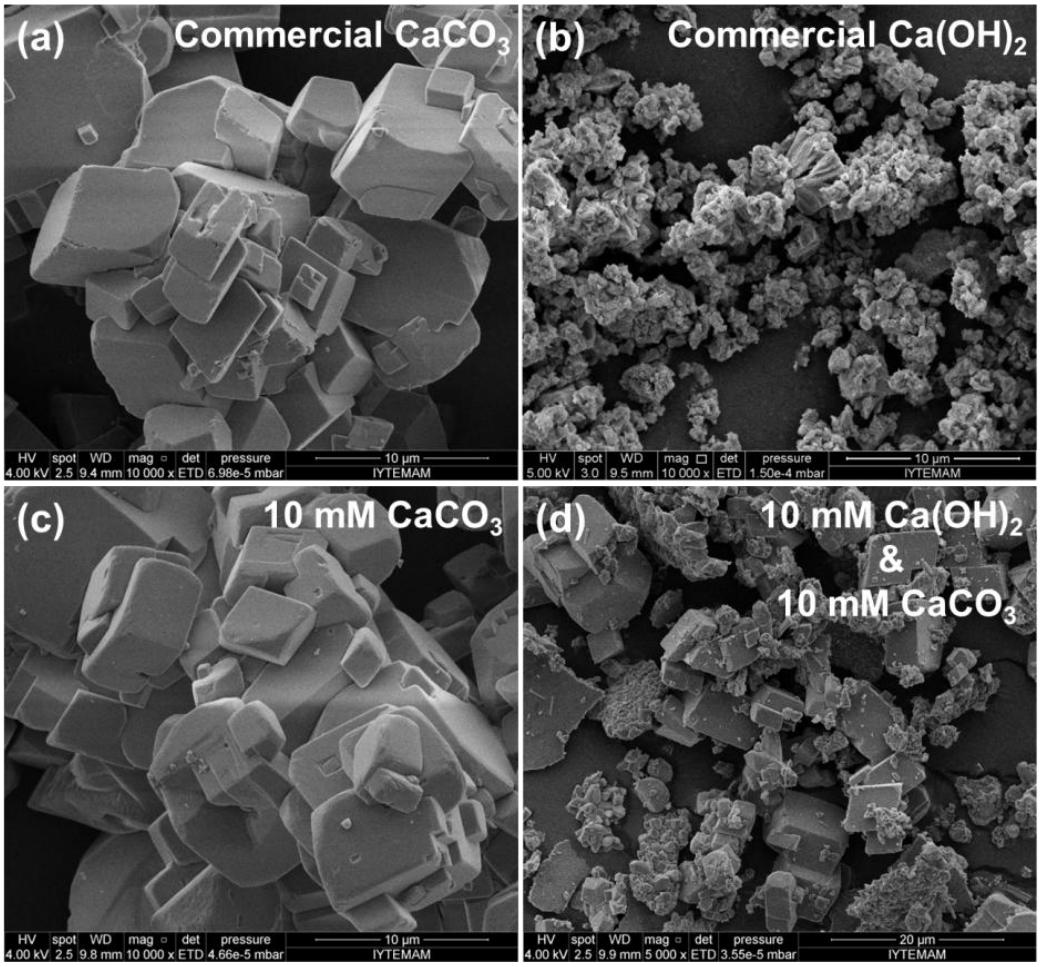

Figure 4.10. SEM images of precipitates (a) Commercial $CaCO_3$ (10000x magnification)(b) Commercial $Ca(OH)_2$ (10000x magnification) (c)Particles in 10 mM $CaCO_3$ (10000x magnification) (d) Particles in 10 mM $CaCO_3$ and 10 mM $Ca(OH)_2$ (5000x magnification).

4.2. Bubble Reactor Studies

Many studies about the $CaCO_3$ crystallization have been focused on the reactive crystallization between gas and liquid reactants. In order to produce nano size, mono dispersed and individual crystals, this key factor should be controlled during the $CaCO_3$ production. For this purpose, different experimental set-ups were designed according to CO_2 injection types and the results were compared with each other. For this purpose, CO_2 gas was injected into the reactor at the top level by three different apparatus such as a perforated glass rod, a circular pipe with holes, and a helix pipe with holes. $Ca(OH)_2$ solutions were prepared at certain concentartions. After the dissolution was completed,

CO_2 injection was applied into the solution. Both of pH and conductivity values were measured. These values for the perforated glass rod were shown in Figure 4.10. As shown in figure, before the CO_2 injection, the conductivity and pH values for pure water were constant at 0.90 µs/cm and 5.5, respectively. When 7.7797 g of $Ca(OH)_2$ were added into 7 L pure water, pH was reached to 12.5 and conductivity was reached to 6.6 mS/cm. As soon as the CO_2 was injected into the system, almost a linear decrease in the conductivity was observed and a slight decrease in pH was observed at the early stage of crystallization. When the conductivity was close to 0 mS/cm a sharp decrease in pH was observed. Finally, pH approached to about 7 and conductivity increased slightly, then the reaction was terminated. The samples which has been taken at 5,4,3,2,1 and near 0 mS/cm conductivity values during the reaction, were analyzed to determine particle size and zeta potential of the produced $CaCO_3$ particles as well as their SEM images and XRD analysis.

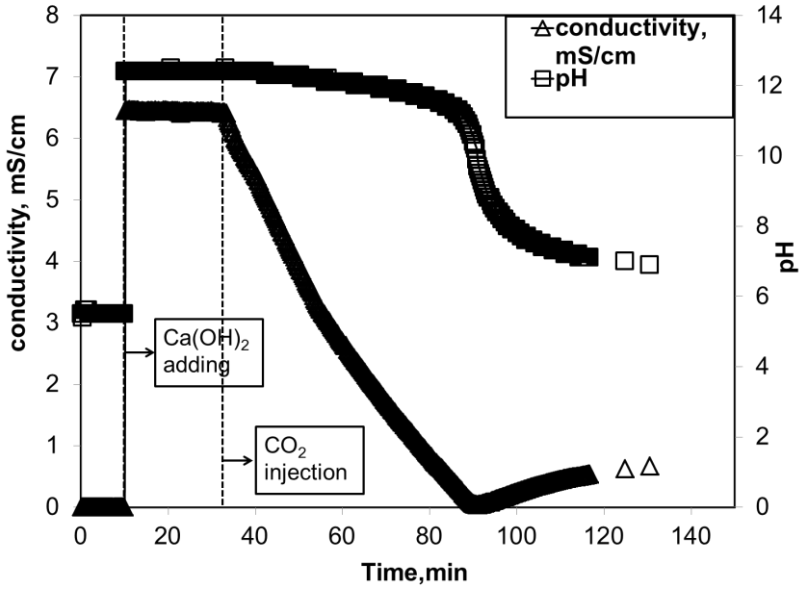

Figure 4.11. Change of conductivity (mS/cm) and pH perforated glass rod during the experiment.

Theoretically, the carbonization reaction is completed when the conductivity has reached to its minimum value and the pH was about 7.0-7.5 (García Carmona et al., 2003). At this moment, the ions in the reaction were consumed and it was the end of the $CaCO_3$ formation. Then, reverse reactions such as dissolution of the products were started to increase.

Similar results were observed when different set-ups were used. As shown in Figure 4.12, pH and conductivity values were decreased with a similar pattern for the different set-ups. Depending on the CO_2 injection rate, for instance, as shown in the circle pipe with holes, the CO_2 transfer rate enhances. As soon as CO_2 was injected into the system, conductivity was decreased linearly and pH was started to decrease slightly. At the end stage of crystallization, pH approached to about 7 and conductivity reached to near 0 mS/cm. The crystallization time was changed according to CO_2 injection methods. The most rapid reaction was observed when CO_2 was injected into the system from perforated glass rod due to the big bubbles occurring in the solution. When CO_2 was injected into the system by circular pipe with holes smaller bubbles were observed, distributed homogeneously in the reactor. When CO_2 was injected into the system by the helix pipe with holes smaller bubbles were observed but non-homogeneously dispersed in the solution. Therefore, the crystallization time was increased due to the small contact area between gas and liquid reactants.

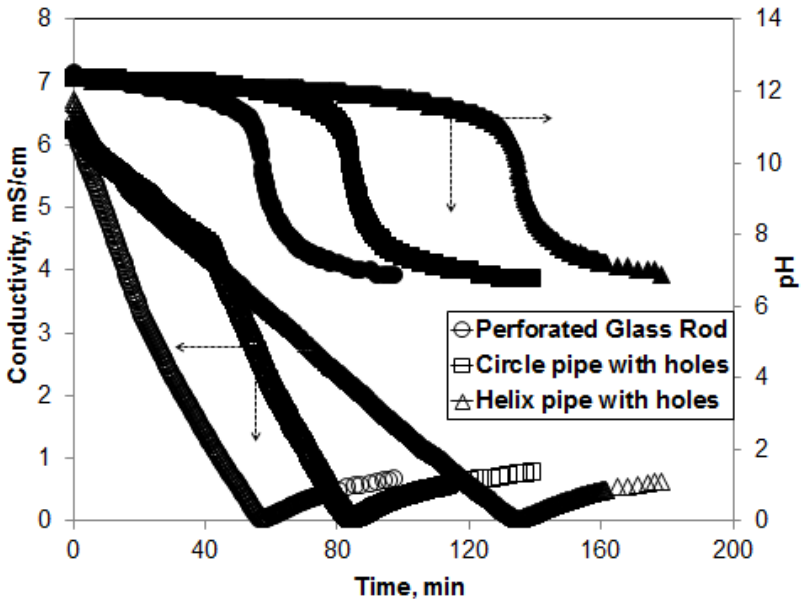

Figure 4.12. Conductivity and pH (mS/cm) values for the different CO_2 injection set-ups.

The samples which has been taken at 5,4,3,2,1 and 0 mS/cm conductivity values during the reactions, were analyzed to determine particle size and zeta potential of produced $CaCO_3$ particles. Figure 4.13 shows the zeta potential and average particle size when different set-ups were used. As shown in the figure, before the crystallization,

the size of particles were observed nearly 200 nm. When CO_2 was injected, the size of particles were started to increase slightly for the helix pipe. An increase in particle size was observed when conductivity and pH were reached to 0 mS/cm or 7, respectively. This may be a result of dissolution of stable particles and aggregation due to the decreasing pH value.

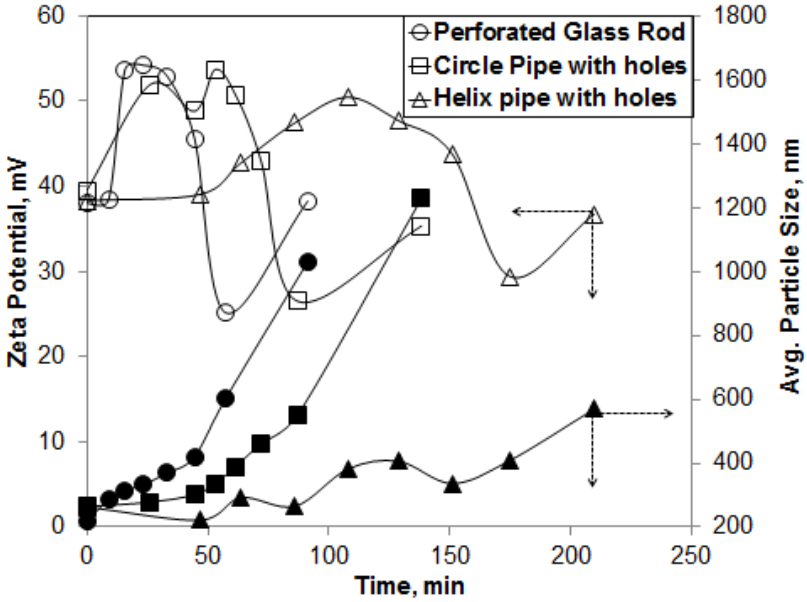

Figure 4.13. Change of zeta potential (mV) and average particle size (nm) during the reactions of different CO_2 injection methods (from perforated glass rod, circle pipe and helix pipe with holes).

Figure 4.14 shows the SEM images of the particles obtained by the perforated glass rod. Morphology of particles was shown step by step for each stages of the experiments. As shown in figure, before the CO_2 injection, at stage (0), there was a mixture of large and small particles in solution. These particles may come from the impurities in the $Ca(OH)_2$ solutions. As soon as CO_2 was injected into the solution, spindle-like $CaCO_3$ particles were observed at stage (1), (2) and (3). These particles change their orientation into crystal form as the conductivity and pH were decreased, at stage (4) and (5). At these stages, spindle-like particles converted into hollow rectangular prism shape when the crystallization was progressed in time. Hollow particles may be occurred due to increasing CO_2 amount in solution. The CO_2 could cause to dissolve the particles resulting in some defects on the more energetic end sides of the crystals. When the reaction is completed, at stage (6) more individual crystal

forms were observed in solution. After this stage, pH was nearly 7, some crystal dissolution was seen since some defects have occurred on the crystal surfaces (Stage 7).

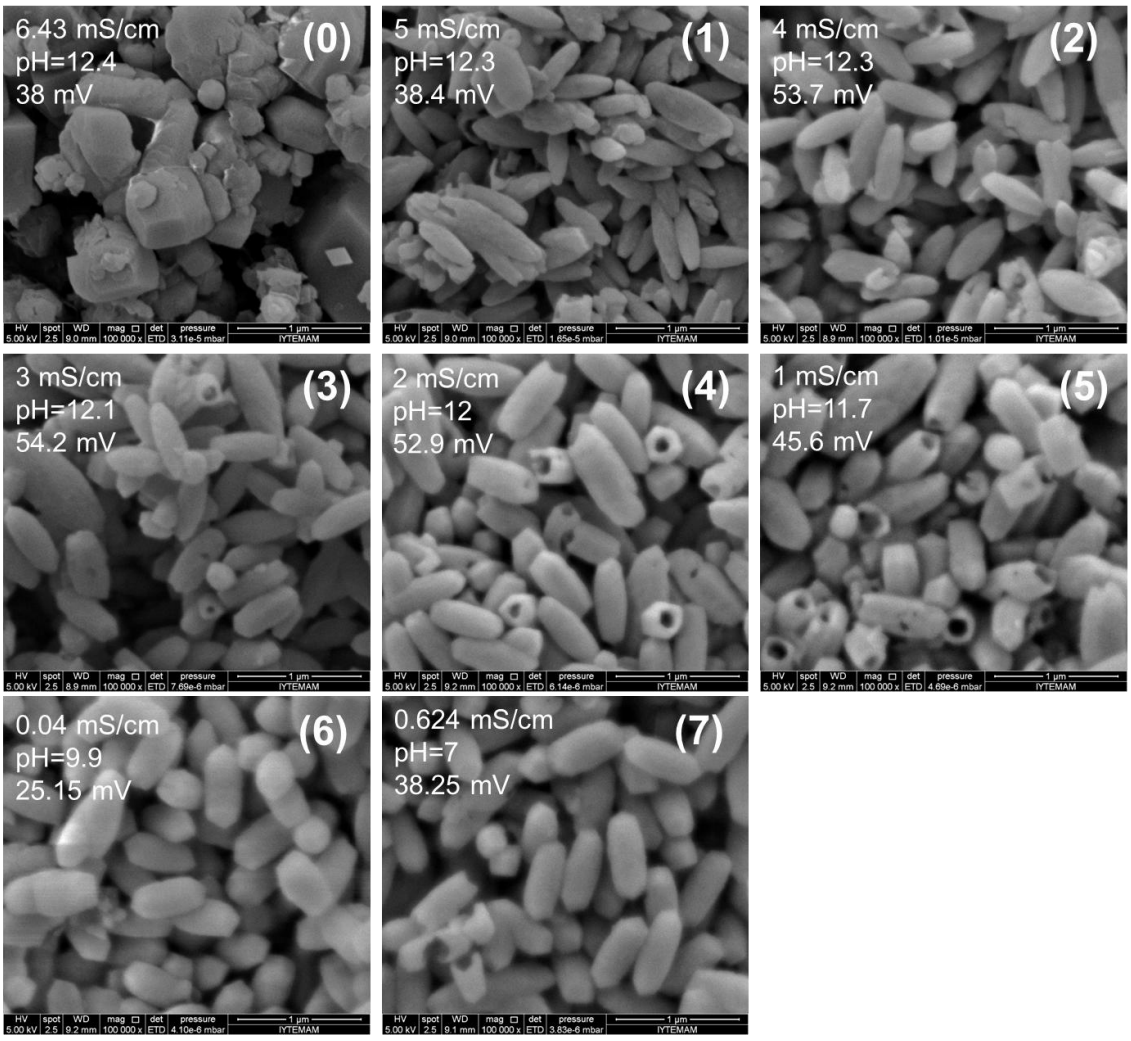

Figure 4.14. SEM images of particles according to advancement of reaction by perforated glass rod CO_2 injection.

Figure 4.15 shows SEM images of precipitate calcite particles, which were obtained by the circlar pipe CO_2 injection at different conductivity values. Before the CO_2 injection, at stage (0), there was a mixture of large and small amorphous particles. As soon as CO_2 was injected into the solution, cubic and interpenetrated $CaCO_3$ particles were observed at stage (1), (2) and (3). At (4) and (5), beside cubic particles, hollow rectangular prism shaped particles were observed. Increasing CO_2 in solution could cause to dissolve the particles resulting in some defects on the more energetic region of the crystals. When the reaction is completed, at stage (6) smaller individual

cubic crystal forms were observed in solution. After this stage, pH has nearly 7, dissolution started and some defects occurred on the crystal edges (Stage 7).

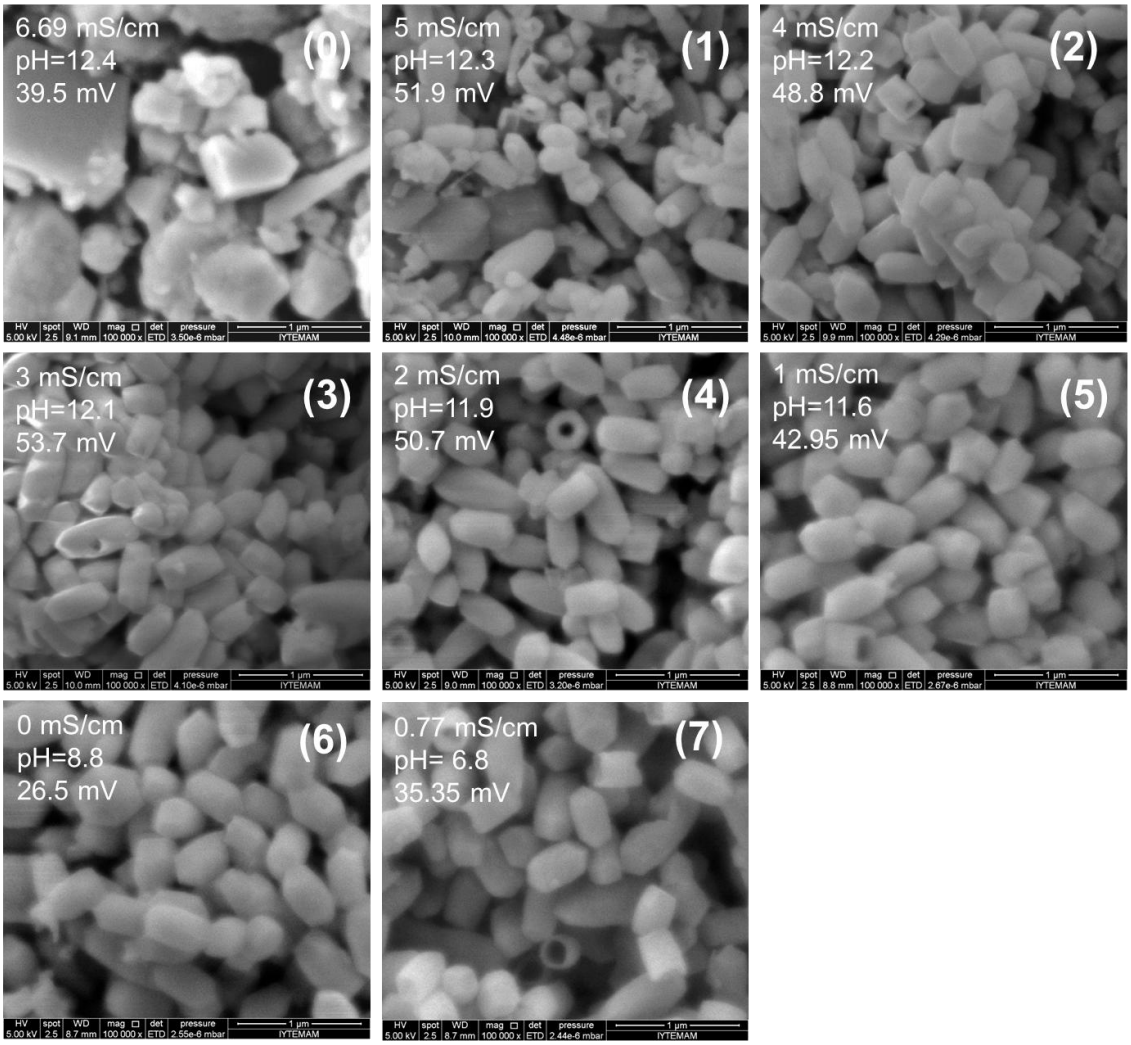

Figure 4.15. SEM images of particles according to advancement of reaction by circle pipe CO_2 injection.

Figure 4.16 shows SEM images of precipitate calcite particles, which were obtained by the helix pipe CO_2 injection set-up, during reaction according to conductivity. Before the CO_2 injection, at stage (0), there was a mixture of large and small amorphous $Ca(OH)_2$ particles. As soon as CO_2 injected into the solution, beside amorphous and interpenetrated $CaCO_3$ particles some impurities such as large cubic $CaCO_3$ particles were observed at stage (1), (2) and (3). These particles started to change orientation into the crystal form depending on conductivity and pH, at stage (4) and (5). At these stages, beside cubic particles, hollow cubic particles were observed. Increasing CO_2 in solution could be caused to dissolve the particles and appearing some

defects on the more energetic region of the crystals. When the reaction was completed, at stage (6) smaller individual cubic crystal forms were observed in solution. After this stage, pH has nearly 7, reverse reactions started and some defects with hollow forms were occurred on the crystal edges (Stage 7).

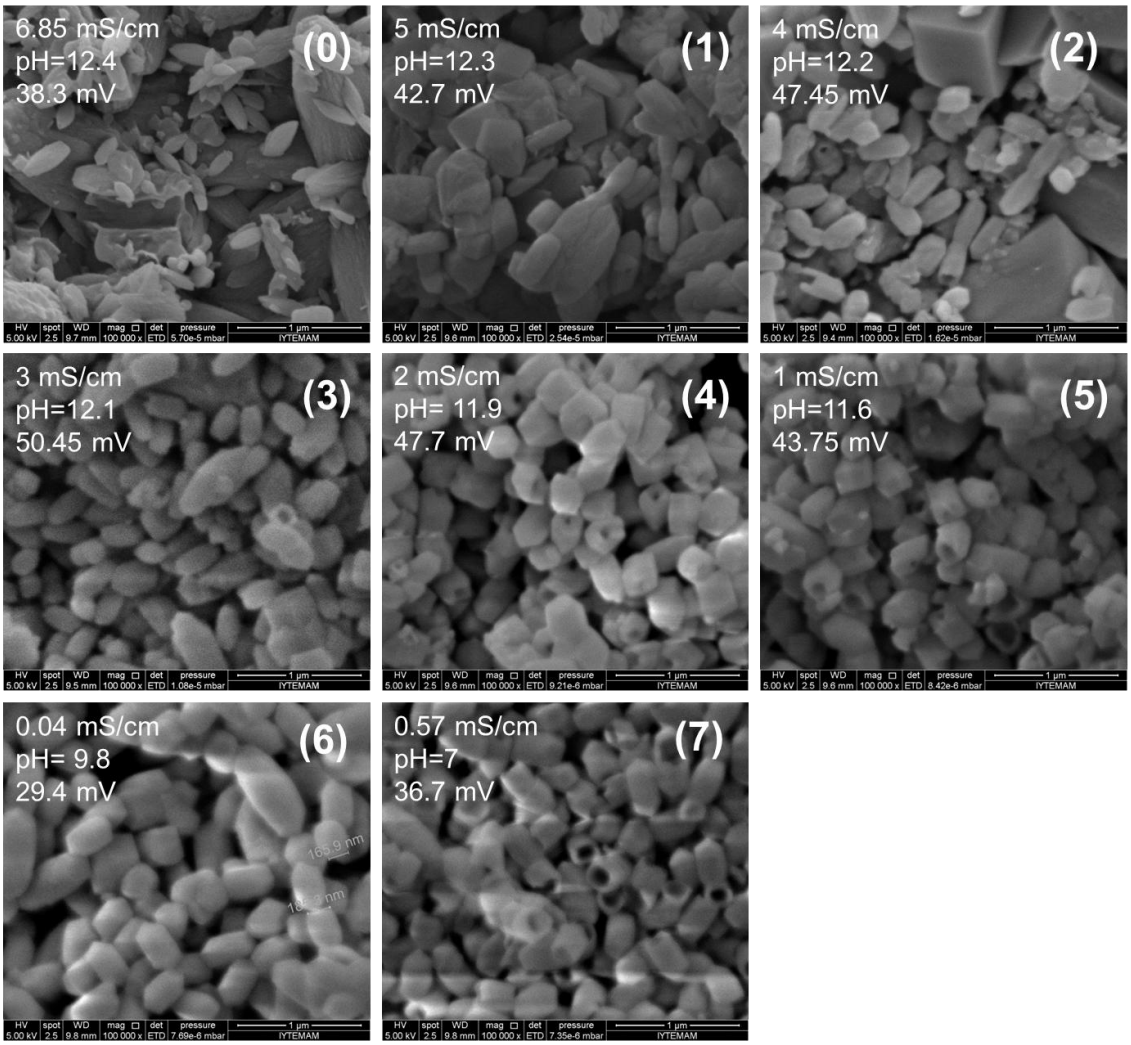

Figure 4.16. SEM images of particles according to advancement of reaction by helix pipe.

Figure 4.17 compares the SEM images of the precipitates obtained from different CO_2 injection methods. These images were the final precipitate particles obtained after the reactions were completed. According to the images, it can be said that, particle size of the cubic crystals is in the submicron range. Individual, mono dispersed and elongated cubic calcite crystals were obtained for different CO_2 injection methods. But, smaller cubic individual particles were obtained when a small area for the CO_2 injection was created in the reactor using the helix pipe. More coagulated calcite

particles were obtained from CO_2 injection by circle pipe. More dispersed CO_2 bubbles in the reactor may cause to increase the contact area between CO_2 and $Ca(OH)_2$ liquid solution, which may cause the coagulation of particles. As a result, nano $CaCO_3$ particles with almost homogeneous size distribution were obtained for the designed experiment set-ups, at relatively low CO_2 flow rates.

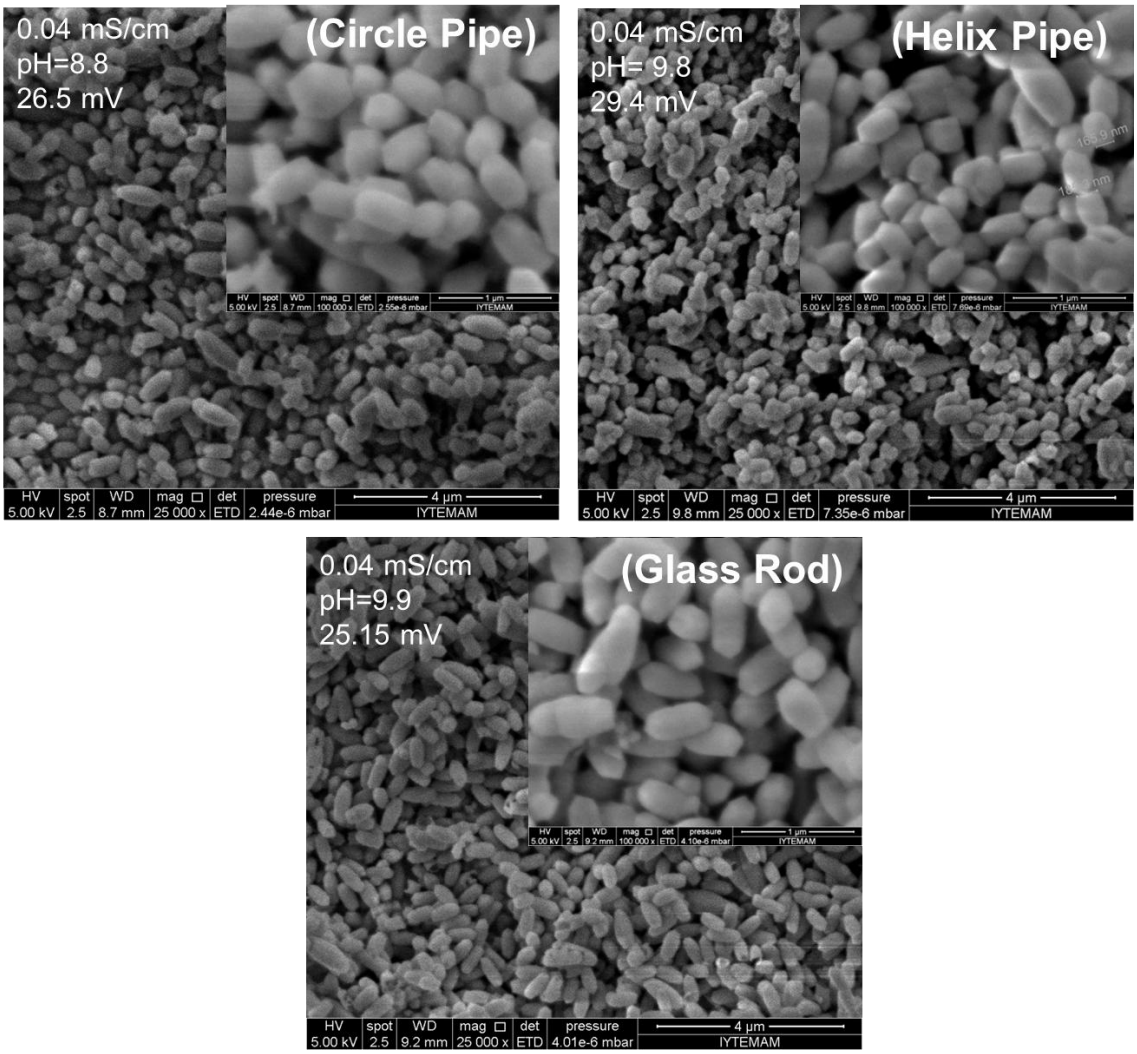

Figure 4.17. SEM images of different CO_2 injection methods (from perforated glass rod, circle pipe and helix pipe with holes).

The comparison of diffraction peaks in XRD was shown in Figure 4.18. According to Bragg's law, the 2θ value at 29.468^o represent that, precipitates are calcite (104). Also the sharp peaks at the *d*-spacing, 3.02864, 1.9166 and 1.8796 indicate the presence of calcite structure. According to XRD patterns of precipitates, the strong and sharp diffractions indicate that all samples were well crystallized calcite. Also, there

was no any different peak detected. Any impurity or any different $CaCO_3$ crystalline form was not observed.

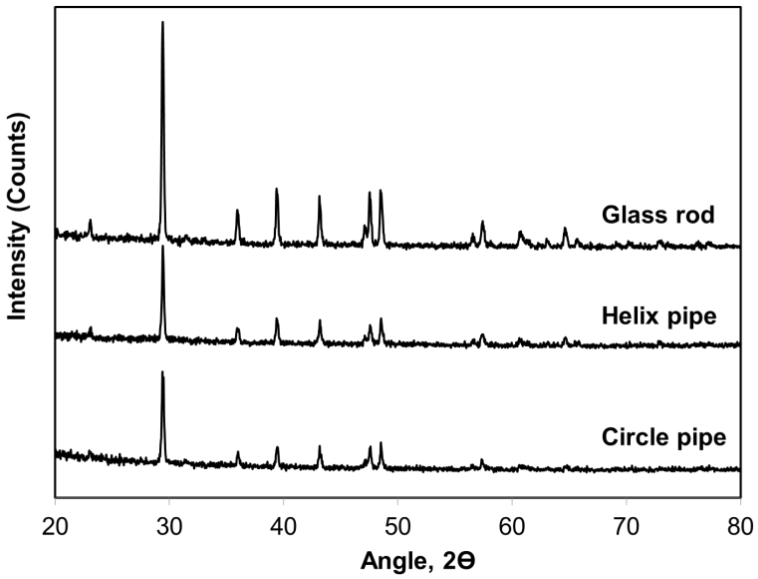

Figure 4.18. XRD patterns of precipitates obtained from different CO_2 injection methods.

4.3. Effect of NaCl on $CaCO_3$ Production by Circle Pipe

Crystallization of calcite occurred in the presence of NaCl. Na^+ and Cl^- ions may influence the coagulation and the size of crystals during $CaCO_3$ precipitation. Studies on the interaction of ions with calcite suggest that these ions can increase ionic interactions of solution and separate the crystal planes during crystal growth (Kim, Ahn, Ko, Park, & Han, 2006; Rodriguez-Blanco, Shaw, Bots, Roncal-Herrero, & Benning, 2012). Effects of NaCl addition on the crystallization of calcite was investigated in the presence of different amount NaCl which were 0.12 mM and 15 mM in solution by using circular pipe CO_2 injection set-up at the top level of reactor. The comparisons of pH and conductivity curves were given in Figure 4.19. As shown in the figure, there is not a strong correlation between NaCl amount and precipitation time of reaction. But conductivity was not decreased below 1 mS/cm during reaction due to the high ionic strength of the solution when the high amount NaCl was used. It was concluded that average reaction time is observed nearly 20 min in the presence of varying NaCl during reaction.

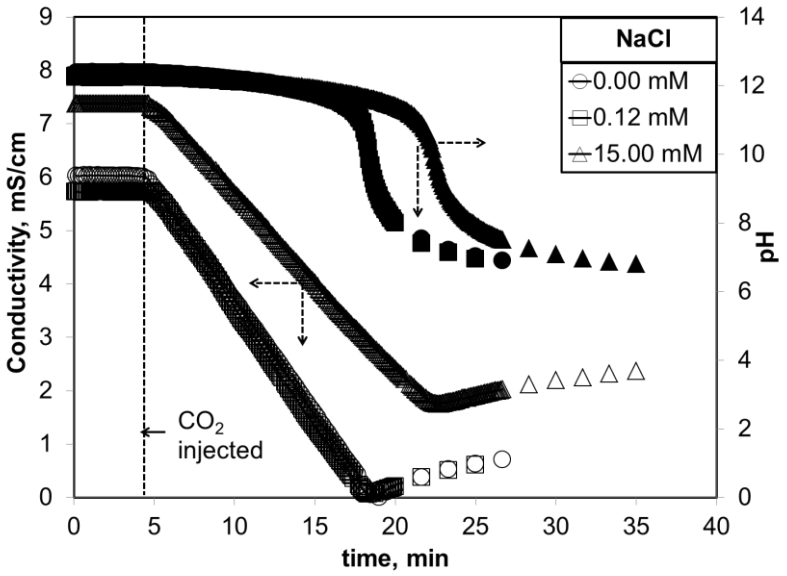

Figure 4.19. Change of pH and conductivity (mS/cm) of experiments in presence of different amount NaCl.

Figure 4.20a-b shows the change of zeta potential and average particle size of precipitates in the presence of different amount NaCl in solution by using circular pipe CO_2 injection at the top level of reactor. As shown in Figure 4.20-a, an increase in the zeta potential was nearly 50 mV at the beginning of crystallization when small amount NaCl was used. Then, a decrease in zeta potential was observed below +30 mV. At this point, ionic charge of solution decreased due to the conversion of ions, which caused a slight to coagulation. This is supported by the average particle size which increases to the late stages of the crystallization. As shown in Figure 4.20-b, produced particles were obtained in submicron size during the reactions with the presence of low NaCl amount. When NaCl amount increases, the average particle size increases.

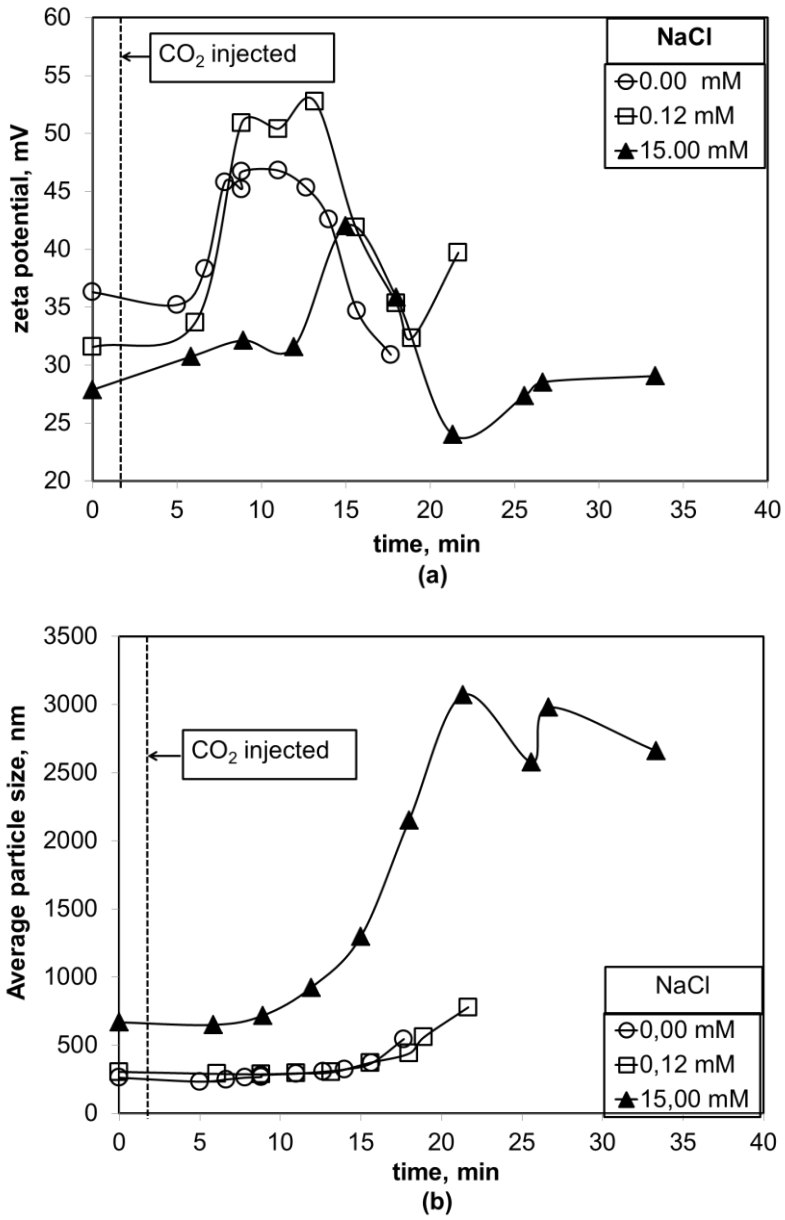

Figure 4.20. (a) The zeta potential and (b) average particle size changes of experiments contain different NaCl amounts.

Morphological analysis of precipitates was achieved from SEM images which were taken at different conductivity values during crystallization. SEM images of particles were shown in Figure 4.21 and Figure 4.22 step by step for different NaCl amounts such as 0.12 mM NaCl and 15 mM NaCl, respectively.

Figure 4.21 shows the SEM images of precipitated calcite particles, which were obtained in the presence of 0,12 mM NaCl. Before the CO_2 injection, at stage (0), there was a mixture of small and large smooth cubic particles. These may be occurred in solution due to some impurities, especially $CaCO_3$ coming from $Ca(OH)_2$ solution. As

soon as CO_2 injected into the solution, spindle-like small cubic $CaCO_3$ particles were formed at stage (1) and (2). Cubic calcite particles as well as hollow particles were observed at stage (3), (4) and (5). At these stages, increasing CO_2 amount in solution could cause to dissolve the particles resulting in some defects on the more energetic sides of the particles. When the reaction was completed at stage (6) beside cubic particles, individual rectangular calcite particles were formed. This result was nearly the same with the reaction when no NaCl included in the solution. Finally, round calcite particles were obtained at the end of the crystallization when pH was nearly 7 at stage (7).

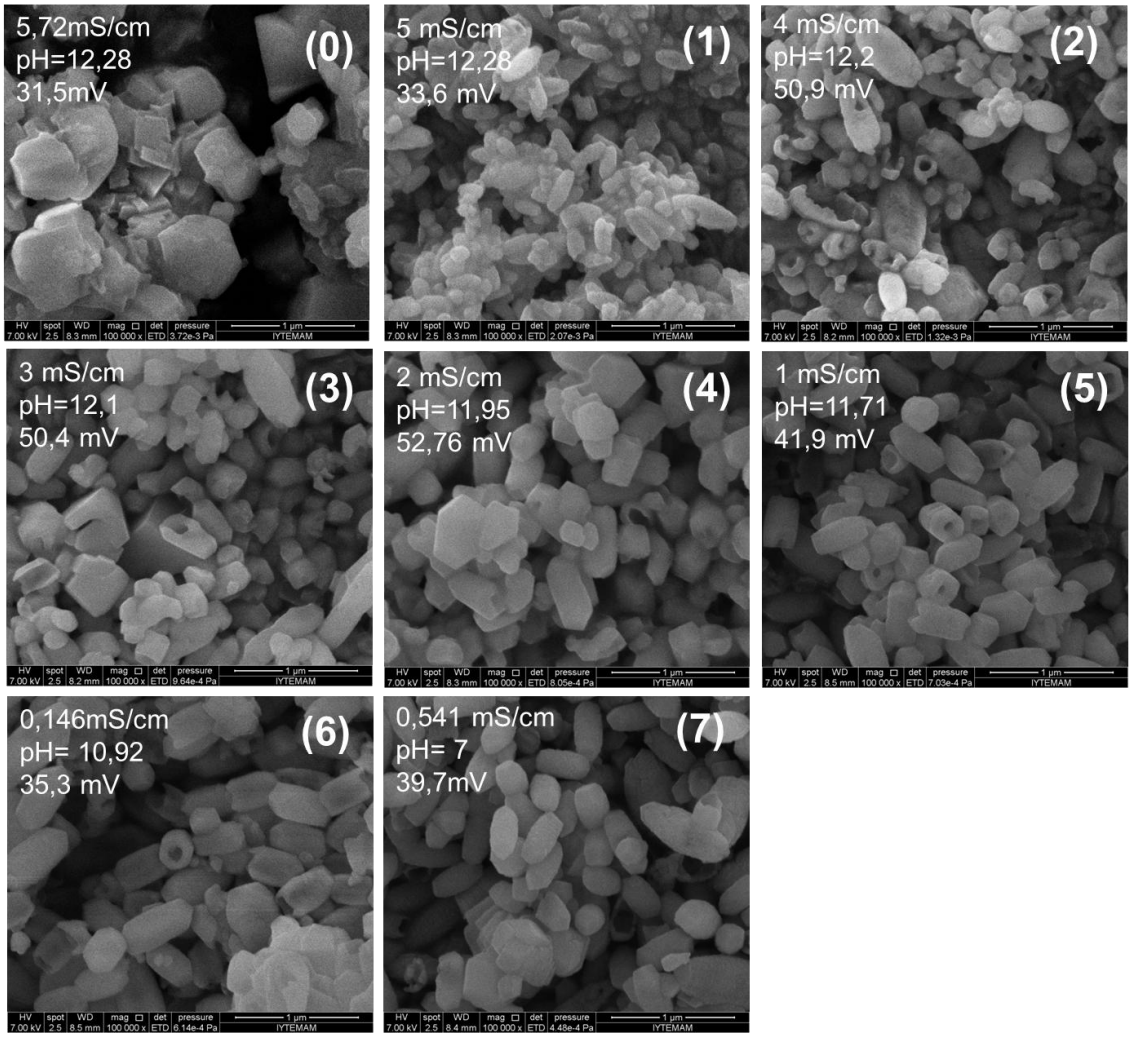

Figure 4.21. SEM images of particles according to advancement of reaction in presence of 0,12 mM NaCl.

Figure 4.22 shows SEM images of precipitate calcite particles, obtained in the presence of 15 mM NaCl. Before the CO_2 injection at stage (0), there were some

particles which may probably come from some impurities such as $CaCO_3$. As soon as CO_2 injected into the solution, small $CaCO_3$ particles were formed at stage (1) and (2). These particles oriented into more individual rectangular shapes at stage (3). At these stages, some hollow particles were observed due to the increase in the CO_2 amount in the solution which could cause the dissolution of the particles and resulting in some defects on the more energetic sides of the crystals. When the reaction was completed at stage (4), individual, almost cubic and hollow calcite particles were formed. This result may be observed according to high amount NaCl in solution. Na^+ and Cl^- ions may influence the crystal growth by increasing electrostatic strength between and around the particles during $CaCO_3$ precipitation. Finally, hollow cubic calcite particles were obtained at stage (7) when the pH value was nearly 7.

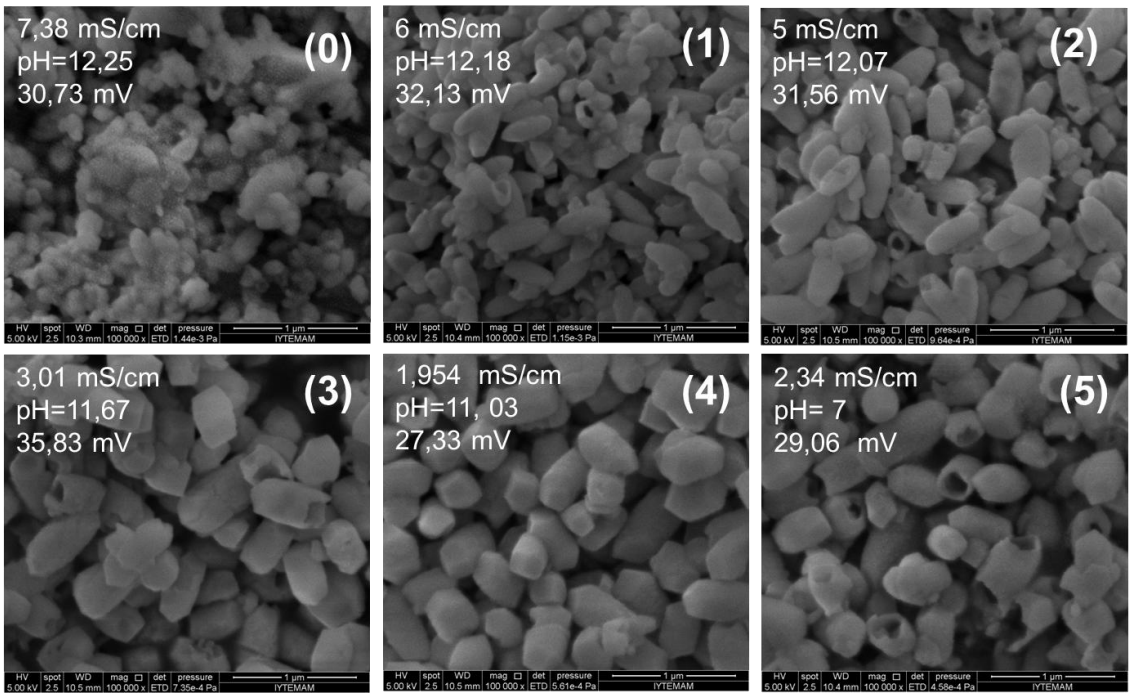

Figure 4.22. SEM images of particles according to advancement of reaction in presence of 15 mM NaCl.

4.5. Effect of CO_2 Injection Levels on $CaCO_3$ Production by Circular Pipe

Effect of CO_2 injection level on the crystallization of calcite was investigated by adjusting the level of the circular pipe in the reactor. Pipe level was adjusted at the top, middle and bottom in the reactor, respectively. The contact time of gas and liquid reactants may influence the morphology of crystals during calcium carbonate precipitation. The pH and conductivity values are given in Figure 4.23. As shown in the figure, decrease in conductivity and change in pH show similar trends. Homogeneous and same size CO_2 bubbles were created in the system for all pipe levels. For that reason, very rapid crystallizations (~10 min) have occurred in the solution. The reaction time was even more decreased when CO_2 was injected at the bottom of the reactor due to the high contact area of reactants. The CO_2 bubbles in the system decreased while the pipe levels were at the top and middle in the reactor. The reaction time was nearly the same at these levels.

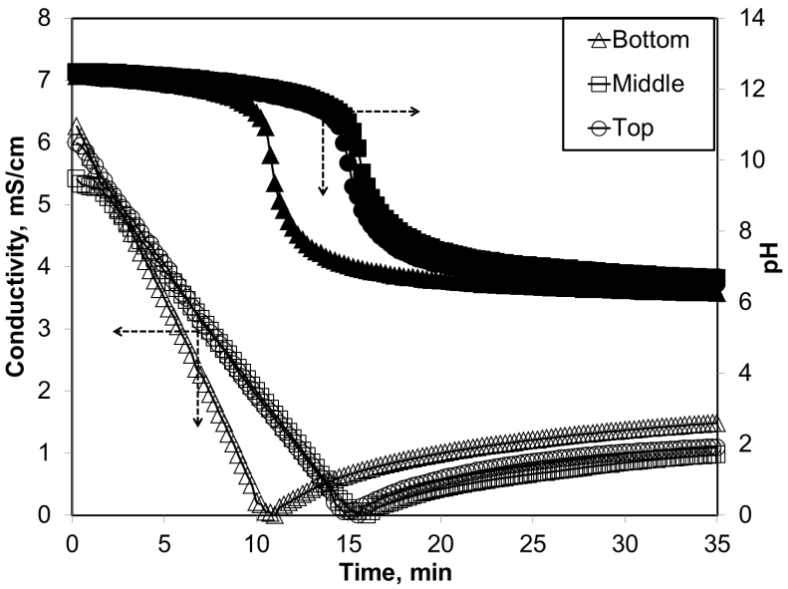

Figure 4.23. Change of pH and conductivity at different CO_2 injection levels.

Figure 4.24 shows the zeta potential and average particle size of particles at different CO_2 injection levels. As shown in figure, the average particle size was nearly 200 nm before the crystallization reaction. When reaction was started, the average size of the particles were started to increase slightly. Particle size of all CO_2 injection level

was obtained in submicron sizes during crystallizations. After reactions were completed, a sharp increase in the average particle size was observed. The increase in average particle size could be due to aggregation at low pH values. CO_2 injection from the bottom resulted in fast crystallization. So, the particle sizes were larger than those for the other injection levels. Nearly the same zeta potential curves were obtained during the reactions. A sharp increase was observed to about +45 mV at the beginning of reaction. Then, a sharp decrease was seen to about +20 mV at the late stage of crystallization. It is possible to say that the surfaces of the calcite crystals covered by the ionic species that make than attractive to form of aggregation.

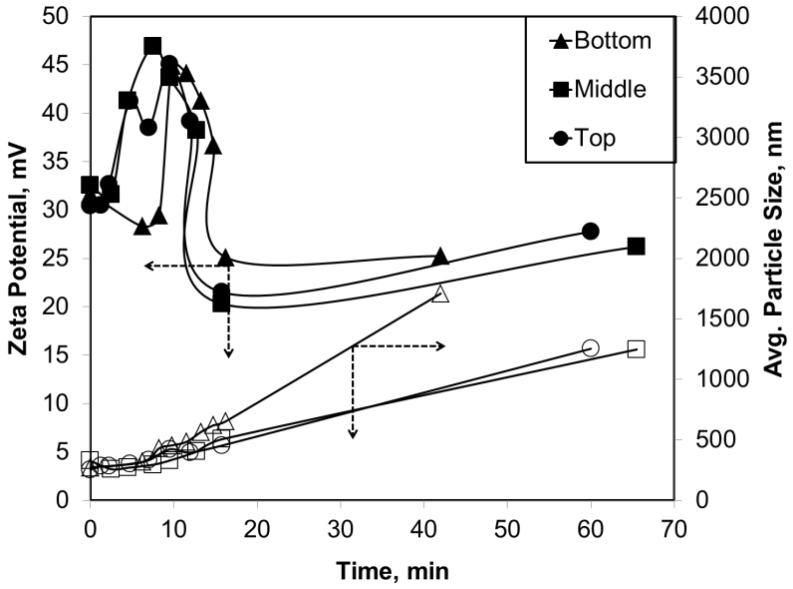

Figure 4.24. Change of zeta potential and average particle size at different CO_2 injection levels.

Figure 4.25 shows the SEM images of particles obtained from crystallization when the CO_2 injection level was at top. As shown in figure, before the CO_2 injection at stage (0), there was a mixture of large and small amorphous $Ca(OH)_2$ and $CaCO_3$ particles. As soon as CO_2 injected into the solution, spindle-like $CaCO_3$ particles were obtained at stage (1) and (2). Interpenetrated very small particles were occurred in solution as the conductivity and pH were decreasing at stage (3), (4) and (5). At these stages, the spindle-like particles covered by the new cubic particles which were participated into spindle-like structure through the crystallization in progress. When the reaction was completed at stage (6) more individual particles with some defects were

formed in solution. After this stage, pH was nearly 7, reverse reactions were started and some defects due to dissolution was occurred on the crystal surfaces (Stage 7).

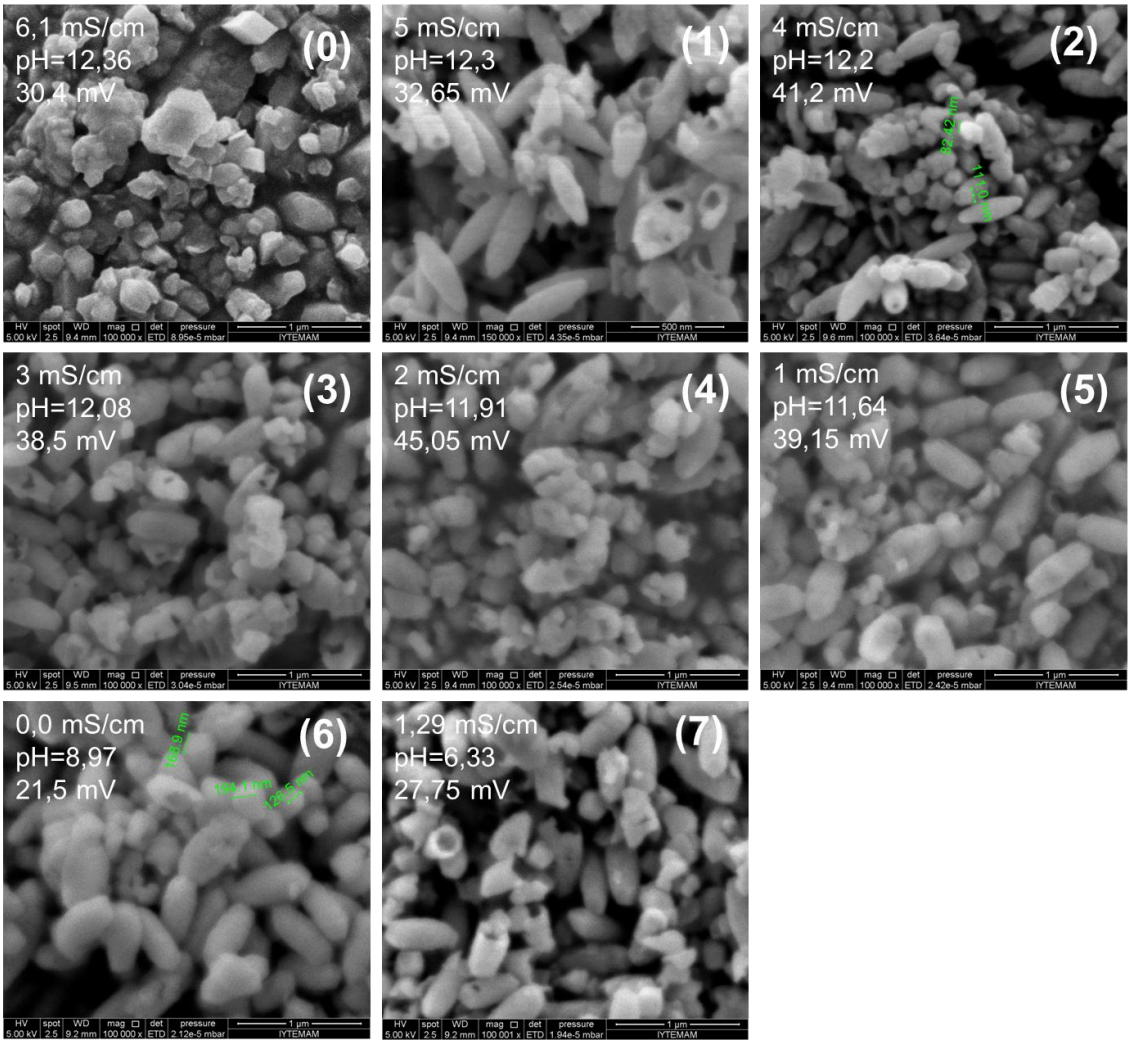

Figure 4.25. SEM images of particles obtained from the top level according to advancement of reaction.

Figure 4.26 shows SEM images of precipitate calcite particles, which were obtained by CO_2 injection from the middle level of the reactor. Before the CO_2 injection, at stage (0), there was some impurity small particles appeared. As soon as CO_2 injected into the solution, spindle-like $CaCO_3$ particles were formed at stage (1). Then, these particles converted into interpenetrated particles at stage (2) and (3). This aggregated structure could be occurred a result of more CO_2 in solution depending on the injection level. Then, particles started to reorient themselves into more individual rice-like shapes at stage (4) and (5). Increasing CO_2 amount could cause some defects

on the particles. When the reaction was completed at stage (6) smaller individual crystal particles were obtained in solution.

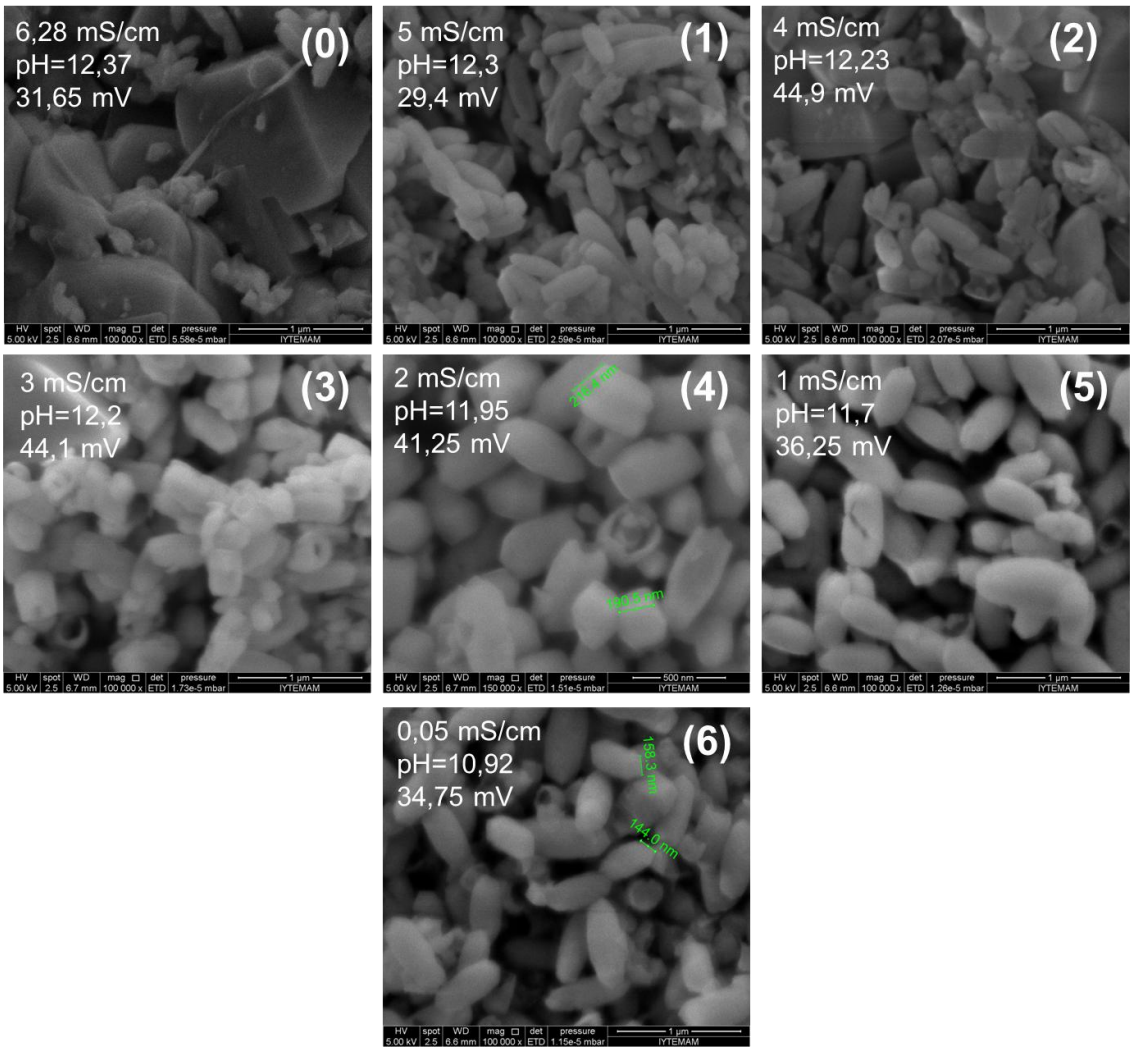

Figure 4.26. SEM images of particles obtained from the middle level according to advancement of reaction.

Figure 4.27 shows SEM images of precipitate calcite particles, which were obtained by CO_2 injection from the bottom level of the reactor. Before the CO_2 injection at stage (0), again some impurity $CaCO_3$ particles were observed. As soon as CO_2 injected into the solution spindle-like $CaCO_3$ particles were obtained at stage (1) and (2). Then, these particles were oriented into rice-like particles depending on conductivity and pH at stage (3), (4) and (5). When the reaction is completed at stage (6), particles were almost disintegrated and more interpenetrated chain-like forms were

observed in solution. After this stage, pH was nearly 7, dissolution was effective resulting in chain-like aggregated particles at stage (7).

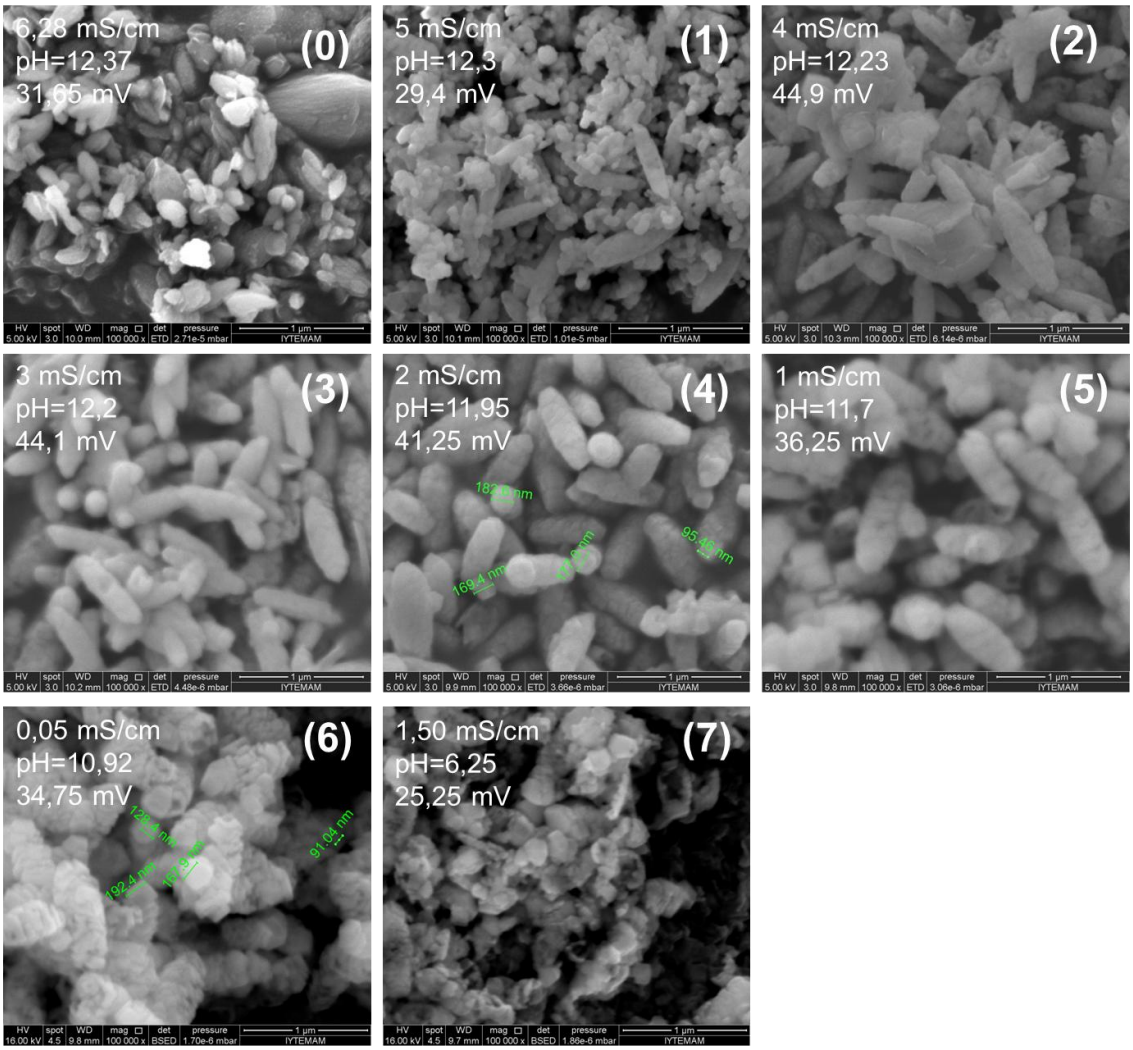

Figure 4.27. SEM images of particles obtained from the bottom level according to advancement of reaction.

Figure 4.28 shows the SEM images of the precipitates obtained from different CO_2 injection levels. These images are representative of the final precipitated particles after the crystallization was completed. According to the images, it can be said that nano calcite particles can be produced in different morphologies by the bubble reactor. Individual, mono dispersed, and elongated calcite crystals were obtained from top and middle CO_2 injection levels. However, chain-like and aggregated particles were obtained during the CO_2 injection at the bottom, due most probably to the excess CO_2 contact time with the calcite particles in solution.

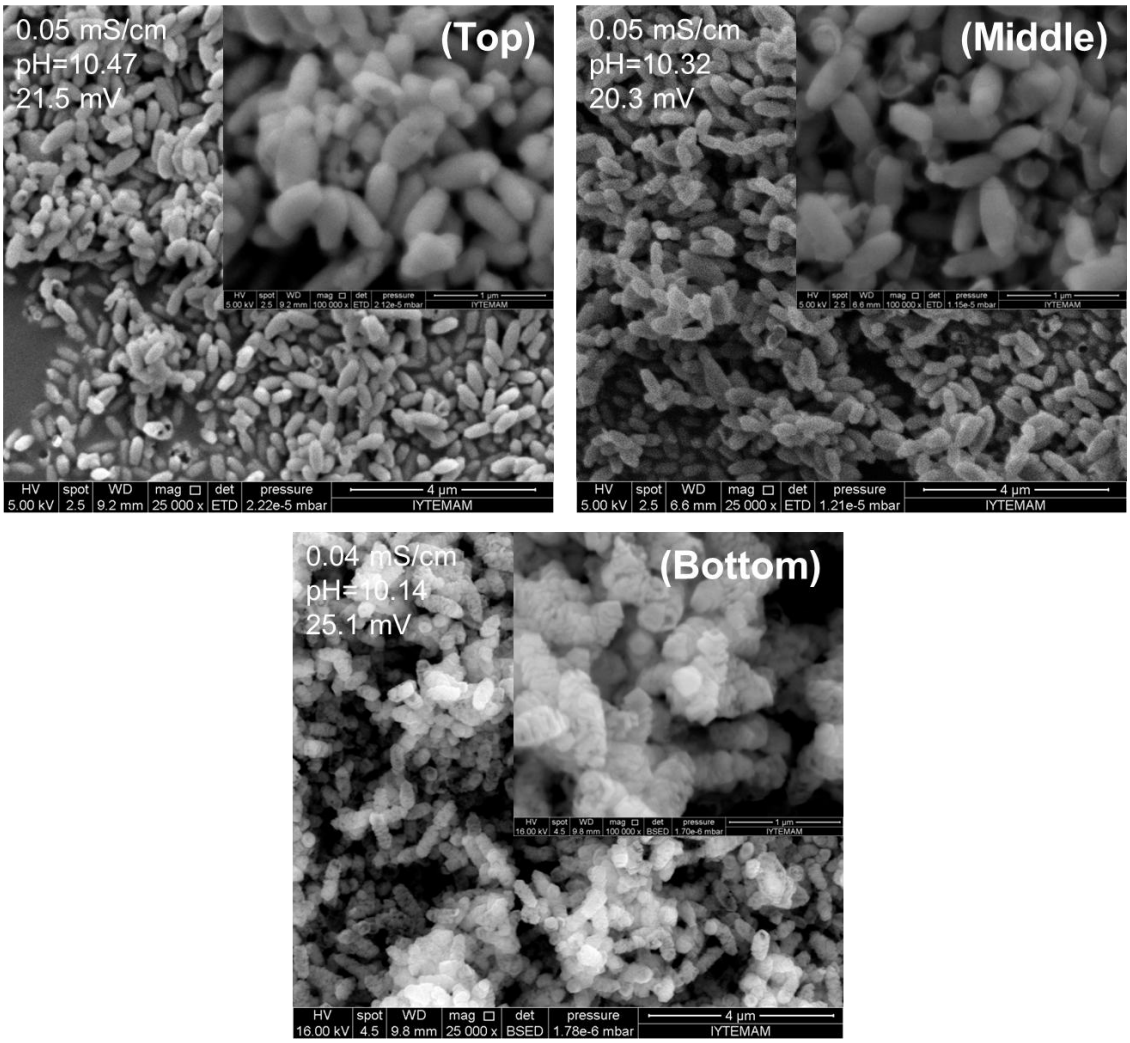

Figure 4.28. SEM images of the precipitates obtained from different CO_2 injection levels (25000x and 100000x magnification).

The XRD patterns of the precipitates obtained from different CO_2 injection levels was shown in Figure 4.29. According to the XRD patterns of precipitates, the strong and sharp diffractions indicate that all samples were all calcite. Also, there were no any different peaks detected. Any impurity or any different $CaCO_3$ crystalline form was not observed.

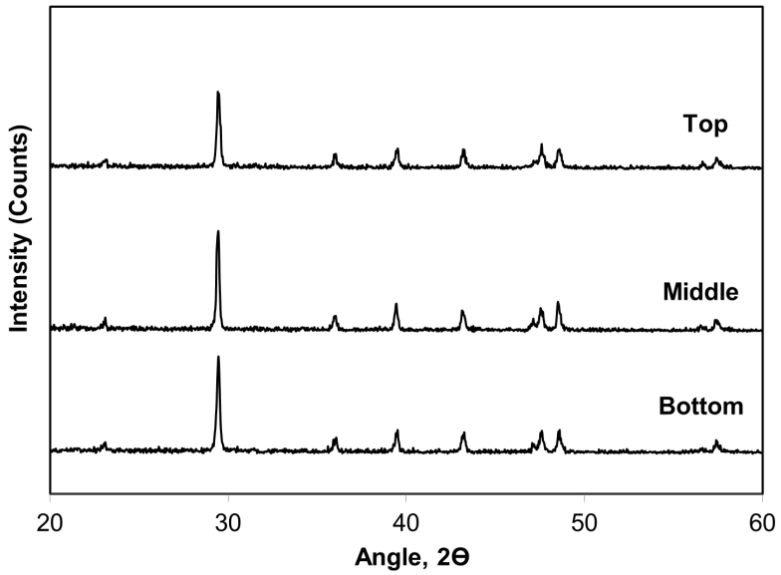

Figure 4.29. XRD patterns of the precipitates obtained from different CO_2 injection levels.

4.6. Effect of Stirring Rate and Slopped Stirring on $CaCO_3$ Production

In order to investigate the effects of stirring rate on calcite precipitation, two different CO_2 injection methods were used one is the circular pipe and the other is the helix pipe.

4.6.1. Stirring Rate with Circular Pipe

Precipitated calcium carbonates were produced by CO_2 injection with a circular pipe at the top and bottom levels of the reactor. Stirring rate was changed for each experiment between 0 rpm to 1000 rpm. Stirring rate was not examined above 1000 rpm due to the vortex occurring in the solution. The conductivity and pH values both of CO_2 injection at the top and bottom levels of reactor were shown in Figure 4.30a-b.

As shown in Figure 4.30a, there is not a strong correlation between the stirring rate and precipitation time when CO_2 injection was injected at the bottom of the reactor. When the stirring rate was increased, the precipitation time slightly decreases. It was concluded that average reaction time was nearly 10 min while the CO_2 bubbles were

injected at the bottom of the reactor. On the other hand, as shown in Figure 4.30b, there is a strong correlation between the stirring rate and the precipitation time when the CO_2 was injected at the top of the reactor. When the stirring rate was increased, the precipitation time increased. In other words, the dissolution rate was decreased at high stirring rate. It was concluded that reaction time was affected by the stirring rate when the CO_2 was injected at the top of the reactor. When the stirring velocity increases, the rate of precipitation was seen to decrease.

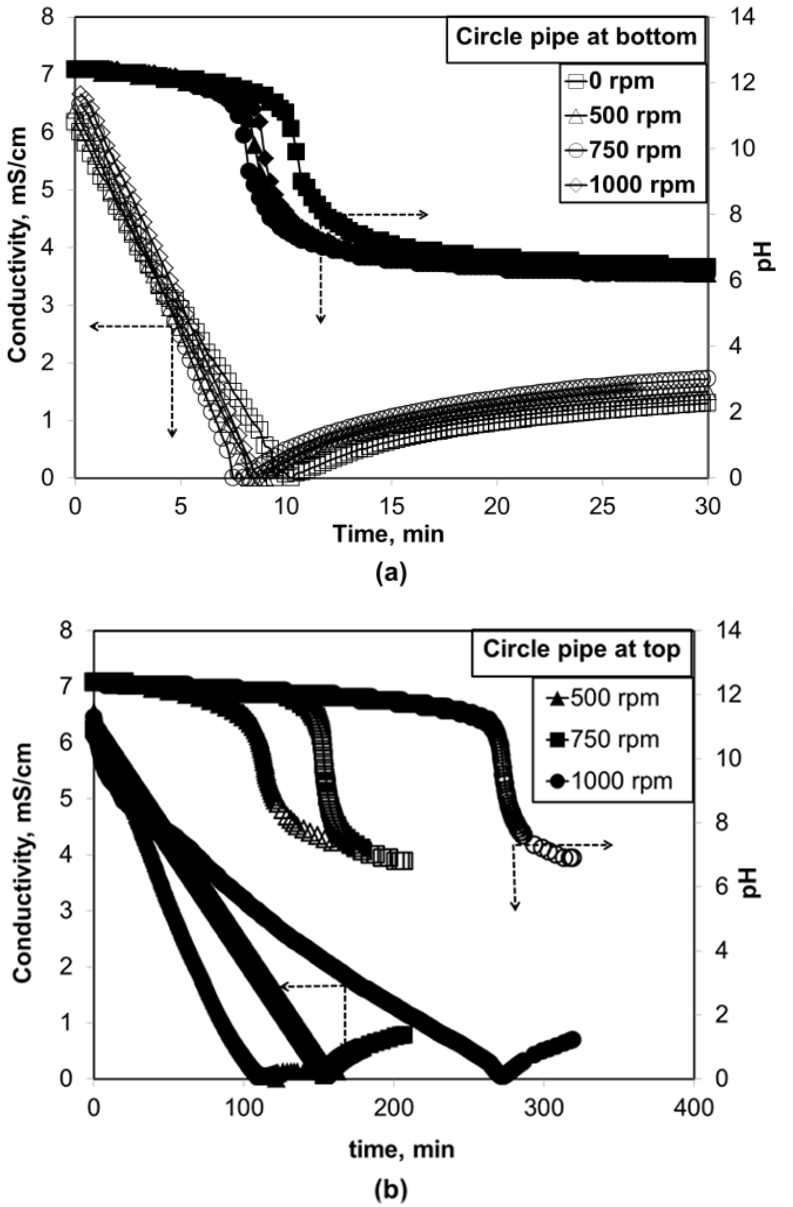

Figure 4.30. The conductivity and pH changes of solution in different stirring velocity (a) CO_2 injection from the bottom (b) CO_2 injection from the top.

Figure 4.31a-b shows the change of average particle size of precipitates at different stirring rate at the bottom and top CO_2 injection levels. As shown in Figure 4.31a, when the CO_2 was injected at the bottom of the reactor, the particle sizes were seen to increases although the crystallization rates were not significantly affected. The increase in particle size could be due to coagulation. Figure 4.31b shows the average particle size when CO_2 was injected at the top of the reactor at different stirring rates. When the stirring rate increases, the precipitation rate decreases as the dissolution was lower when the CO_2 was injected at the top of the reactor. It was concluded that the particle sizes were affected very much at different stirring rates when the CO_2 bubbles were injected at the top of the reactor. When the stirring rate was higher the particle sizes were lower than the CO_2 injection was conducted at the surface of the reactor. Therefore, high stirring rate could be more suitable to obtain calcite particles in submicron sizes while CO_2 bubbles were injected into the system from the top of the reactor.

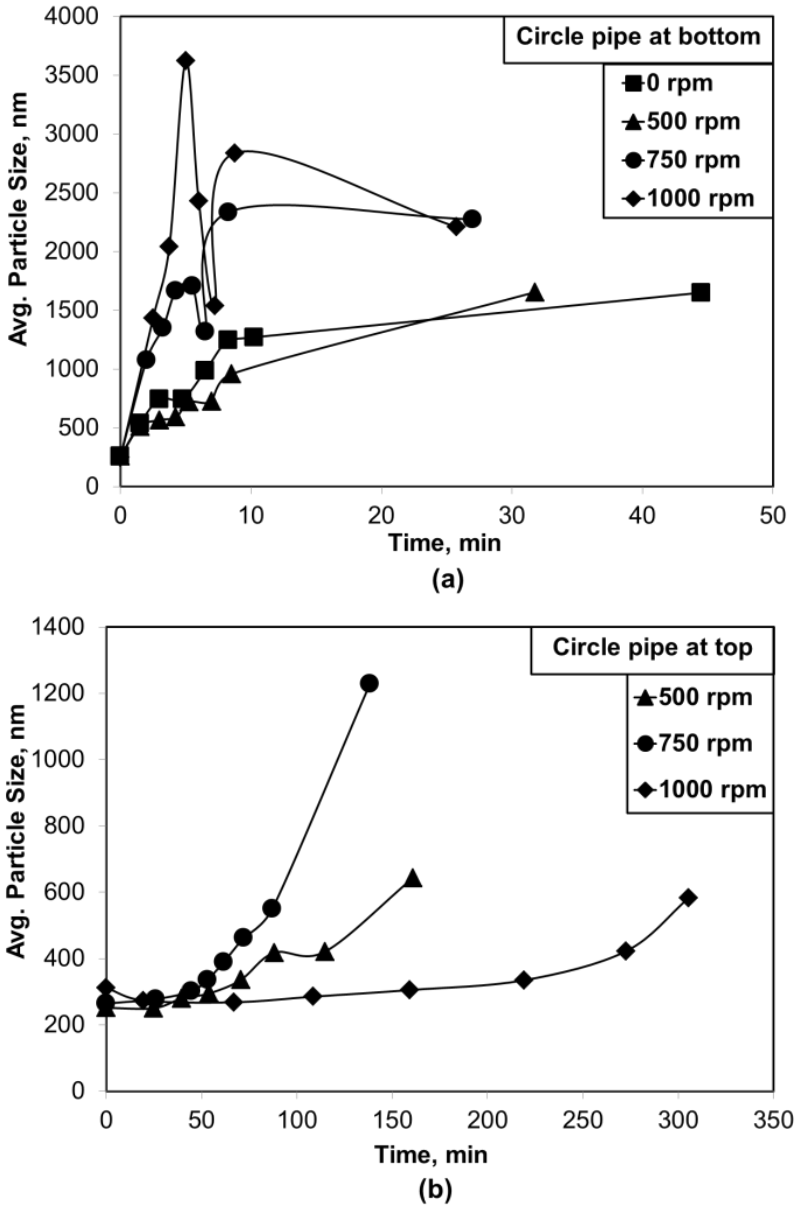

Figure 4.31. The average particle size changes of solution in different stirring velocity (a) CO_2 injection from the bottom (b) CO_2 injection from the top.

Figure 4.32a-b shows the change in zeta potential values for particles at different stirring rates for the bottom and top CO_2 injection levels. As shown in Figure 4.32a, nearly same zeta potential values were obtained for different stirring rates when the CO_2 was injected at the bottom. A sharp increase was observed at about +45 mV at the beginning of the reaction. At this period, the primary calcite particles were nucleated and dispersed in to the solution. Then, a sharp decrease was observed at about +30 mV at the late stages of the crystallization. At this point, some particles were seen calcite to coagulate. This is supported by the average particle size as given in Figure 4.31b. When

the CO_2 was injected at the top of the reactor, the zeta potential showed similar trend for the different stirring rates as shown in Figure 4.32b. When the stirring rate was high at 1000 rpm, zeta potential stayed higher than +40 mV indicating a highly mono-dispersed particle in the solution.

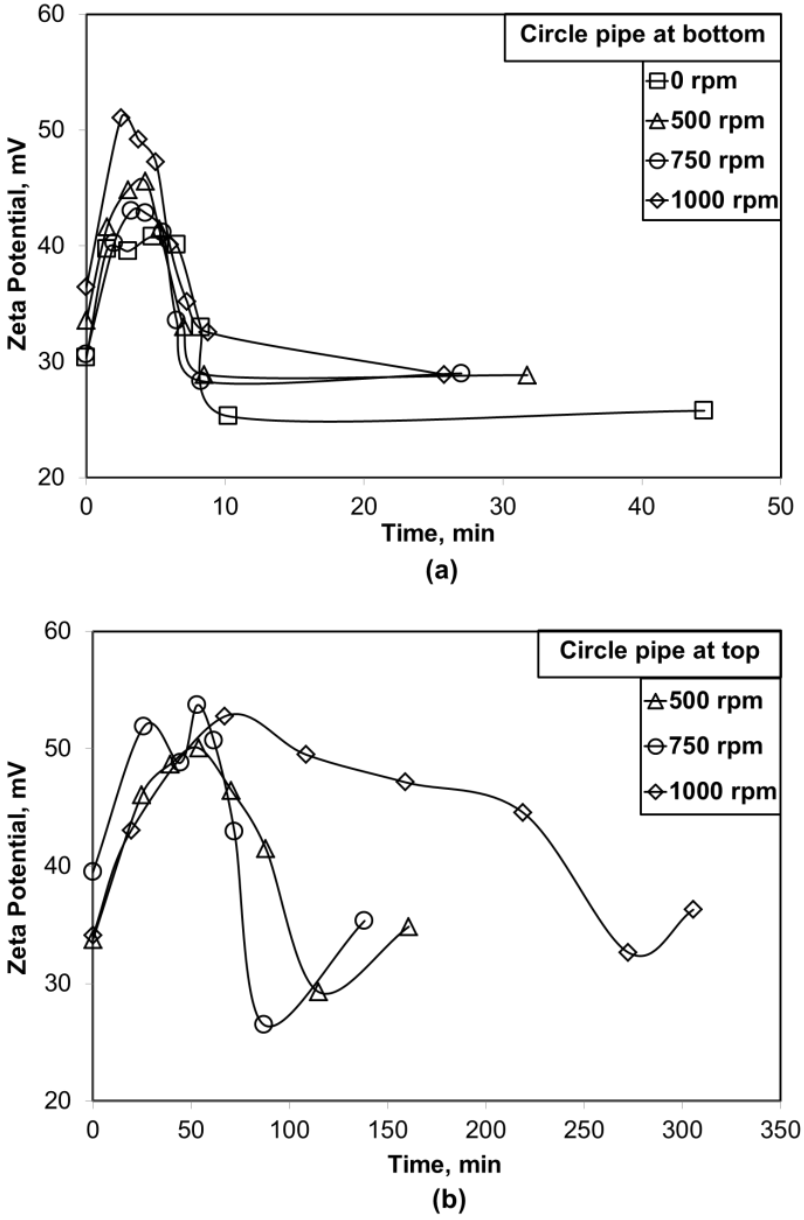

Figure 4.32. The zeta potential changes of solution in different stirring velocity (a) CO_2 injection from the bottom (b) CO_2 injection from the top.

SEM images of the particles obtained at different CO_2 injection level and different stirring rates were obtained. Figure 4.33 shows SEM images of precipitate calcite particles, which were obtained by CO_2 injection from the bottom level while

solution was stirring at 0 rpm. Before the CO_2 injection, at stage (0), there was a mixture of large and small amorphous $Ca(OH)_2$ and $CaCO_3$ particles. As soon as CO_2 injected into the solution, cubic chain-like $CaCO_3$ particles were observed at stage (1), (2) and (3). Then these cubic particles oriented into elongated spindle-like shape as the crystallization progresses at stage (4), (5) and (6). This structure could be occurred in solution as a result of high CO_2 amount in solution according to injection level. When the reverse reaction is started, pH was nearly 7, at stage (7) dissolved cubic calcite forms were observed in solution due to the dissolution of particles.

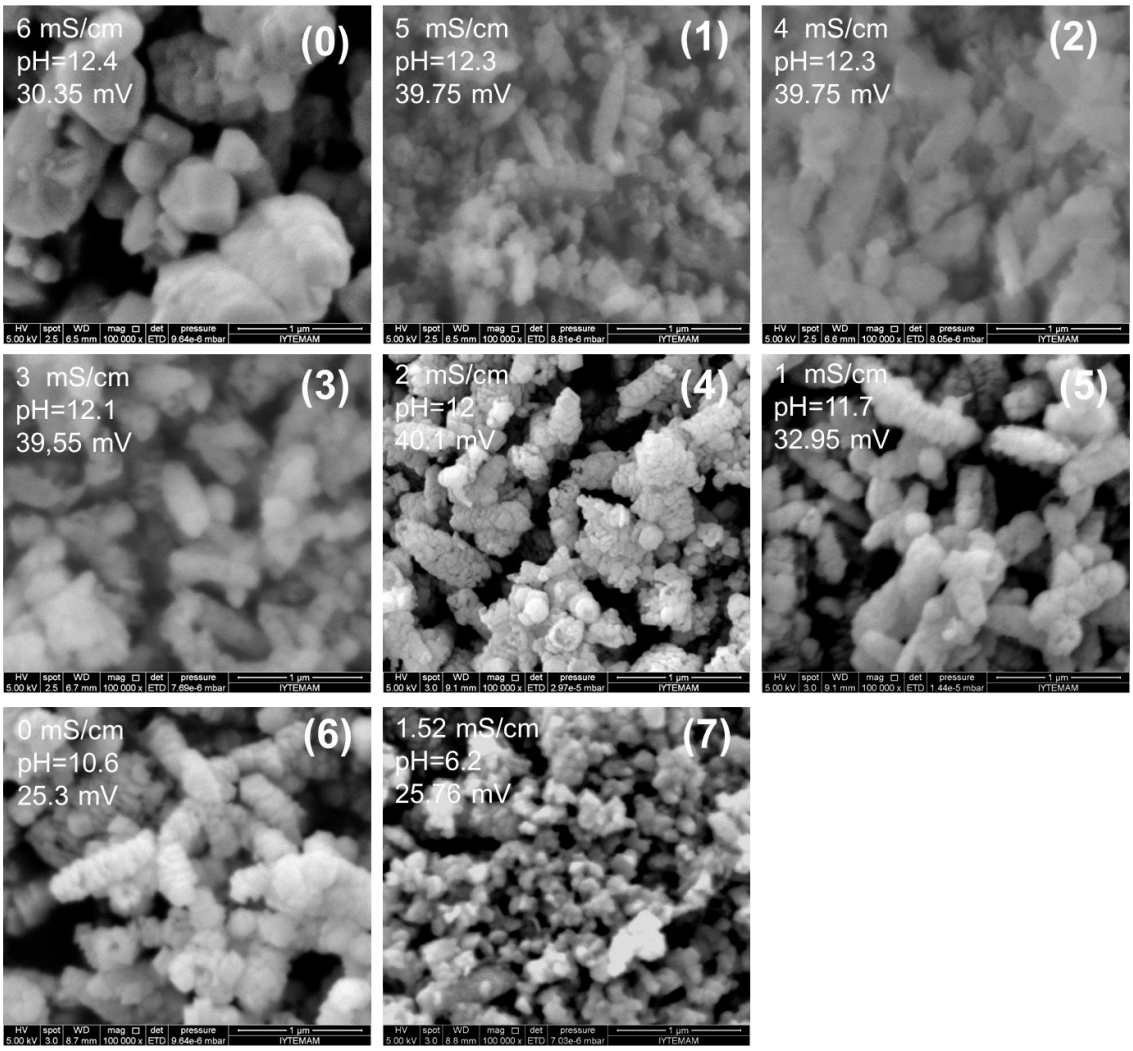

Figure 4.33. SEM images of precipitate according to advancement of reaction while stirring at 0 rpm by CO_2 injection at the bottom of reactor.

Figure 4.34 shows SEM images of precipitate calcite particles, which were obtained by CO_2 injection from the bottom level while solution was stirring at 500 rpm.

Before the CO_2 injection, at stage (0), there was a mixture of large spindle-like $CaCO_3$ particles. This may be result of dissolution CO_2 from the air and converted $Ca(OH)_2$ into $CaCO_3$. As soon as CO_2 injected into the solution, cubic chain-like $CaCO_3$ particles were observed at stage (1) and (2). Then, these cubic particles oriented into elongated spindle-like shape when crystallization was progressed at stage (3), (4) and (5). This structure could be occurred in solution as a result of high CO_2 amount in the solution at low level of injection. When the reaction was completed at stage (6), elongated chain-like calcite particles were formed and finally chain-like calcite particles were converted into aggregated cubic particles at stage 7 due to the reverse reactions at pH nearly 6.

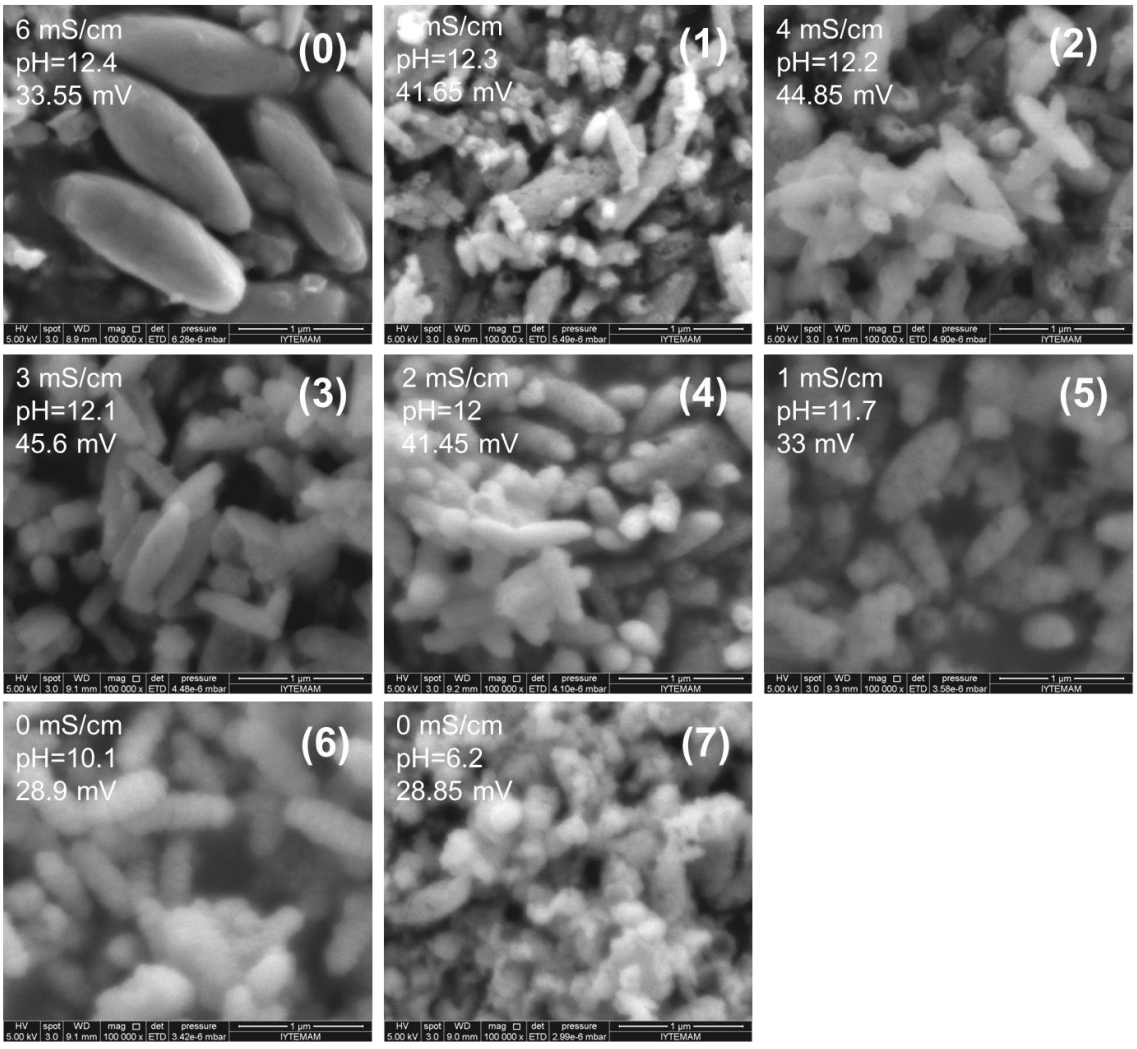

Figure 4.34. SEM images of precipitate according to advancement of reaction while stirring at 500 rpm by CO_2 injection at the bottom of reactor.

Figure 4.35 shows SEM images of precipitate calcite particles, which were obtained by CO_2 injection from the bottom level while solution at stirring rate of 750 rpm. Before the CO_2 injection at stage (0), there was a mixture of large spindle-like $CaCO_3$ particles. This may be result of dissolution of CO_2 from the air some impurity from the $Ca(OH)_2$ solution. As soon as CO_2 was injected into the solution, aggregated $CaCO_3$ particles were observed at stage (1), (2) and (3). Then these cubic particles were oriented into chain-like nona calcite particles as crystallization progressed at stage (4), (5) and (6). These nano particles could occur as a result of high stirring rate. High stirring rate may also cause dispersion of chain-like structure. When the reaction was completed at stage (6), chain-like aggregated calcite particles were formed. At stage 7, chain-like particles were disintegrated into highly aggregated calcite particles. This result could be the result of decomposition of crystal particles with increasing acidity of the solution.

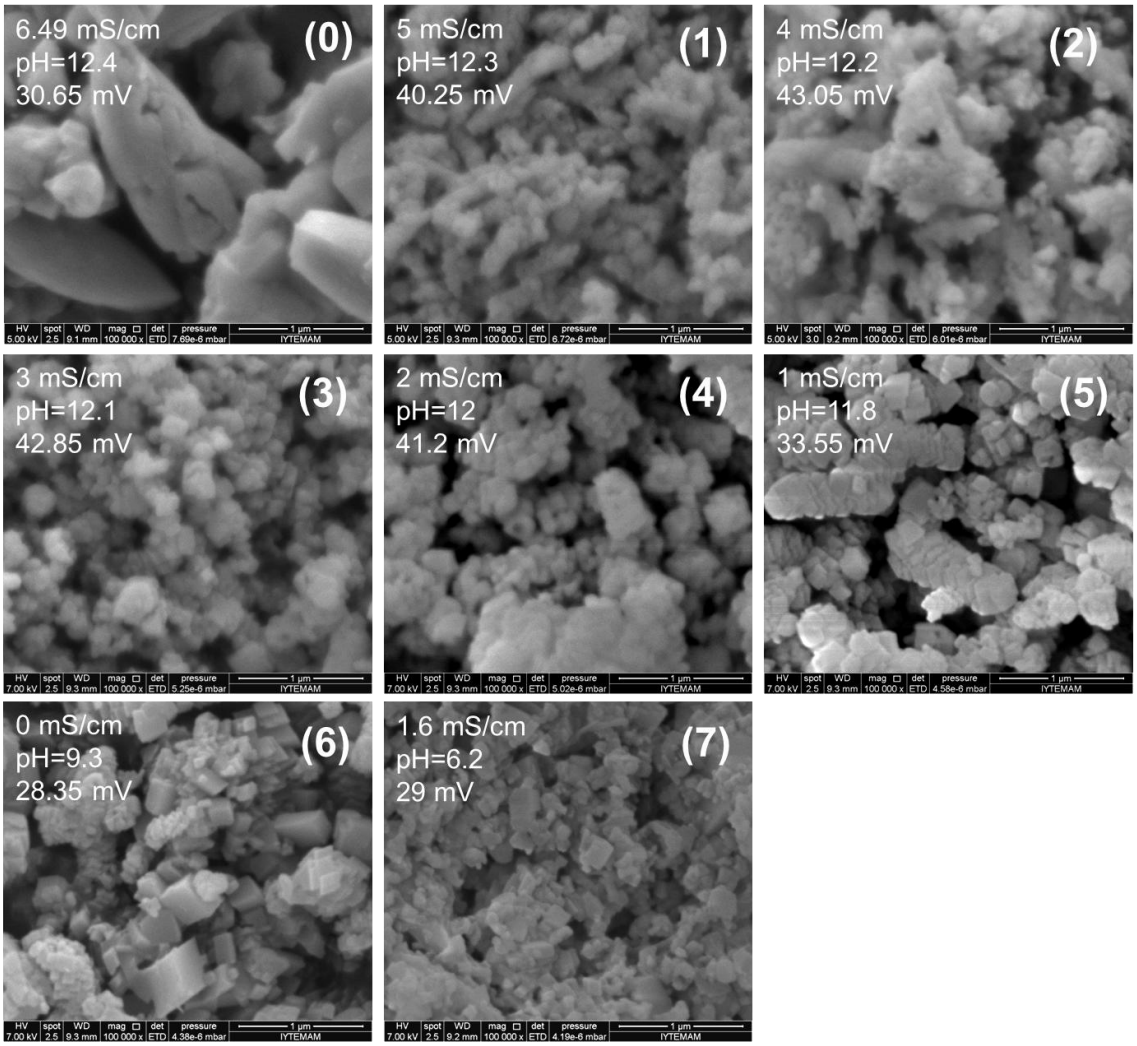

Figure 4.35. SEM images of precipitate according to advancement of reaction while stirring at 750 rpm by CO2 injection at the bottom of reactor.

Figure 4.36 shows SEM images of precipitate calcite particles, which were obtained by CO_2 injection from the bottom level while solution was stirring at 1000 rpm. Before the CO_2 injection at stage (0), there was a mixture of small and large size $CaCO_3$ particles. This may be result of dissolution CO_2 from the air and converted $Ca(OH)_2$ into $CaCO_3$ and also $CaCO_3$ impurity. As soon as CO_2 was injected into the solution, aggregated and very small cubic $CaCO_3$ particles were observed at stage (1). Spindle-like shaped chain-like calcite particles were occurred in solution at stage (2), (3) and (4). Then, these cubic particles oriented into very small cubic chain-like shape as the crystallization was progressed at stages (5) and (6). This structure could be occurred as a result of rapid stirring rate. Rapid stirring rate may cause the dispersion of chain-like particles into individual particles. When the reaction was completed at stage

(6), beside aggregated chain-like calcite particles, aggregated nano calcite particles were observed at stage 7 at low pH.

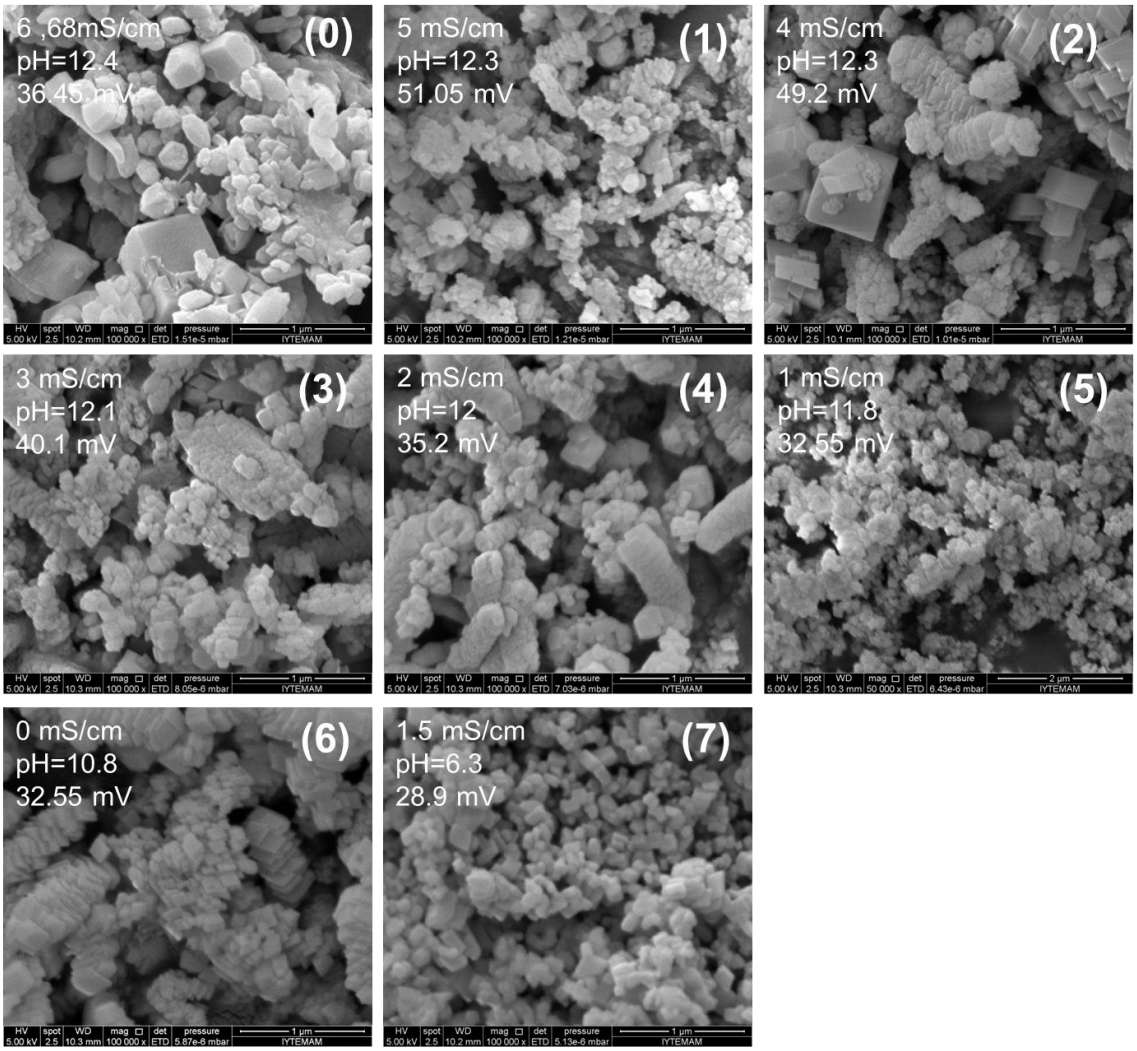

Figure 4.36. SEM images of precipitate according to advancement of reaction while stirring at 1000 rpm by CO_2 injection at the bottom of reactor.

A comparison of The SEM images of the precipitates at different stirring rates which were obtained by CO_2 injection at the bottom of the reactor shown in Figure 4.37. According to the images, chain-like and aggregated calcite crystals were produced from all of the reactions when the CO_2 was injected at the bottom of the reactor. Although morphologies of particles were not change with stirring rate, more aggregated particles were observed when the stirring velocity was lower. When the stirring rate was higher, higher aggregated nano calcite particles were produced.

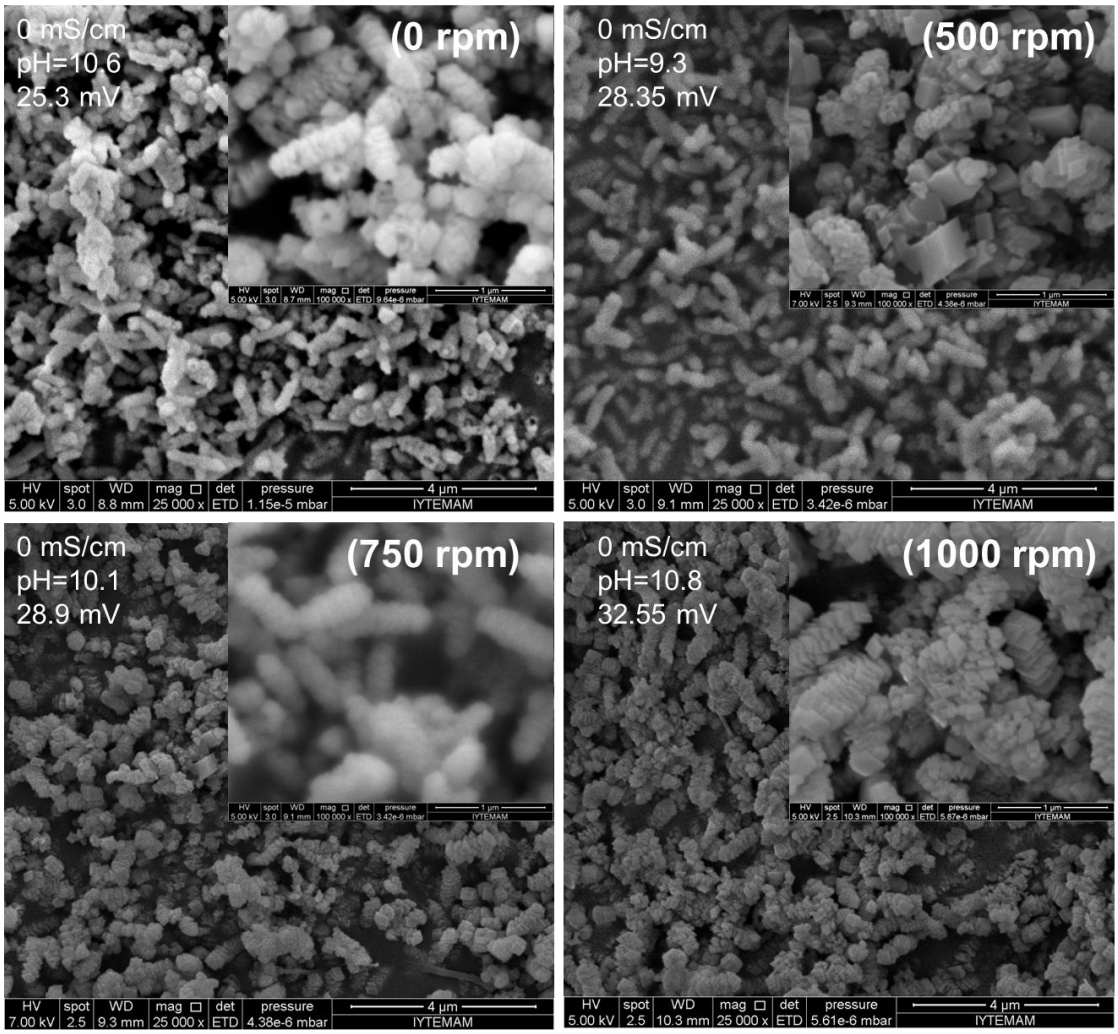

Figure 4.37. SEM images of precipitate in different stirring velocity by CO_2 injection at the bottom of reactor (25000x and 100000x magnification).

Figure 4.38 shows SEM images of precipitate calcite particles, which were obtained by CO_2 injection from the top level while solution was stirring at 500 rpm. Before the CO_2 injection at stage (0), there was a mixture of small and large size particles due to mostly impurities. As soon as CO_2 was injected into the solution, spindle-like $CaCO_3$ particles were formed at stage (1) and (2). Spindle-like shaped calcite particles oriented into very small cubic particles by crystallization at stage (3), (4) and (5). At these stages, beside cubic particles, hollow cubic particles were also observed. When the reaction was completed at stage (6), spindle-like calcite particles were obtained.

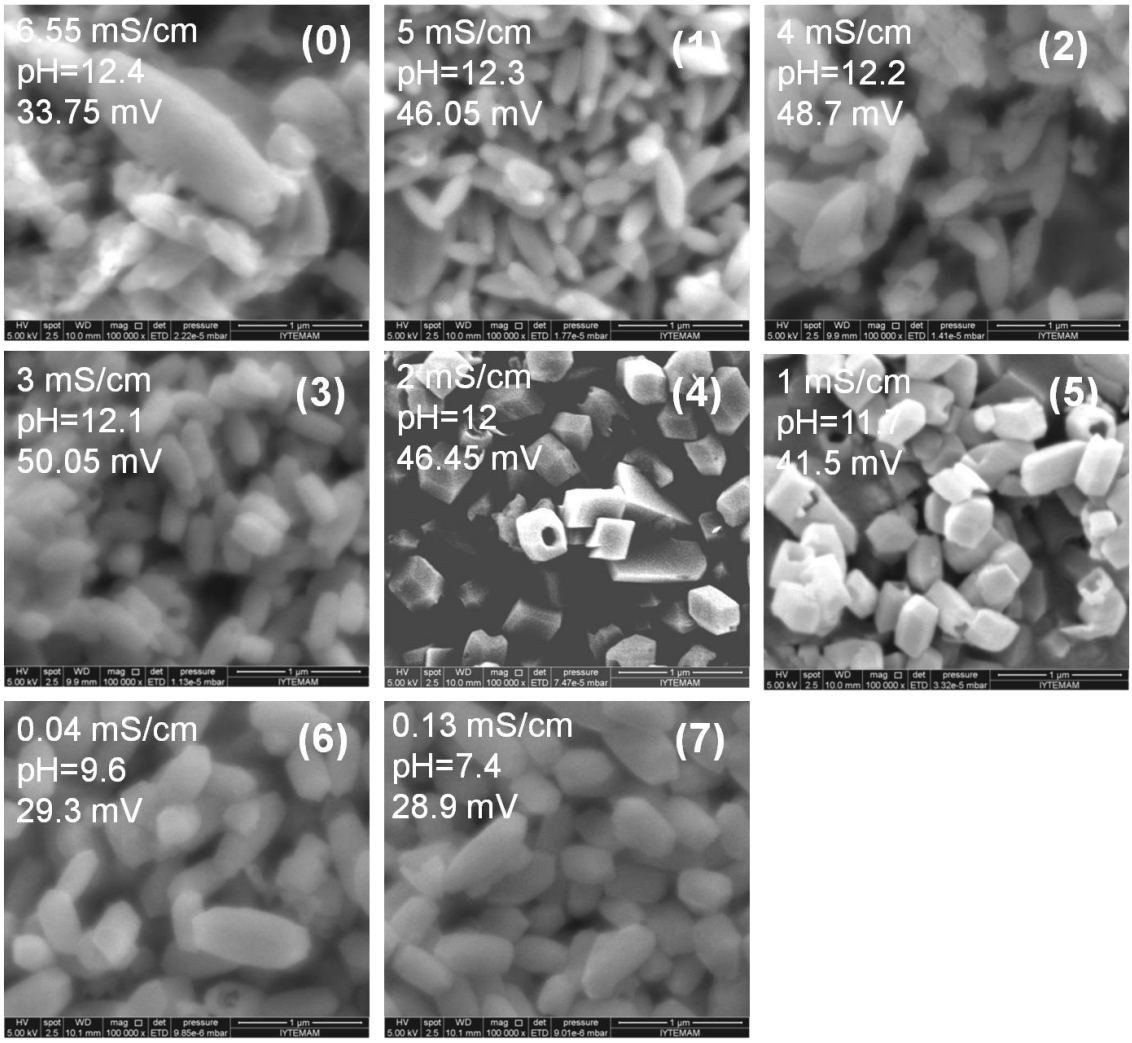

Figure 4.38. SEM images of precipitate according to advancement of reaction while stirring at 500 rpm by CO_2 injection at the top of reactor.

Figure 4.39 shows SEM images of precipitate calcite particles, which were obtained by CO_2 injection from the top level while solution was stirring at 750 rpm. Before the CO_2 injection at stage (0), there was a mixture of small and large size particles. As soon as CO_2 was injected into the solution, spindle-like and aggregated cubic $CaCO_3$ particles were formed at stage (1), (2) and (3). More individual cubic calcite particles were observed with some hollow shape after crystallization at stage (4), (5) and (6). At these stages, increasing CO_2 in solution could cause to dissolve particles. When the reaction was completed at stage (6) rice-like calcite particles were obtained. This may be as a result of high stirring rate. Finally, more individual calcite particles with some cracks were observed in solution at stage at low pH.

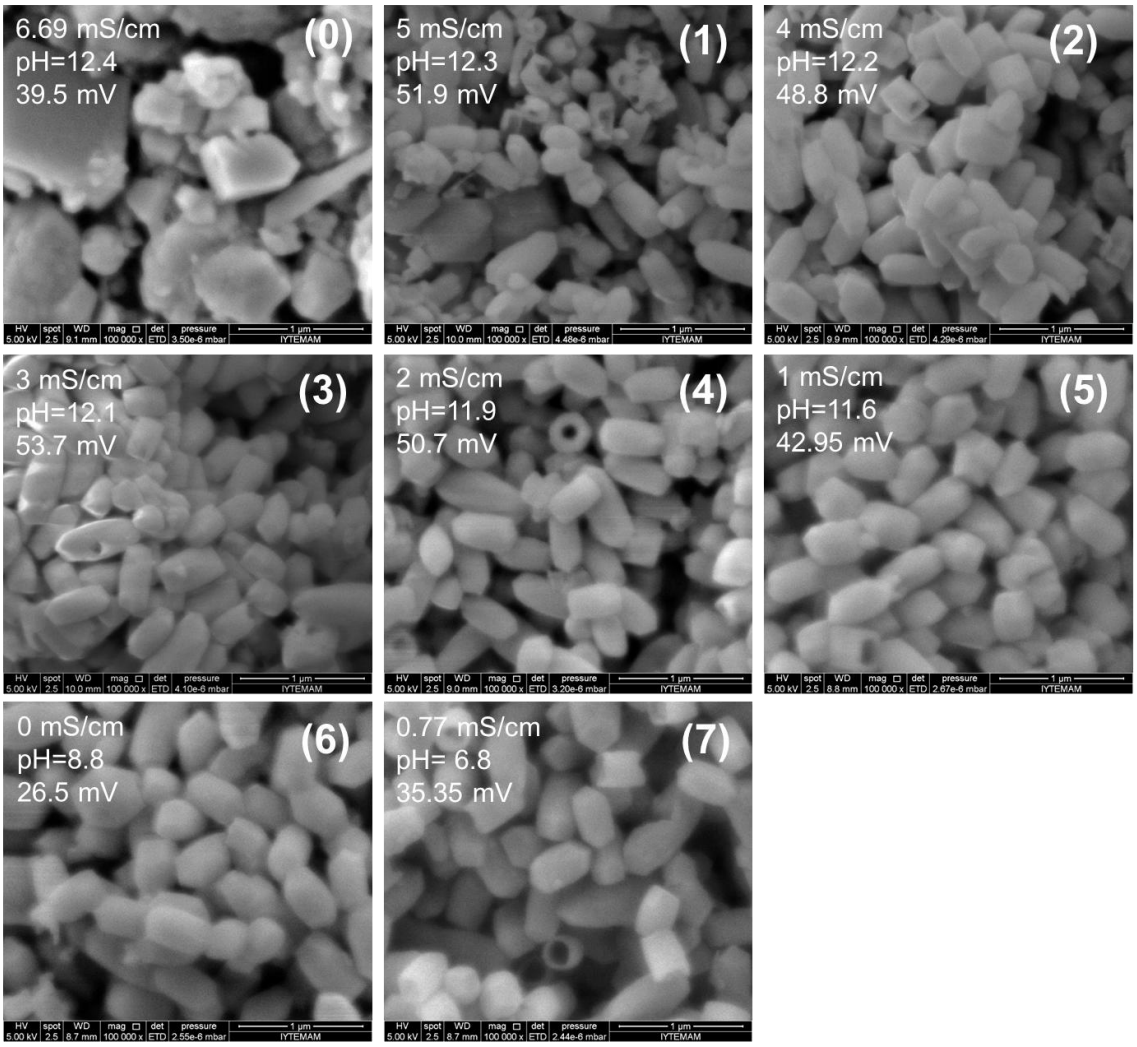

Figure 4.39. SEM images of precipitate according to advancement of reaction while stirring at 750 rpm by CO_2 injection at the top of reactor.

Figure 4.40 shows SEM images of precipitated calcite particles, which were obtained by CO_2 injection from the top level while solution was stirring at 1000 rpm. As shown in the figure, as soon as CO_2 injected into the solution, spindle-like $CaCO_3$ particles were formed at stages (1), (2) and (3). More individual and hollow nano calcite particles were obtained at stages of (4) and (5). When the reaction is completed at stage (6), individual cubic calcite particles were observed. This may be a result of rapid stirring rate. Finally, calcite particles some aggregation was obtained at stage (7) when pH was 7.

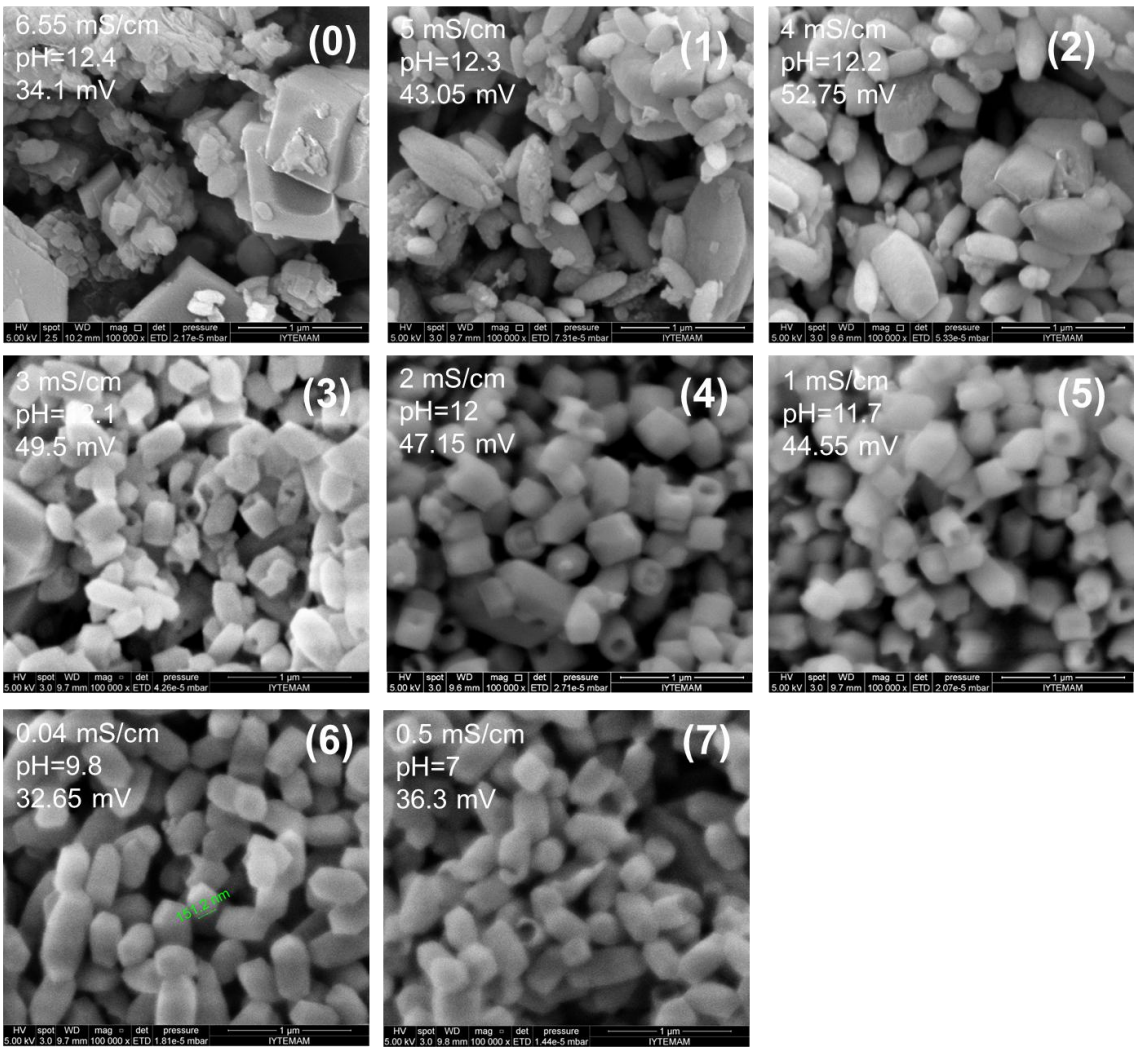

Figure 4.40. SEM images of precipitate according to advancement of reaction while stirring at 1000 rpm by CO_2 injection at the top of reactor.

The SEM images of precipitates at different stirring rates which were obtained by CO_2 injection at the top of reactor were shown in Figure 4.41. According to the images, rhombohedral cubic and mono dispersed $CaCO_3$ crystals were produced from each crystallization rates when CO2 was injected at the top of the reactor. Although morphologies of particles were not changed with stirring rate, more aggregated particles were observed when the stirring rate was slower.

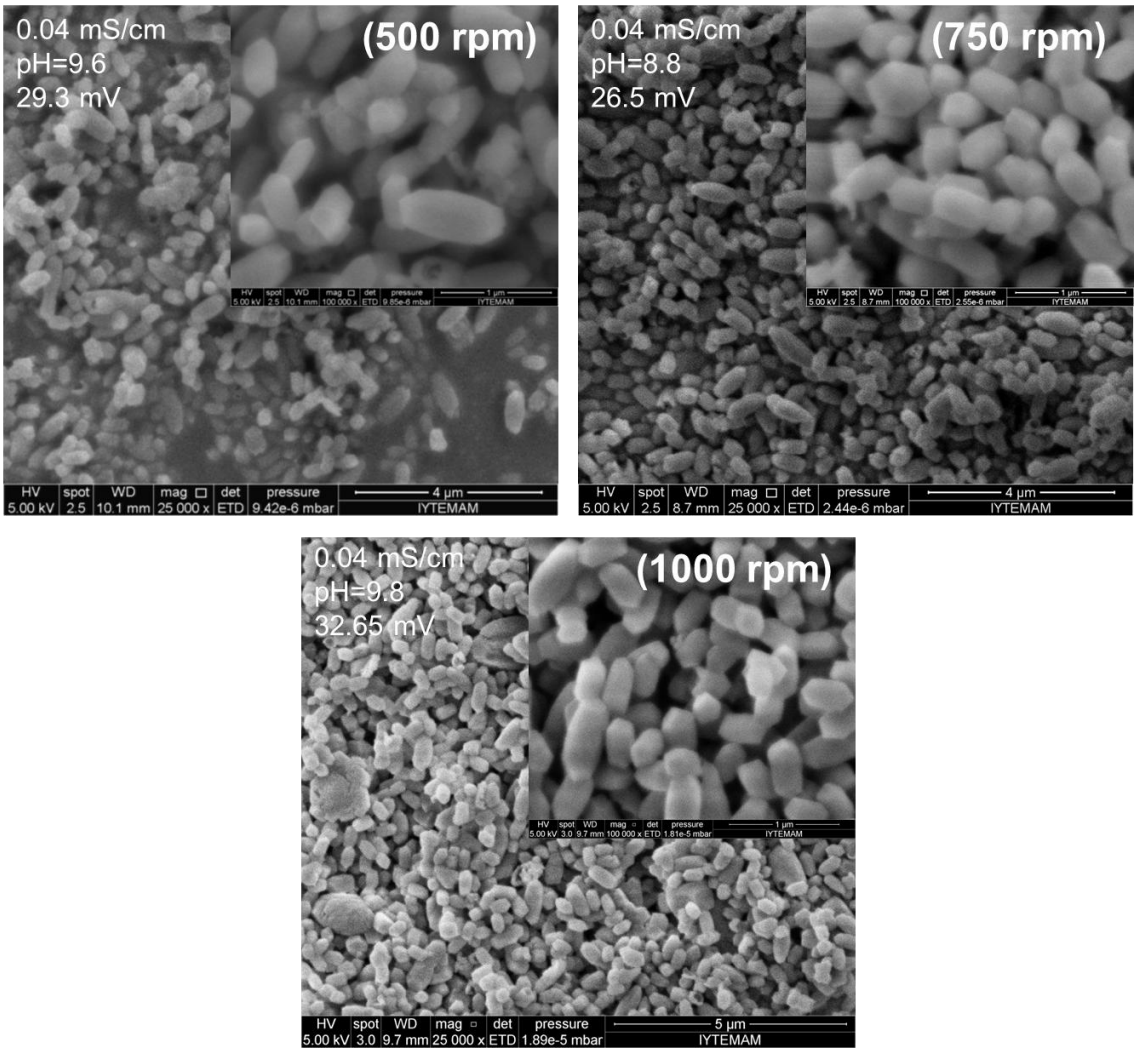

Figure 4.41. SEM images of precipitate in different stirring rates by circular pipe CO_2 injection (25000x and 100000x magnification).

4.6.2. Stirring Rate with Helix Pipe

Precipitated $CaCO_3$ were produced by using a helix pipe for CO_2 injection at the top level of the bubble reactor. Stirring rate was varied for each experiment between 0 rpm to 1000 rpm. Stirring rate was not examined above 1000 rpm due to the vortex in the solution. The conductivity and pH values at different stirring rates were shown in Figure 4.42. As shown in the figure, the crystallization is dependent on the way where CO_2 was injected in the bubble reactor. As the helix pipe is very close to the surface, the completion of the crystallization took extensive time. As the stirring rate was increased, precipitation time of reaction was decreased. CO_2 injection with the helix pipe provides a narrow reaction area in the reactor. We called this area as the crystallization region.

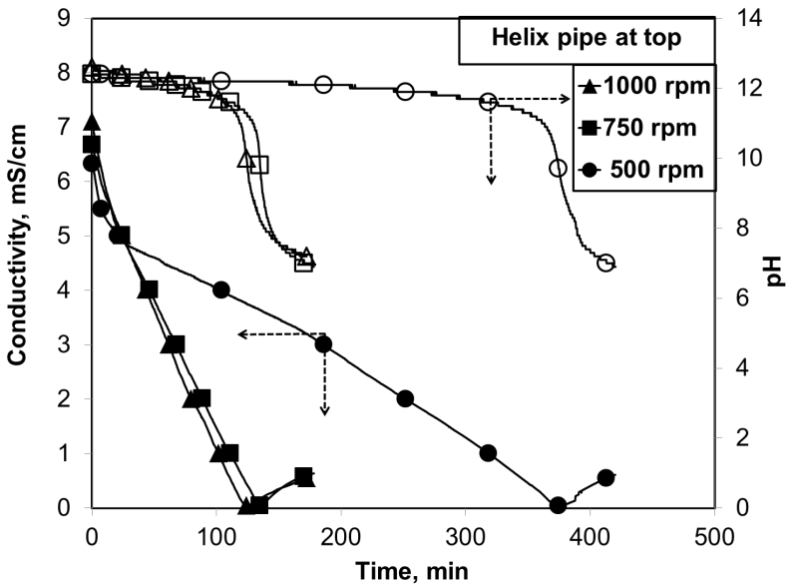

Figure 4.42. The conductivity and pH changes of solution in different stirring velocity by helix pipe CO_2 injection from the top level.

Figure 4.43 shows the zeta potential and average particle size of precipitates obtained at different stirring rates CO_2 injection by the helix pipe from the top level. As shown in the figure, all produced particles were obtained in submicron sizes. There is reverse proportionality between the stirring rate and average particle size. When the stirring rate increased, the time for the completion of the reaction decreased. Zeta potential values were obtained reversely proportional to the particle size as expected. An increase in the zeta potential was observed at the beginning of the reaction. At this period, the primary small calcite particles may be nucleated and dispersed in solution. Then, a decrease in zeta potential was observed at the final stages of reaction. At this point, calcite particles may form coagulation. It was concluded that production of nano particles during prolonged period of reaction is possible when the stirring rate is low.

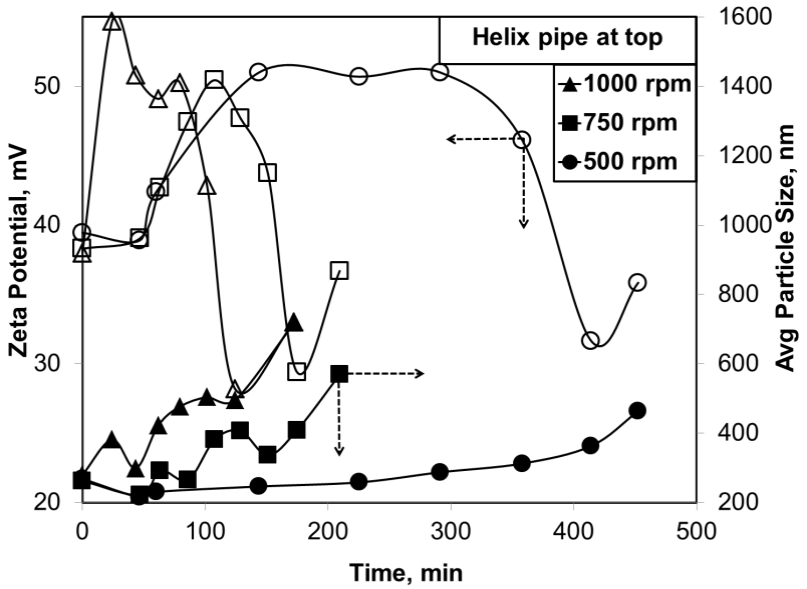

Figure 4.43. The zeta potential and average solution size changes of precipitate in different stirring velocity by helix pipe CO_2 injection from the top level.

Figure 4.44 shows the SEM images of precipitate calcite particles, which were obtained by CO_2 injection with the helix pipe from the top level while the solution was stirred at 500 rpm. Before the CO_2 injection, at stage (0), there was a mixture of small and large size particles due most probably to impurities in the $Ca(OH)_2$ solution. As soon as was CO_2 injected into the solution, spindle-like small $CaCO_3$ particles were formed at stages (1) and (2). More individual small calcite particles were synthesized at stages (4) and (5). When the reaction was completed at stage (6), individual and almost mono-dispersed calcite particles were obtained. This may be the result of the CO_2 injection from a small region in the bubble reactor into the solution. Some hollow calcite particles were also synthesized at the late stage of crystallization at stage (7), where pH was 7.

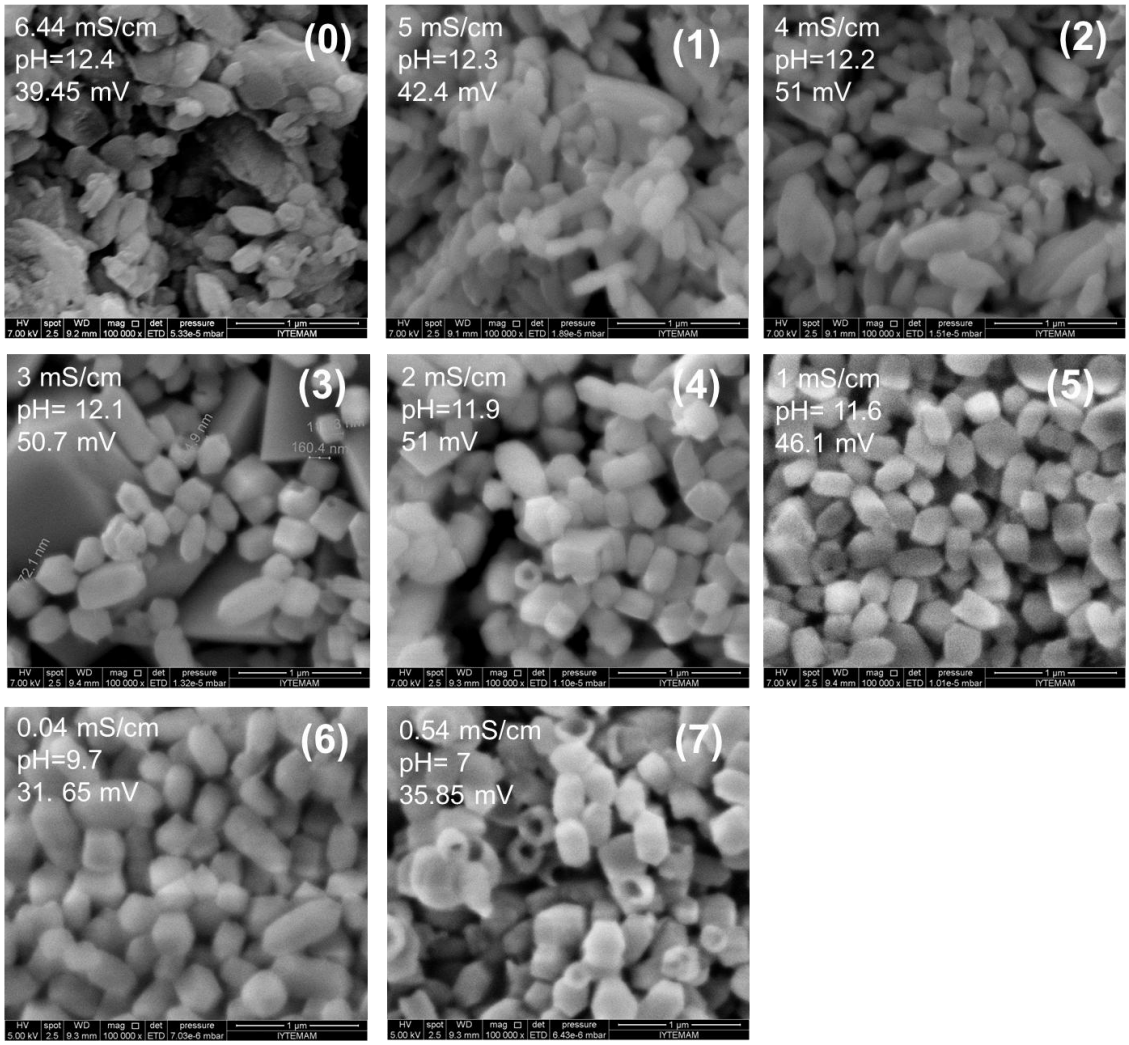

Figure 4.44. SEM images of precipitate according to advancement of reaction while stirring at 500 rpm by helix pipe CO_2 injection at the top of reactor.

Figure 4.45 shows the SEM images of precipitated calcite particles, which were obtained by CO_2 injection with the helix pipe from the top level while the solution was stirred at 750 rpm. As soon as CO_2 was injected into the solution, spindle-like $CaCO_3$ particles were obtained at stages (1), (2) and (3). Then, these spindle-like particles oriented into smaller particles, where some of the particles were converted into the hollow structure at stages (4) and (5). This structure could be occurred as a result of high stirring rate. When the reaction was completed at stage (6), some aggregation was observed among the calcite particles; finally, hollow calcite particles were formed at stage (7) where pH was 7.

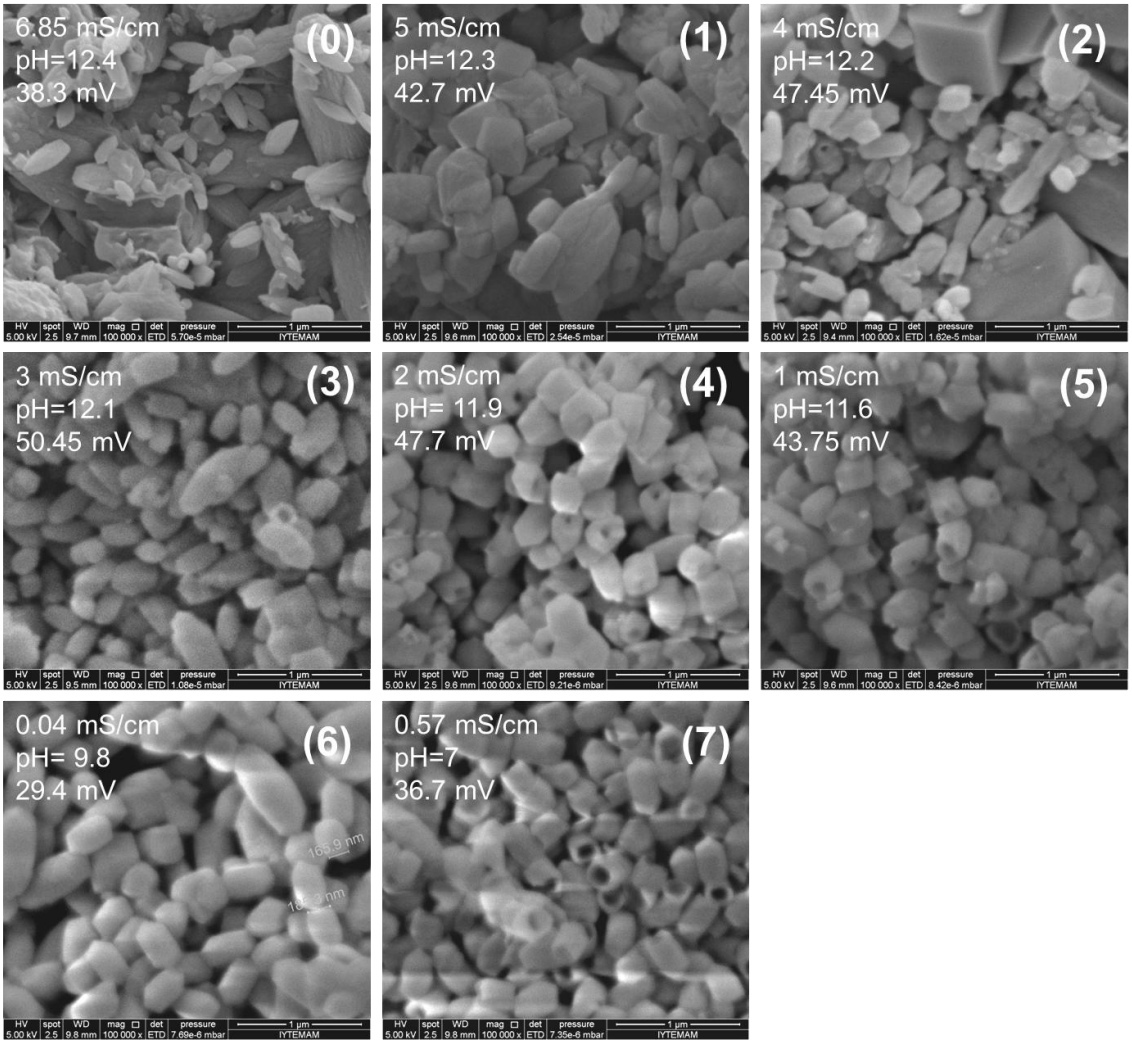

Figure 4.45. SEM images of precipitate according to advancement of reaction while stirring at 750 rpm by helix pipe CO_2 injection at the top of reactor.

Figure 4.46 shows the SEM images of precipitate calcite particles, which were obtained by CO_2 injection with the helix pipe from the top level while the solution was stirred at 1000 rpm. Larger particles as well as small spindle-like particles were formed at the initial stages. However, these particles could also be due to some impurities that were appeared in the SEM images. When the CO_2 was injected into the solution, besides larger cubic $CaCO_3$ particles, spindle-like $CaCO_3$ particles were also observed at stages (1), (2), (3) and (4). Then these spindle-like particles were oriented into smaller cubic particles as the crystallization progressed at stages (5) and (6). This structure could be occurred as a result of rapid stirring rate. If the stirring rate was increased, smaller particles could be obtained due to well- dispersion of particles. At stage (7), hollow calcite particles were formed at pH value was 7.

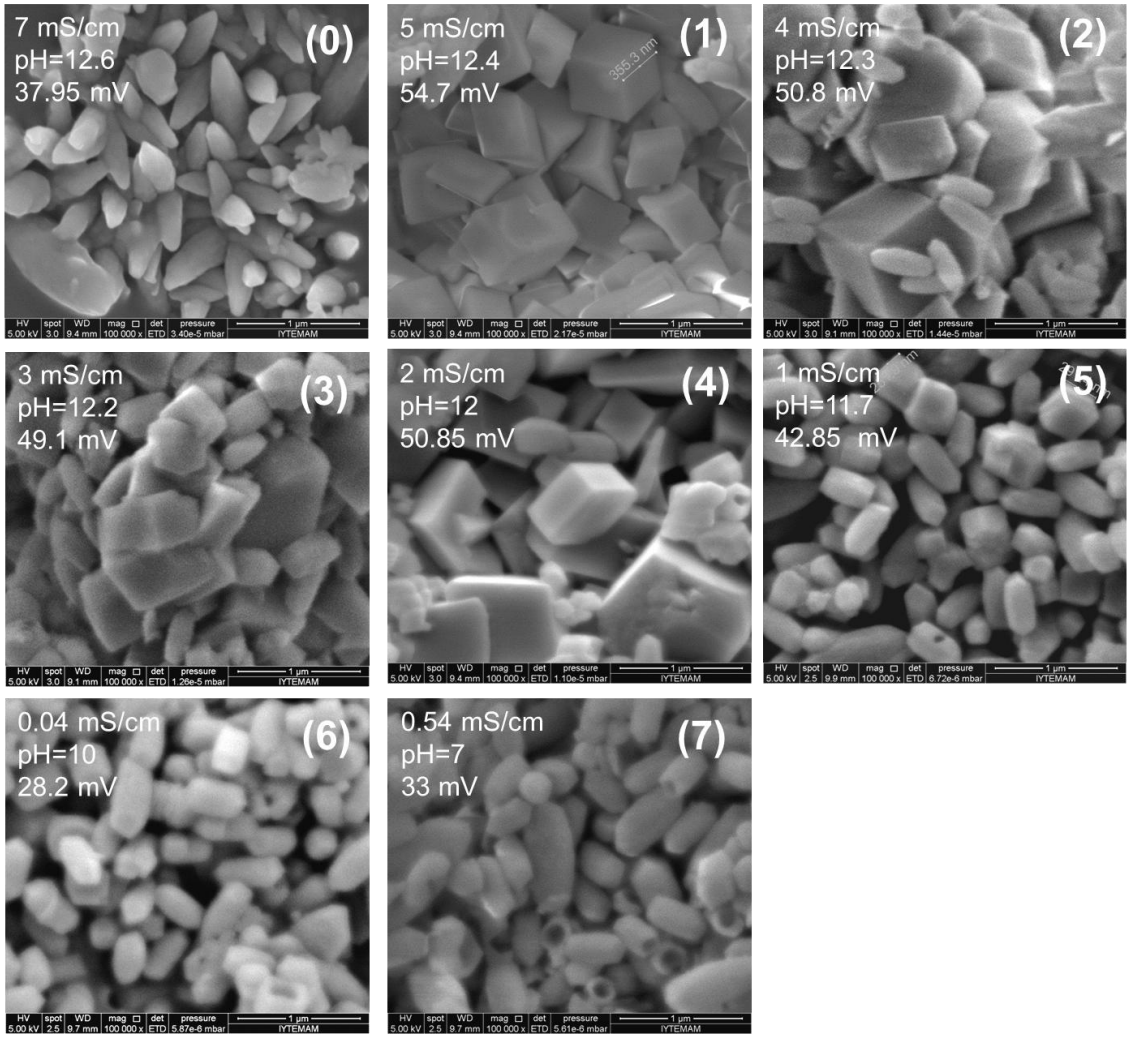

Figure 4.46. SEM images of precipitate according to advancement of reaction while stirring at 1000 rpm by helix pipe CO_2 injection at the top of reactor.

The SEM images of precipitates in different stirring rates which were obtained by CO_2 injection with the helix pipe at the top of the bubble reactor were shown in Figure 4.47. According to the images, all produced particles were in submicron sizes. Rhombohedral and mono dispersed $CaCO_3$ crystals were produced from all three reactions. Although morphologies of particles were not change with stirring velocity, more aggregated and cubic particles were obtained when the stirring rate was slower.

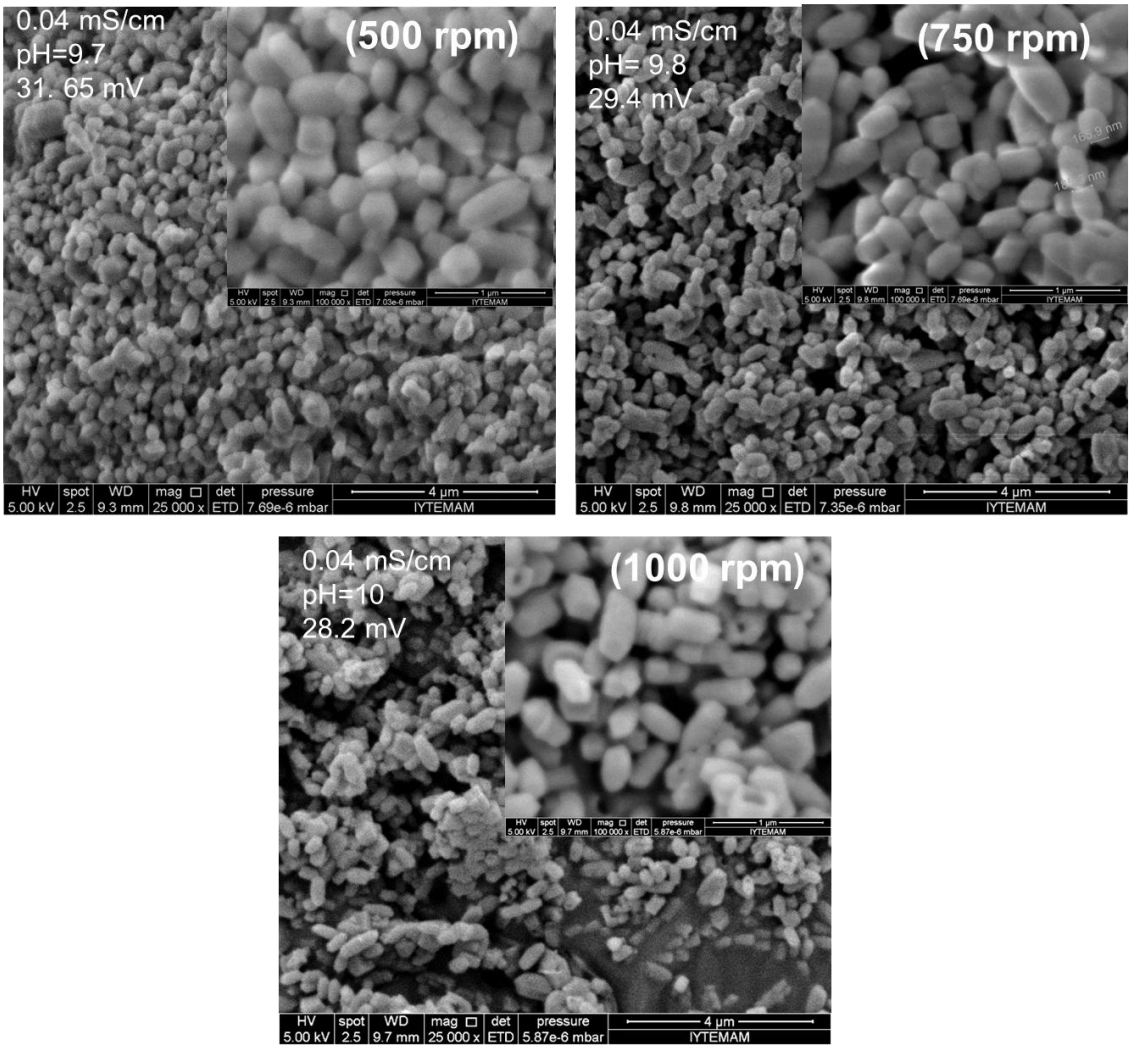

Figure 4.47. The SEM images of precipitate in different stirring velocity by helix pipe CO_2 injection (25000x and 100000x magnification).

The XRD patterns of the precipitates obtained from different stirring rates by CO_2 injection with the helix pipe were shown in Figure 4.48. According to XRD patterns of the precipitates, the strong and sharp diffractions indicate that all samples were well known to calcite. Also, there were no any different peaks detected. Any impurity or any different $CaCO_3$ crystalline form was not observed.

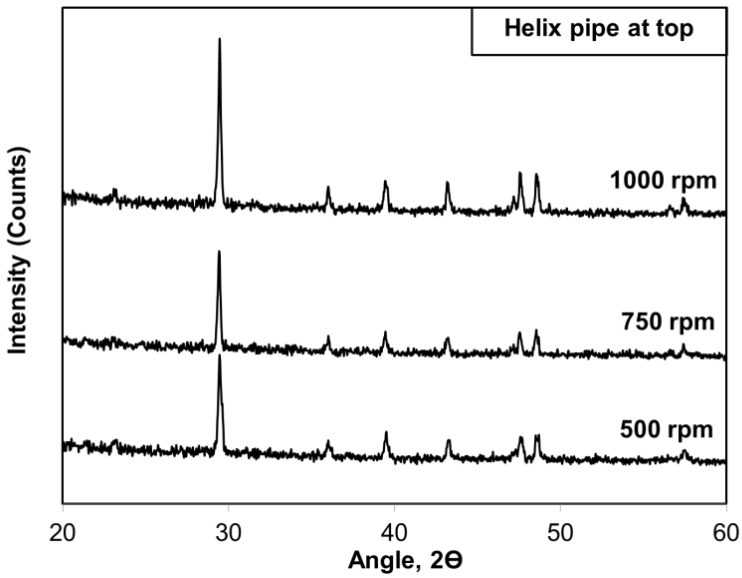

Figure 4.48. The XRD patterns of precipitate in different stirring velocity by helix pipe CO_2 injection.

4.7. Effect of CO_2 Flow Rate on $CaCO_3$ Production

Precipitated $CaCO_3$ were produced by the carbonation method in our developed semi batch bubble reactor at different CO_2 flow rates. CO_2 diffusion into the solution took place from individual bubbles at low CO_2 flow rates. When the CO_2 flow rate was increased, more bubbles were observed in the solution. The different bubbling in scheme would cause a remarkable effect on the morphology and size of particles. For this purpose, CO_2 injection with the helix pipe were performed in a 15 mM $Ca(OH)_2$ solution at different CO_2 flow rates including 80 ml/min, 220 ml/min and 420 ml/min. Reaction times and pH-conductivity curves for different flow rates were given in Figure 4.49. As shown in the figure, the crystallization rate was higher for the higher CO_2 flow rates.

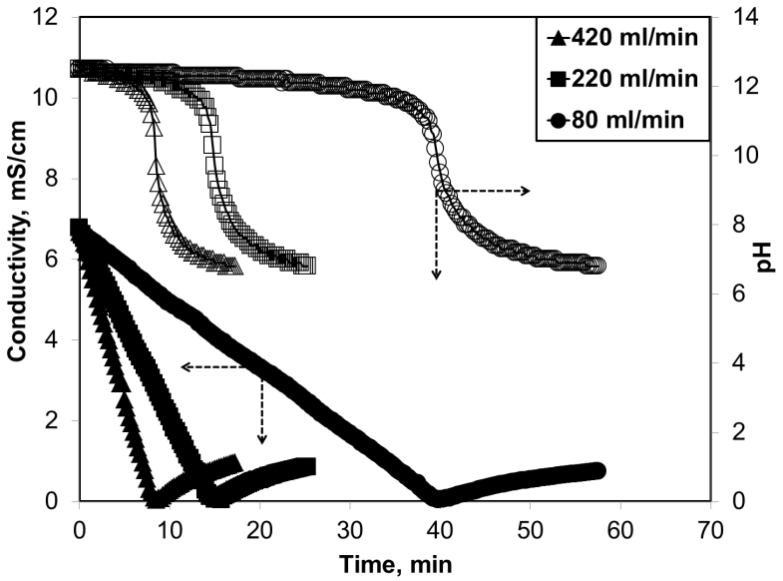

Figure 4.49. pH and conductivity changes of solution at different CO_2 flow rate.

Figure 4.50a-b shows the zeta potential and average particle sizes of the precipitates at different CO_2 flow rates by CO_2 injection with the helix pipe from the top level. As shown in Figure 4.50-a, zeta potential curves showed similar behavior. An increase in zeta potential was seen at the beginning of crystallization. At this period, the primary small calcite particles may be nucleated and dispersed in the solution. Then, a decrease in zeta potential was below the +30 mV value at the late stages of crystallization. At this point, calcite particles seen were started to forms some coagulation. As shown in Figure 4.50-b, produced particles were in submicron sizes for low CO_2 flow rates. There is reverse proportionality between the CO_2 flow rate and average particle size. When the CO_2 flow rate was increased, the time to complete the crystallization way decreased and the average particle size suddenly increased. It was concluded that production of nano particles during prolonged period of crystallization could be possible when the CO_2 flow rate is lower for the proposed system.

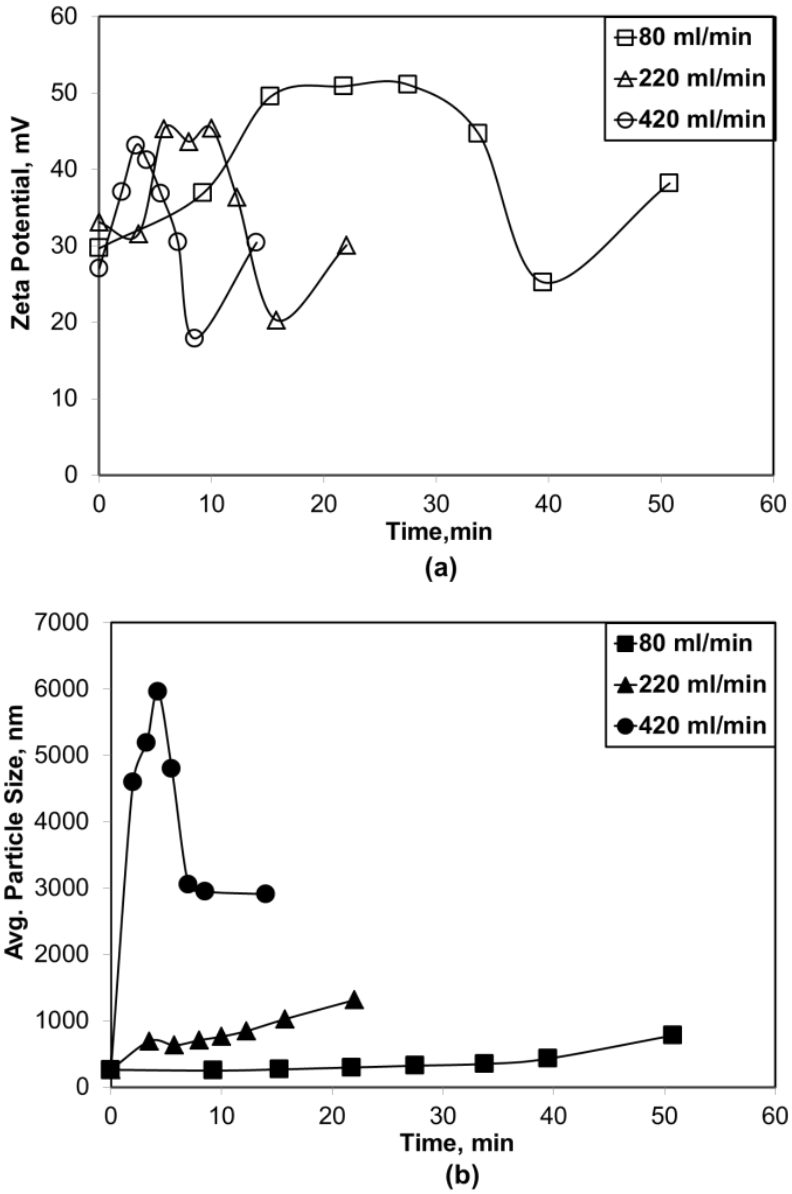

Figure 4.50. (a) Zeta potential and (b) average particle changes of solution at different CO_2 flow rate.

Figure 4.51 shows the SEM images of precipitated calcite particles, which were obtained by helix pipe CO_2 injection from the top level while CO_2 flow rate was at 80 ml/min. Before the CO_2 injection, at stage (0), there was a mixture of large particles due probably to impurities in the $Ca(OH)_2$ solution. As soon as CO_2 was injected into the solution, spindle-like $CaCO_3$ particles were obtained at stages (1), (2) and (3). Some large cubic smooth $CaCO_3$ particles were also observed at stage (3). This particles may be an impurity in $Ca(OH)_2$ powder and seen in the SEM image. Then, these spindle-like particles were oriented into smaller particles, some of which were formed hollow

structure at stages (4), (5) and (6). Finally hollow calcite forms converted into spindle-like shape due to dissolution and recrystallization mechanism at stage (7).

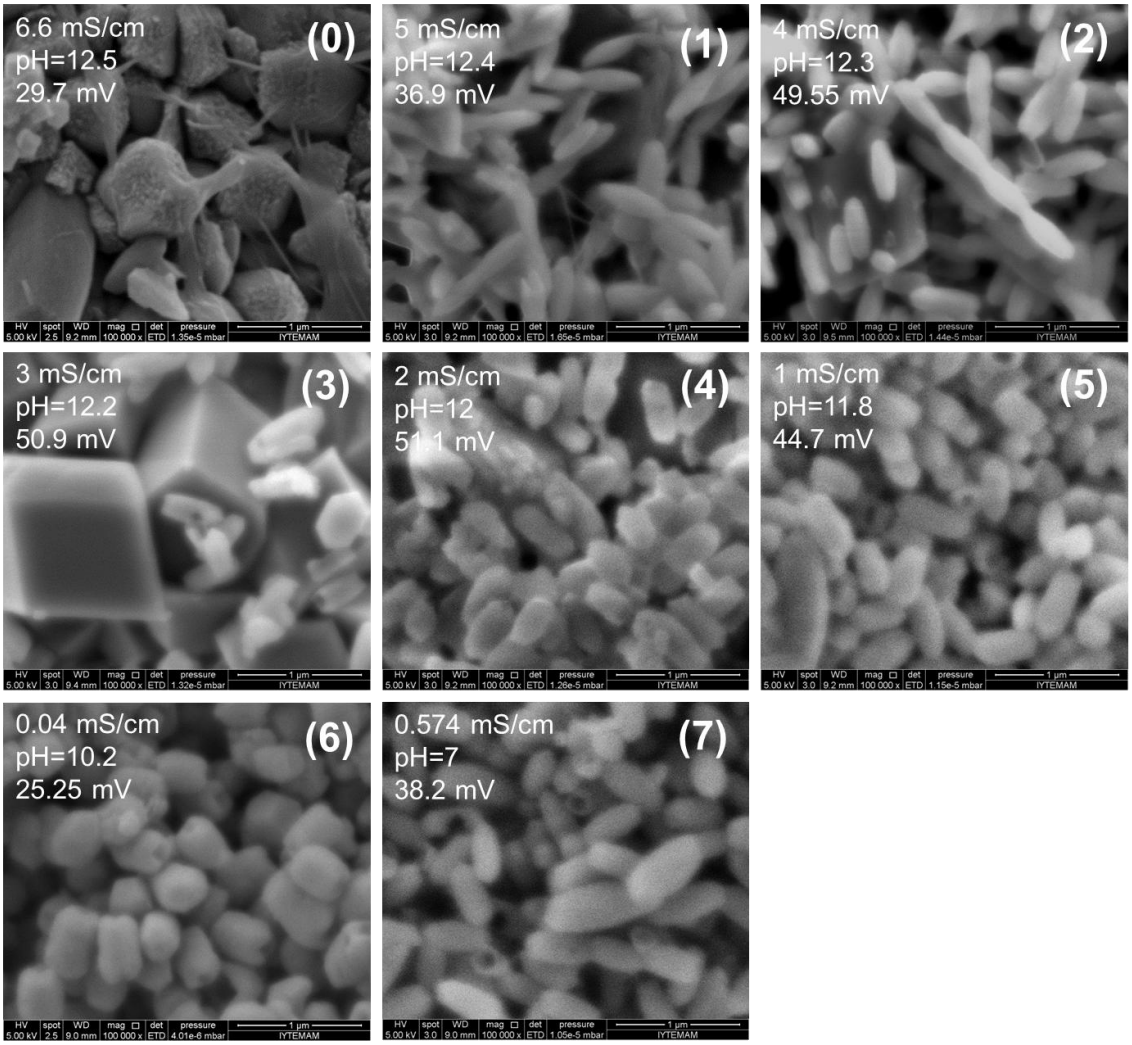

Figure 4.51. SEM images of precipitate according to advancement of reaction obtained from 80 ml/min CO_2 flow rate.

Figure 4.52 shows the SEM images of precipitated calcite particles, which were obtained by CO_2 injection with the helix pipe from the top level while the CO_2 flow rate was at 220 ml/min. Before the CO_2 injection, at stage (0), there was larger particles were observed. As soon as CO_2 was injected into the solution, spindle-like $CaCO_3$ particles were observed at stages (1), (2) and (3). Some small $CaCO_3$ particles were formed as a result of these spindle-like particles at stages (4) and (5). When the reaction was completed, at stage (6), these small particles were oriented into chain-like particles by

crystallization. Finally, some decomposition was observed in chain-like forms into spindle-like shape again due to the reverse reaction of pH about 7 at stage (7).

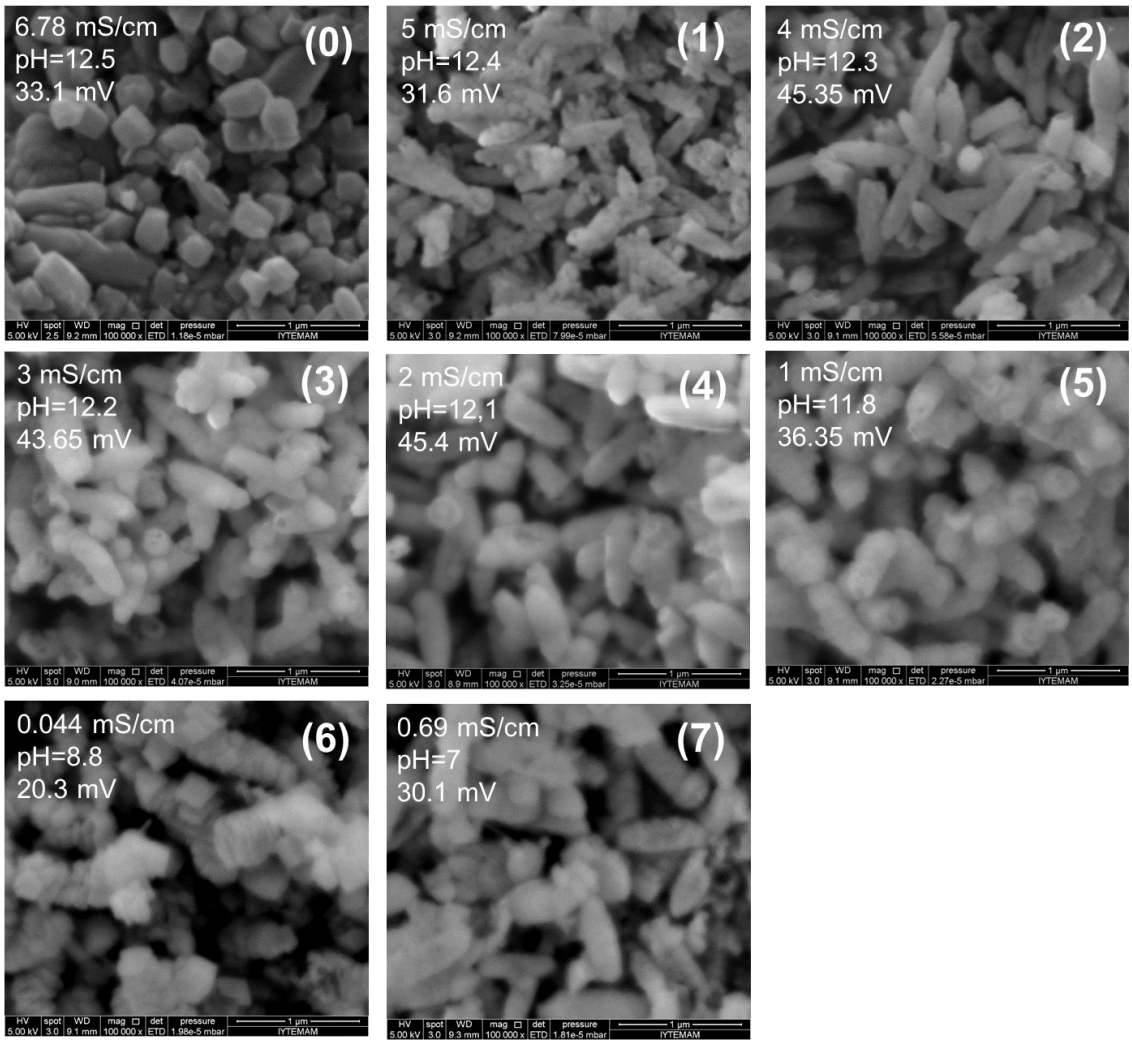

Figure 4.52. SEM images of precipitate according to advancement of reaction obtained from 220 ml/min CO_2 flow rate.

Figure 4.53 shows the SEM images of the precipitated calcite particles which were obtained by CO_2 injection with the helix pipe from the top level while the CO_2 flow rate was at 420 ml/min. Before the CO_2 injection, at stage (0), there were large particles, again due to impurities present in the $Ca(OH)_2$ solution. As soon as the CO_2 injected into the solution, very small $CaCO_3$ particles were formed in the solution. These small particles formed into aggregated particles in time. Similar images were taken in all stages. This is a result of high CO_2 flow rate. High CO_2 caused a rapid crystallization, which lead to small but an aggregation of particles.

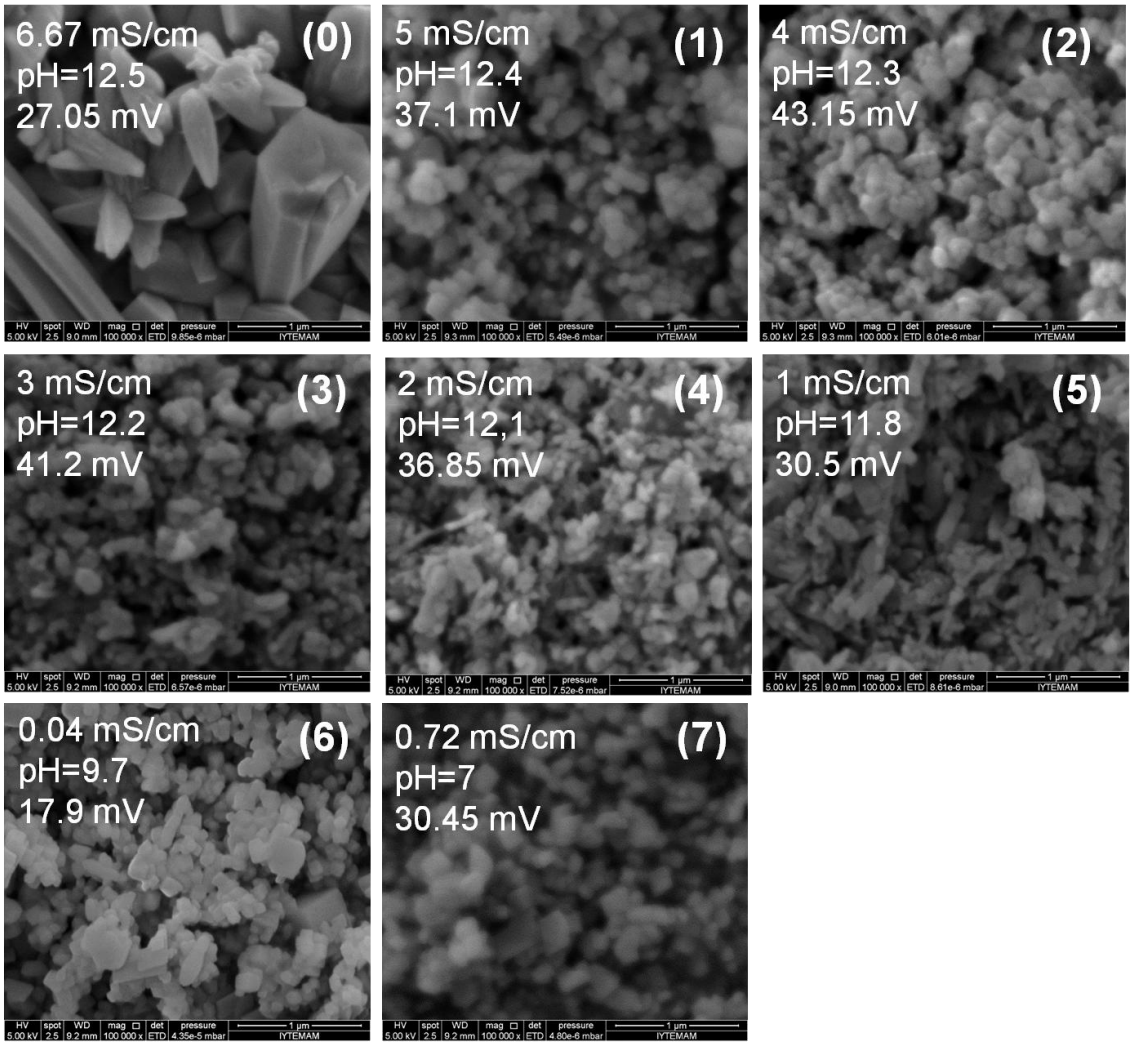

Figure 4.53. SEM images of precipitate according to advancement of reaction obtained from 420 ml/min CO_2 flow rate.

SEM images of precipitates obtained from different CO_2 flow rate experiments were compared in Figure 4.54. Reaction time was decreased by increasing the CO_2 flow rates which the particles were rice-like at low CO_2 flow rates the crystals obtained at high CO_2 flow rates in aggregated smaller cubic form of about 50 nm. This may be the result of increasing CO_2-$Ca(OH)_2$ contact area. Reactive calcite crystallization occurs between gas-liquid interfaces. In this system, these interfaces were increased due to the successive CO_2 bubbles. As decreasing CO_2 flow rate, reaction time is increased and final crystals obtained were individual cubic from of about 200 nm.

It is possible to say that; low CO_2 flow rate is more suitable condition to obtain mono-disperse nano calcite particles o about 200 nm. On the other hand, smaller calcite

particles of about 50 nm can be produced at high CO_2 flow rate, but they undergo aggregation in the solution.

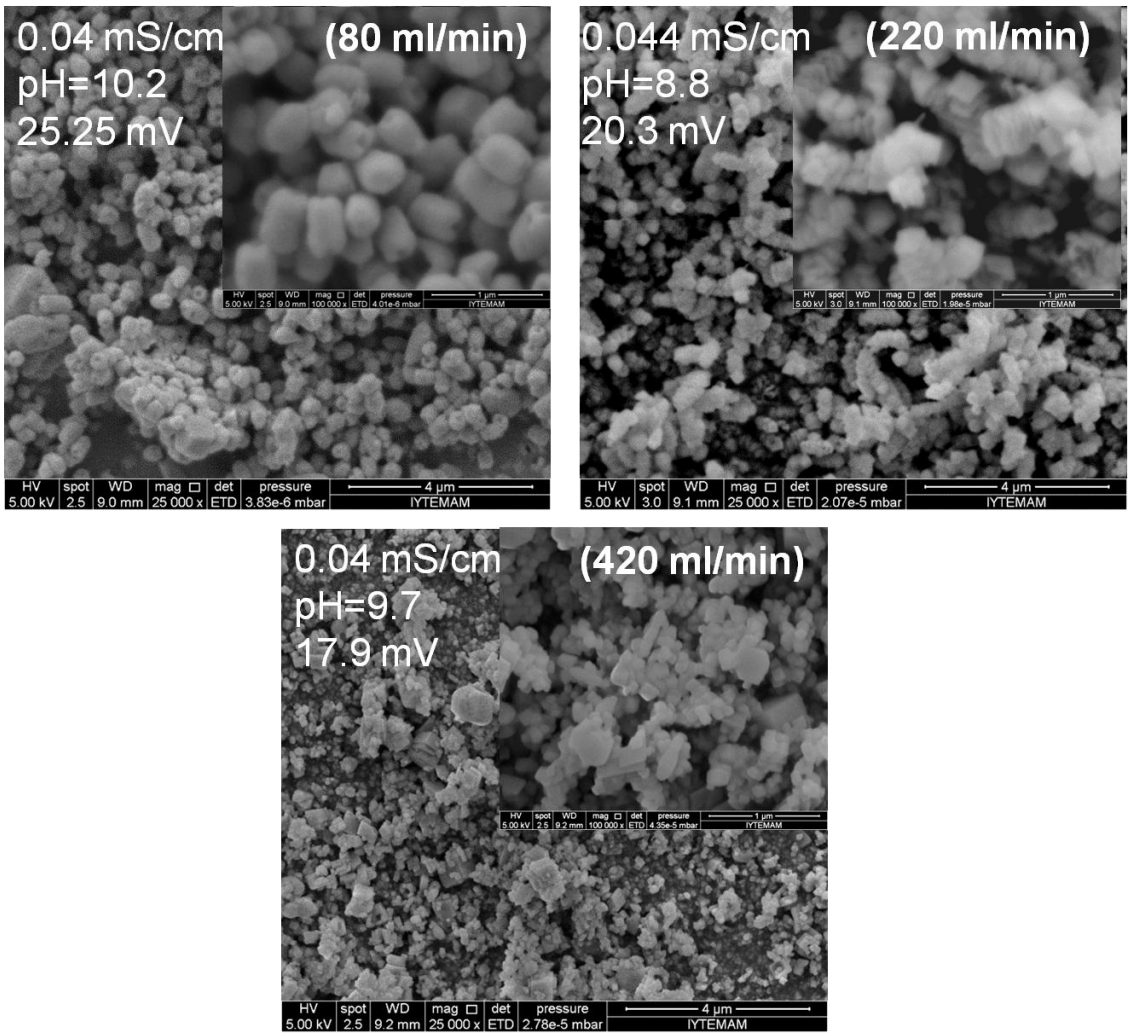

Figure 4.54. SEM images of precipitate obtained from different CO_2 flow rate (25000x and 100000x magnification).

The XRD patterns of the precipitates obtained from the different CO_2 flow rates by the helix pipe CO_2 injection were shown in Figure 4.55. According to the XRD patterns of the precipitates, the strong and sharp diffractions indicate that all samples were calcite. Also, there were no any different peaks detected. Any impurity or any different $CaCO_3$ crystalline form was not observed.

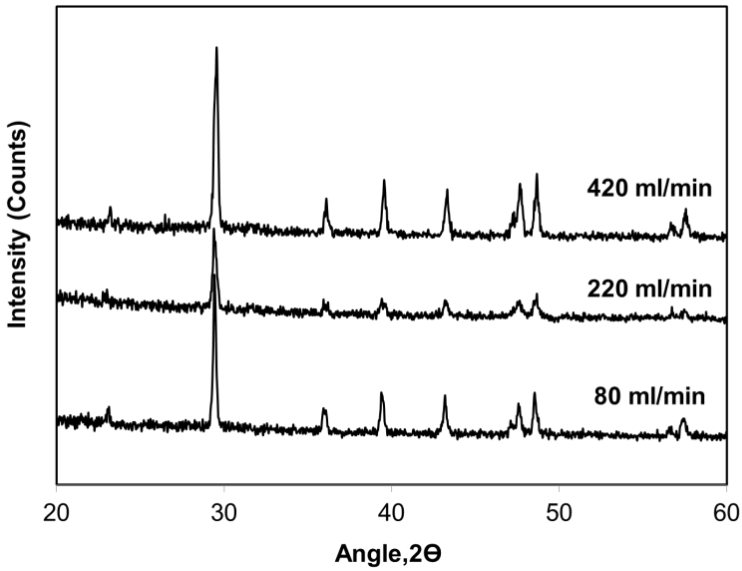

Figure 4.55. XRD patterns of precipitate obtained from different CO_2 flow rate experiments.

4.8. CO_2 Pulsation Using Helix Pipe

Like CO_2 flow rate, CO_2 injection type may also influence the $CaCO_3$ crystallization. For this study, "CO_2 pulsation" means that suddenly injecting CO_2 into the system for a period of time and then suddenly stop it following. This flash CO_2 injection would cause some changes in the system. For that reason, CO_2 was injected into the system by two different ways; one is continuous and the other is pulsation. These processes were analyzed at low and high CO_2 flow rates, respectively. The results were compared with each other in the following sections.

4.8.1. Pulsation with Low CO_2 Flow Rate

Two experiments were performed in order to investigate the CO_2 injection by pulsation into the system. CO_2 injection was performed at low CO_2 flow rate while all other conditions remain constant. Figure 4.56 shows the pH and conductivity values when CO_2 was injected into the solution by pulsation and continuous. Reaction was carried out in a longer time period when the CO_2 was injected into the system by pulsation. Conductivity was constant when the CO_2 injection was stopped during

pulsation. It again continued to decline when CO_2 was injected. In the pulsation method, it was aimed that particles would form during CO_2 injection, and they were transferred into the stabilization region when the CO_2 injection was stopped.

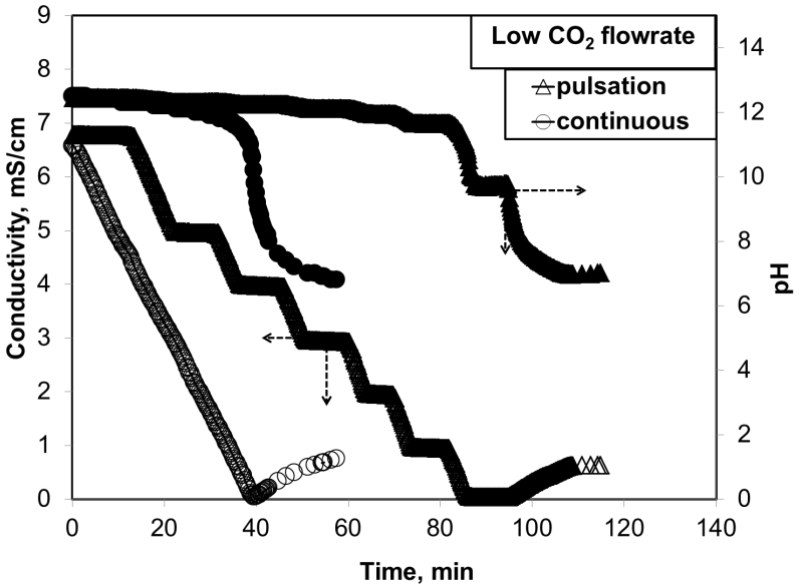

Figure 4.56. Change of conductivity and pH in different CO_2 injection way at low CO_2 flow rate.

Figure 4.57 shows the zeta potential and average particle size of solution for the different CO_2 injection procedures. As shown in the figure, the average particle sizes curves showed similar trend although pulsation method took longer time. Particles were in submicron size during crystallization. At the beginning of the reactions, particle size was nearly 250 nm. Particle sizes were started to grow rapidly at the end of the reaction. At his point zeta potential was decreased to its lowest values which resulted in the coagulation of calcite particles. The zeta potential for the continuous CO_2 injection procedure, an increase was observed about +50 mV at the beginning of the crystallization. At this period, the primary small calcite particles may be nucleated and dispersed in the solution. Then, a decrease in zeta potential was seen to below the +30 mV at the final stages of the crystallization. In CO_2 pulsation procedure, the zeta potential was about +30 mV during crystallization and it was decreased to about +20 mV at the stage of crystallization. While the average particle size were below 350 nm during crystallization a sudden jump were seen to the late stages of crystallization.

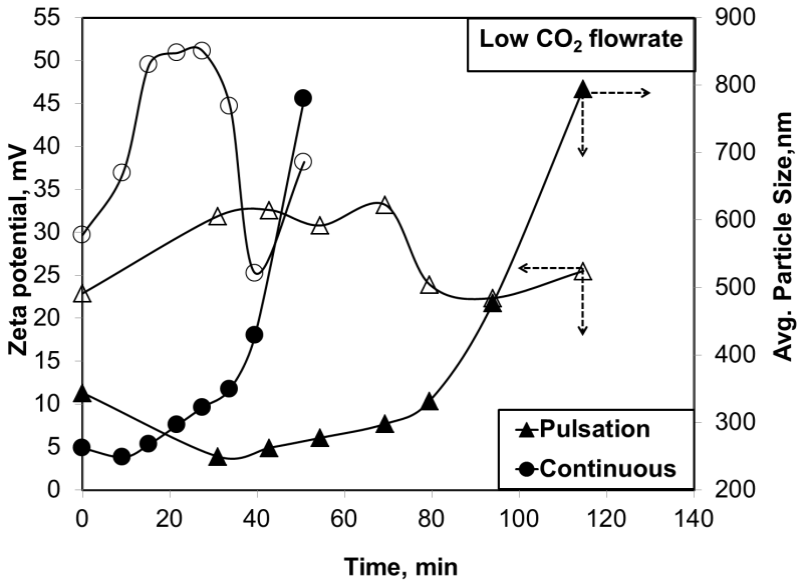

Figure 4.57. Change of zeta potential and average particle size in different CO_2 injection way at low CO_2 flow rate.

The SEM images were shown for the two procedures when the CO_2 injection was conducted close to surface of the bubble reactor with a helix pipe. SEM images of precipitate calcite particles, which were obtained by continuous CO_2 injection, were shown in Figure 4.58. Before the CO_2 injection, at stage (0), there was a mixture of small and large $Ca(OH)_2$ particles. As soon as CO_2 was injected into the solution at stage (1), spindle-like $CaCO_3$ particles were obtained in solution. These particles were in smaller sizes. The very large particles which are shown in stage (3) may be an impurity in $Ca(OH)_2$ powder. Some small $CaCO_3$ particles formed at stages (4) and (5). When the reaction was completed at stage (6), small cubic particles were obtained, some of which formed hollow shaped particles. Finally, some decomposition was observed in cubic forms into spindle-like shape again due to the reverse reaction at pH nearly 7 at stage (7).

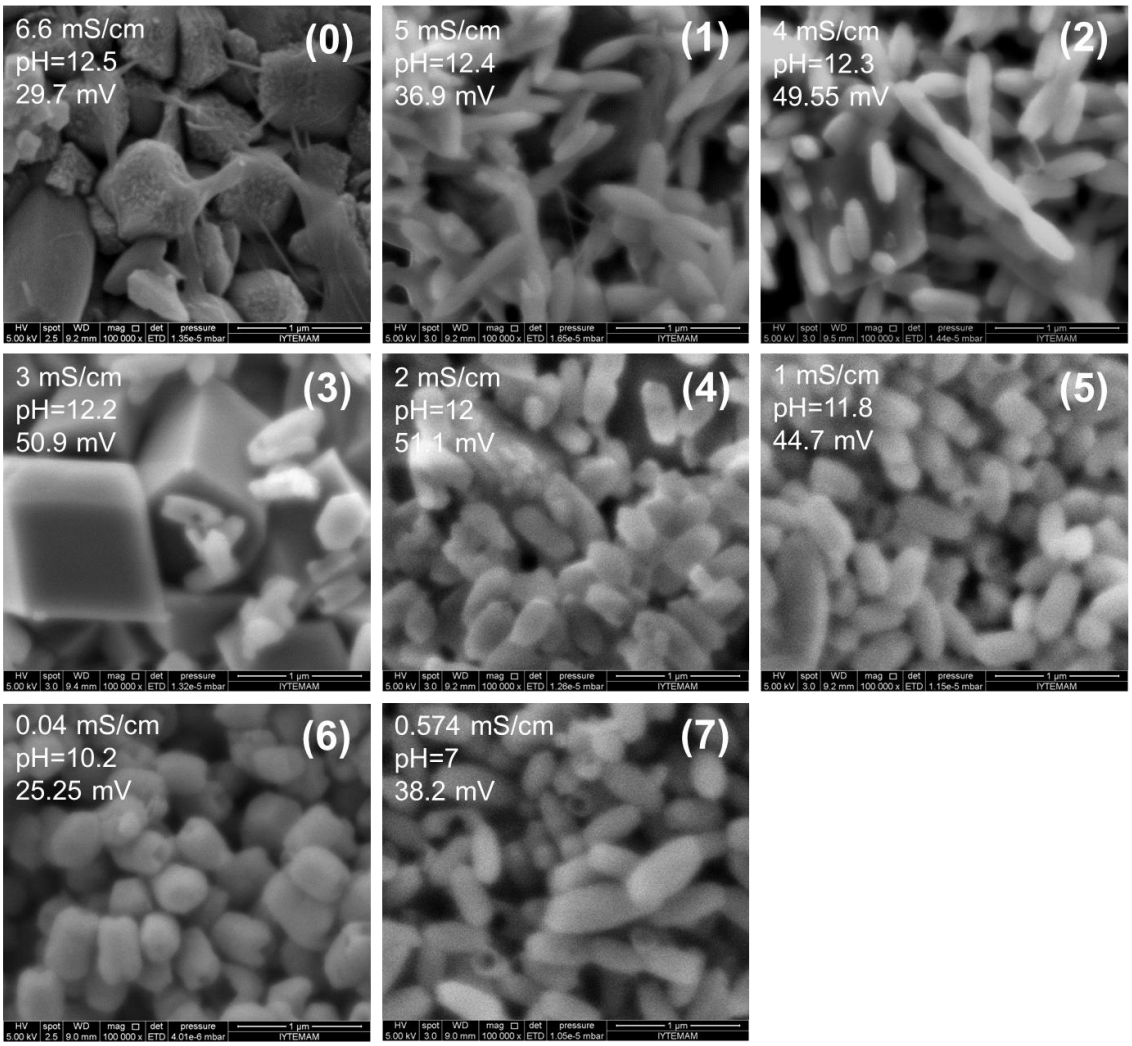

Figure 4.58. SEM images of precipitate according to advancement of reaction obtained by continuous CO_2 injection at low CO_2 flow rate.

SEM images of precipitated calcite particles, which were obtained by CO_2 pulsation method, were shown in Figure 4.59. Before the CO_2 injection, at stage (0), there was a mixture of small and large particles. As soon as CO_2 was injected into the solution at stages (1) and (2), spindle-like $CaCO_3$ particles were obtained solution. And, these particles were smaller in size and formed into cubic particles at stage (3). Individual, small cubic $CaCO_3$ particles were synthesized in solution at stages (4) and (5). When the reaction was completed at stage (6), these small cubic particles were obtained with some hollow cubic particles as crystallization progressed time. Finally, some decomposition was observed in cubic forms into spindle-like shapes again with a dissolution and recrystallization mechanism at pH nearly 7 at stage (7).

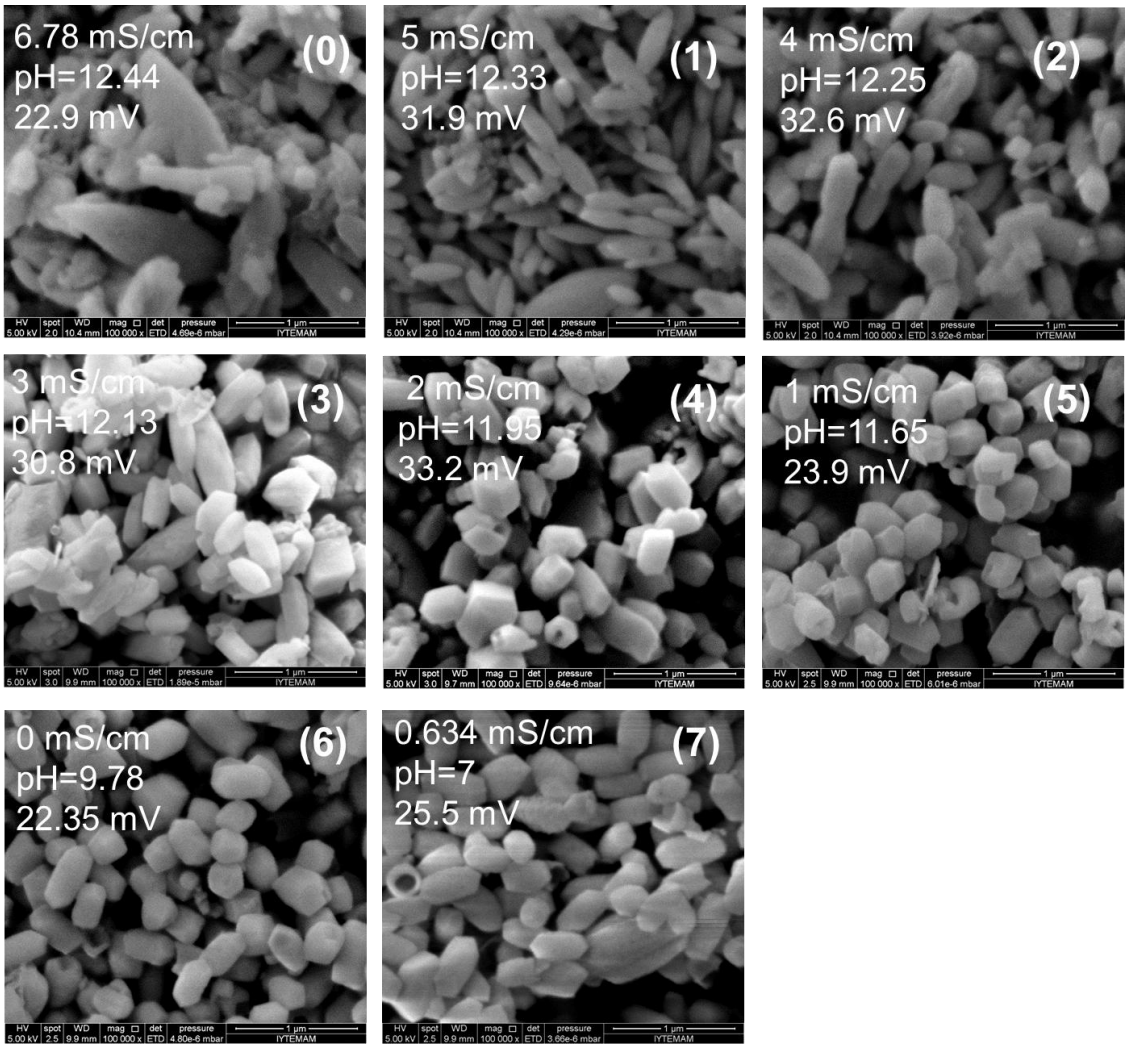

Figure 4.59. SEM images of precipitate according to advancement of reaction obtained by pulse CO_2 injection at low CO_2 flow rate.

A comparison of SEM images of particles obtained from the two procedures given in Figure 4.60. As shown in the SEM images, individual, almost cubic mono-dispersed particles were produced from different CO_2 injection methods at low CO_2 flow rates. Smaller and homogeneously distributed particles were observed from CO_2 injection by pulsation method. Therefore, mono dispersed nano particles could be produced by the pulsation method without much coagulation.

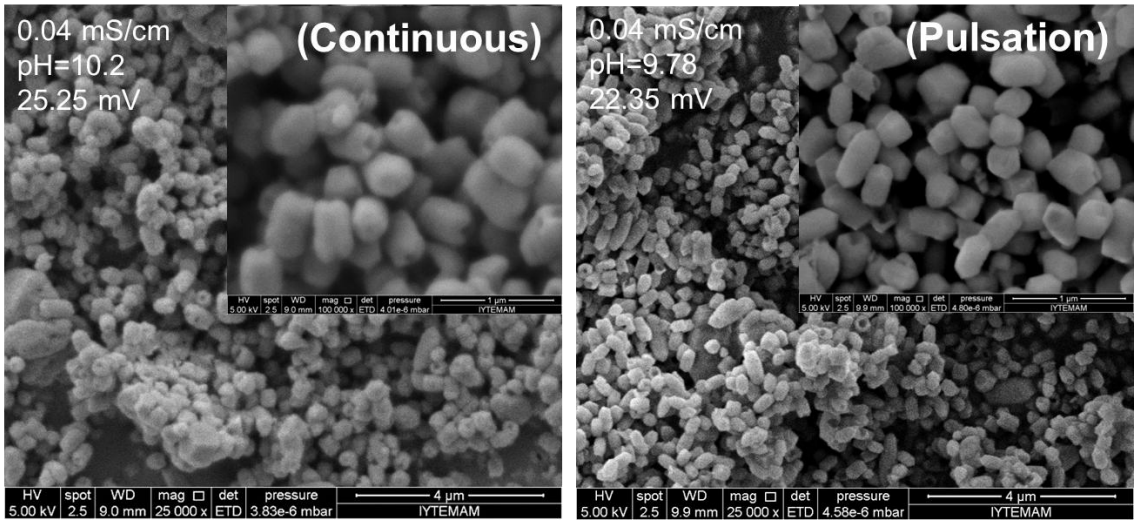

Figure 4.60. SEM images of precipitate obtained from different CO_2 injection way at low CO_2 flow rate (25000x and 100000x magnification).

The XRD patterns of the precipitates obtained from different CO_2 injection methods at low CO_2 flow rate was shown in Figure 4.61. According to the XRD patterns of the precipitates, all samples were calcite.

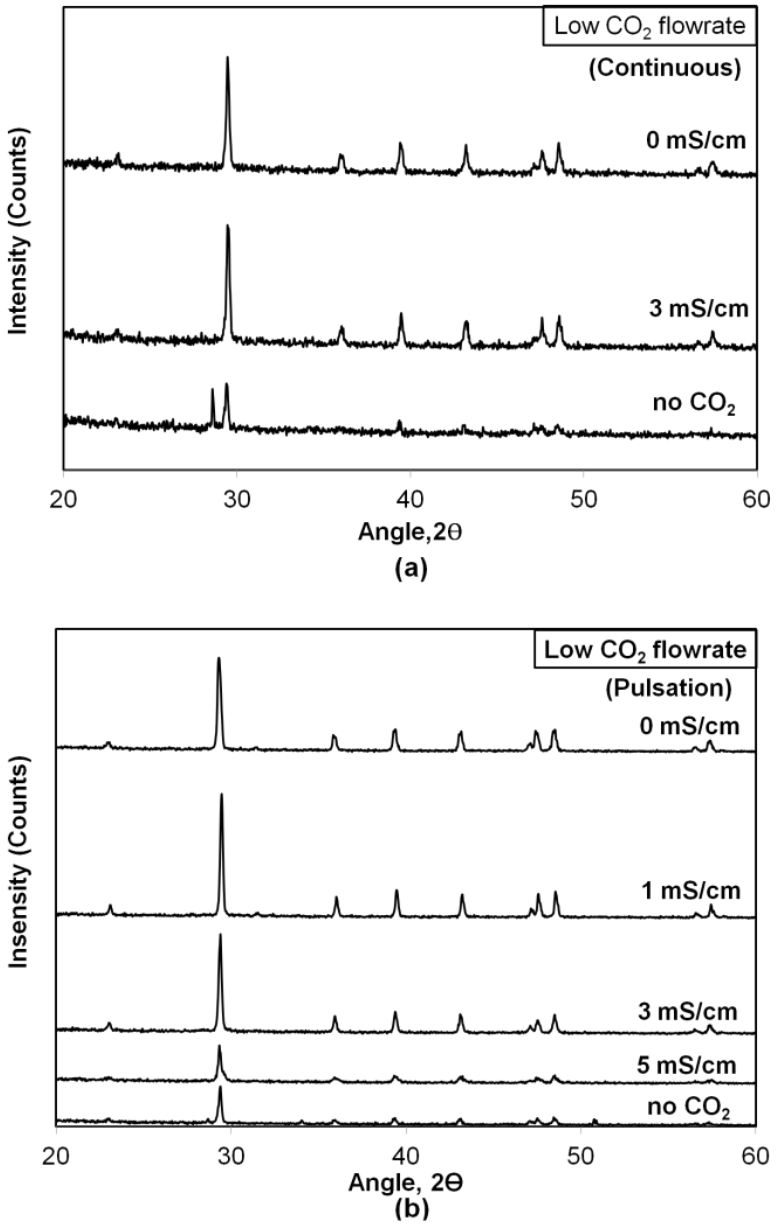

Figure 4.61. XRD patterns of precipitate obtained from different CO_2 injection way (a) continuous (b) Pulsation.

4.8.2. Pulsation with High CO_2 Flow Rates

Pulsation method was tested at high CO_2 injection rate. Figure 4.62 shows the pH and conductivity values in solutions when CO_2 was injected in the solution with either; pulsation and continuous methods. Crystallization took longer time with the pulsation method while it was highly shorter for the continuous CO_2 injection.

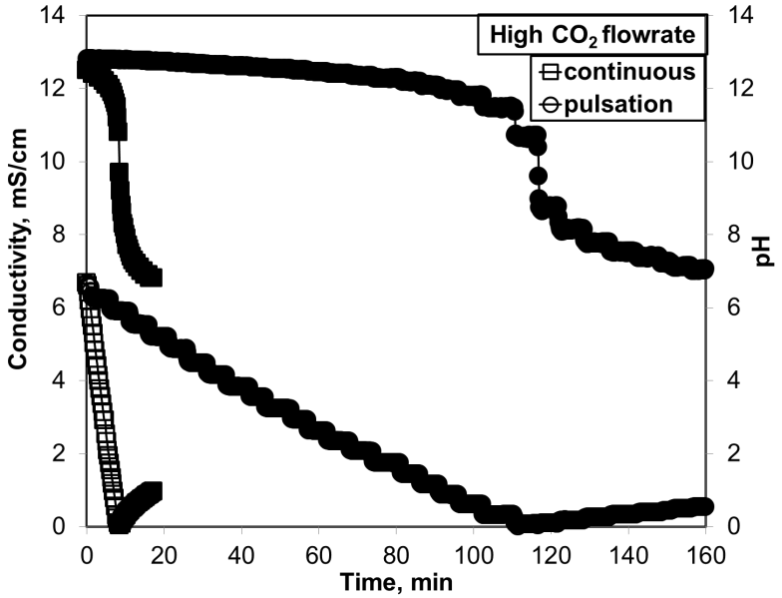

Figure 4.62. Change of conductivity and pH of solution in different CO_2 injection method at high CO_2 flow rates.

Figure 4.63 shows zeta potential and average particle size of solution in different CO_2 injection methods at high CO_2 flow rates. As shown in the figure, average particle size was submicron for the pulsation. On the other hand, the particle sizes were all larger than 3 μm in continuous CO_2 injection method. The increase in the particle size could be due to coagulation of particles. Also pulse CO_2 injection is more suitable way to reach nano calcite at high CO_2 flow rate when the CO_2 flow rate was higher.

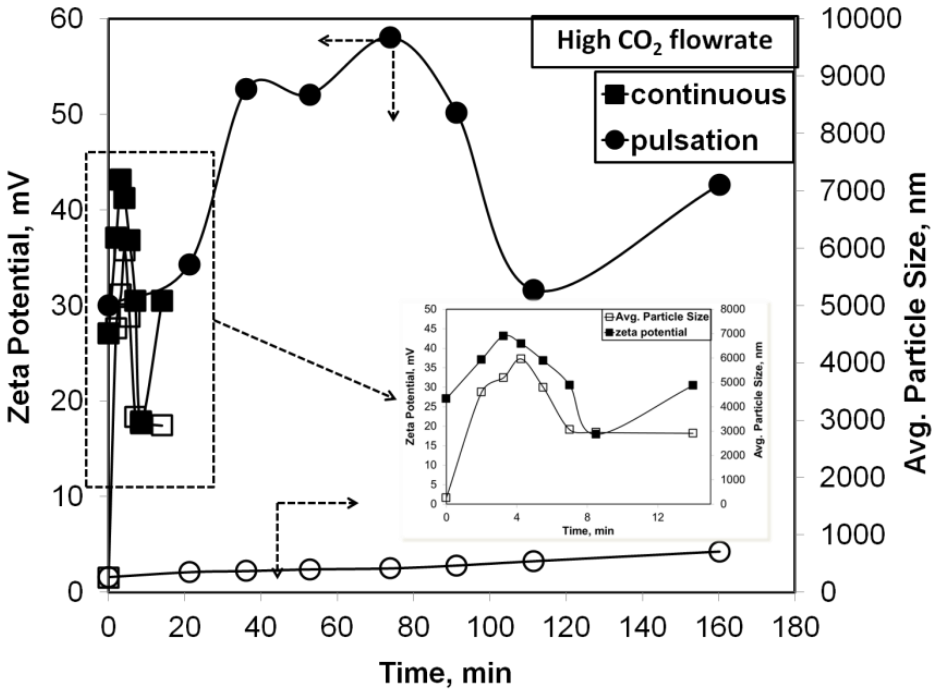

Figure 4.63. Change of zeta potential and average particle size in different CO_2 injection method at low CO_2 flow rate.

Figure 4.64 shows the SEM images of precipitated calcite particles, which were obtained by continuous CO_2 injection at high CO_2 flow rate. Before the CO_2 injection, at stage (0), there was a mixture of small and large particles. As soon as CO_2 was injected into the solution, very small $CaCO_3$ particles were obtained in solution. And these small particles attached together and formed into aggregated particles during crystallization. The aggregation was consistent throughout the crystallization. The aggregation is probably a result of high CO_2 flow rate. High CO_2 caused a rapid crystallization reaction and produced aggregated of $CaCO_3$ particles.

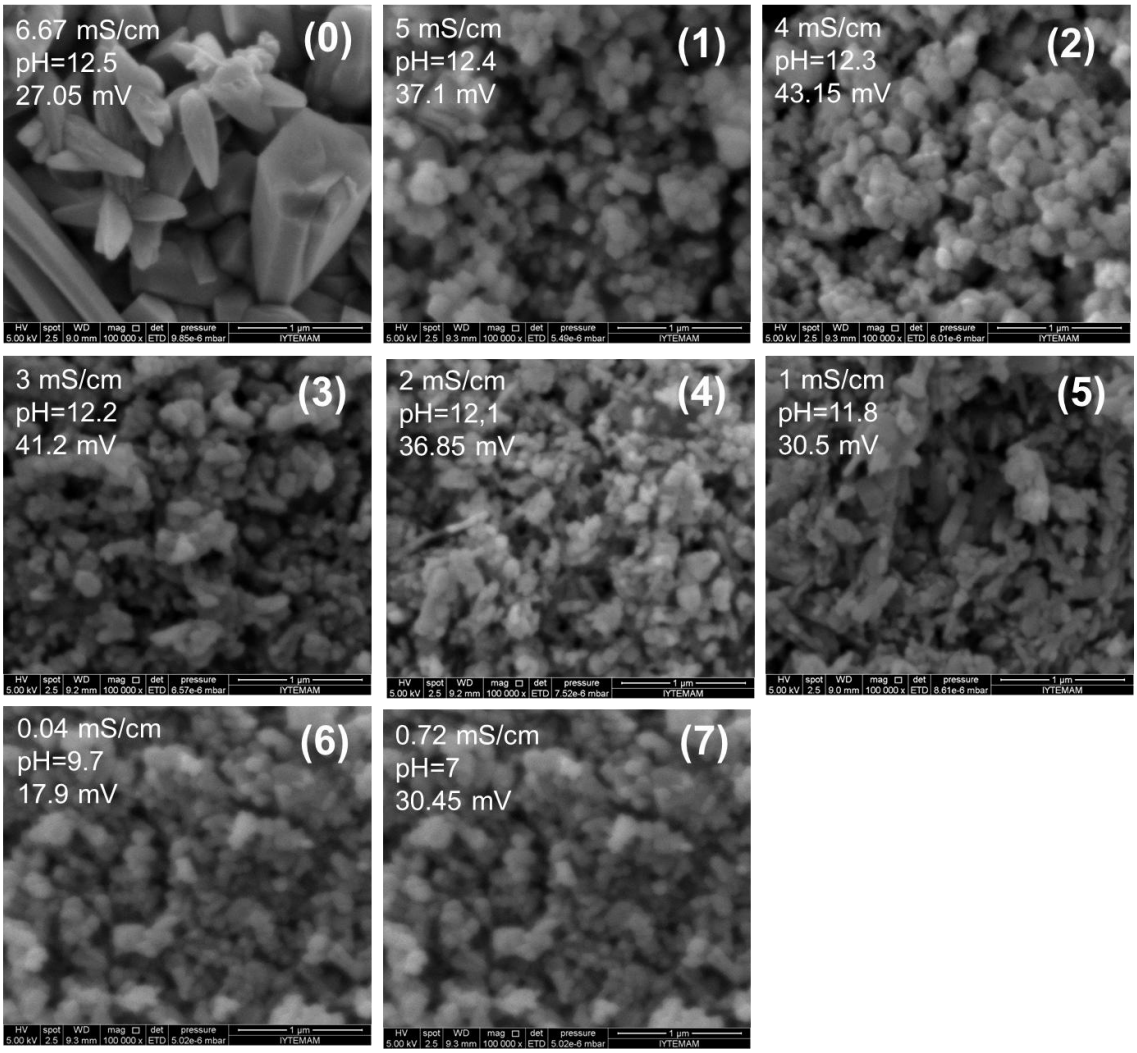

Figure 4.64. SEM images of precipitate according to advancement of reaction obtained by continuous CO_2 injection at high CO_2 flow rate.

Figure 4.65 shows the SEM images of precipitated calcite particles, which were obtained by pulse CO_2 injection method at high CO_2 flow rates. Before the CO_2 injection at stage (0), there was a mixture of large particles due probably to the impurities. As soon as CO_2 was injected into the solution, very small spindle-like $CaCO_3$ particles were produced at stages (1), (2) and (3). These particles dispersed at stages (4) and (5). When the reaction was completed at stage (6), these particles were observed in mostly individual particles. Finally, there was no significant change in particle morphology at pH value nearly 7 at stage (7).

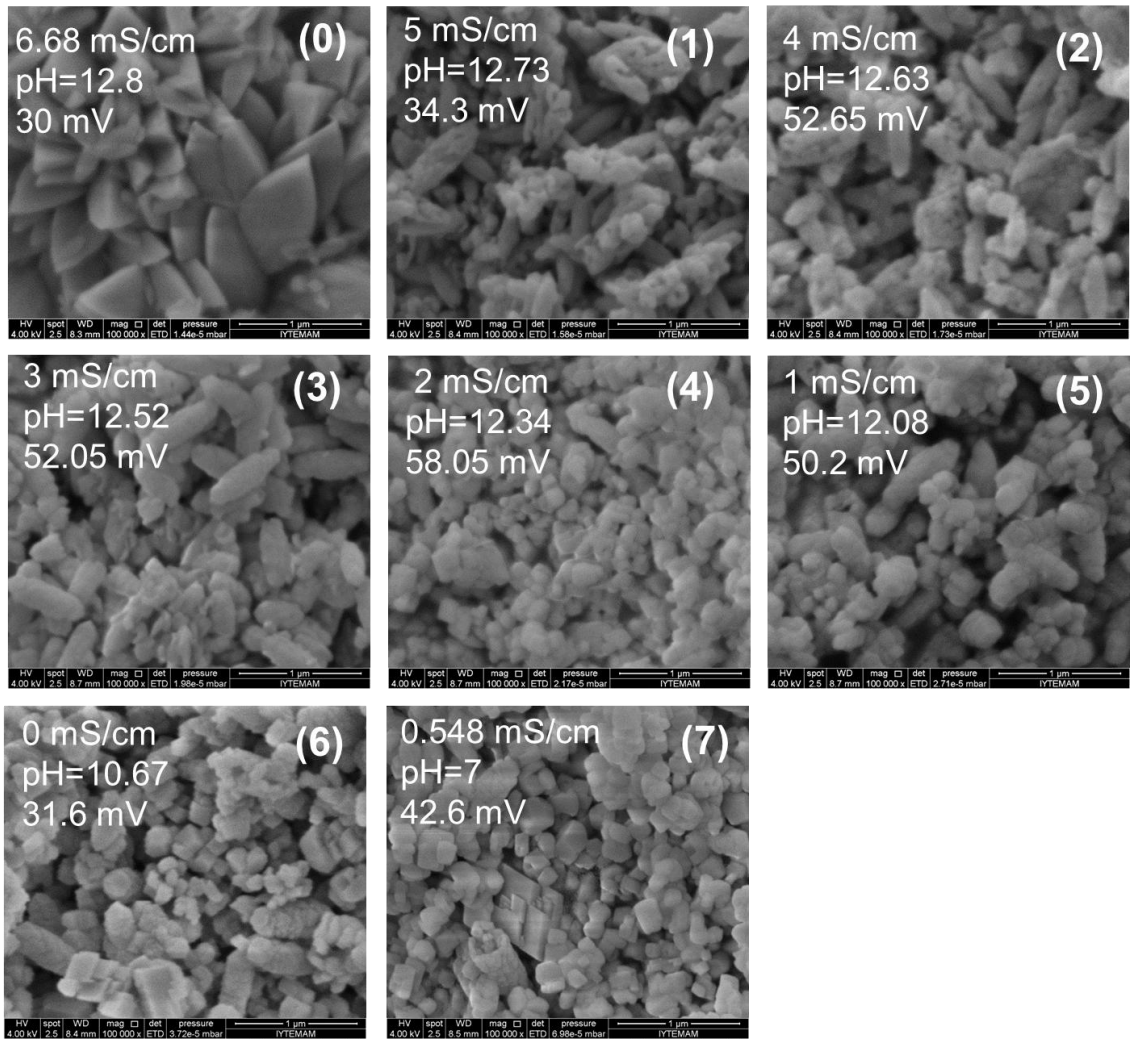

Figure 4.65. SEM images of precipitate according to advancement of reaction obtained by pulse CO_2 injection at high CO_2 flow rate.

Figure 4.66 compares the SEM images obtained during the pulsation method and continuous method at high CO_2 flow rates. According to SEM images, aggregated and small $CaCO_3$ particles were produced from different CO_2 injection methods at high CO_2 flow rates. Smaller and more individual particles were observed from CO_2 injection by pulsation. Particles were more dispersed in pulsation method than those obtained from continuous method.

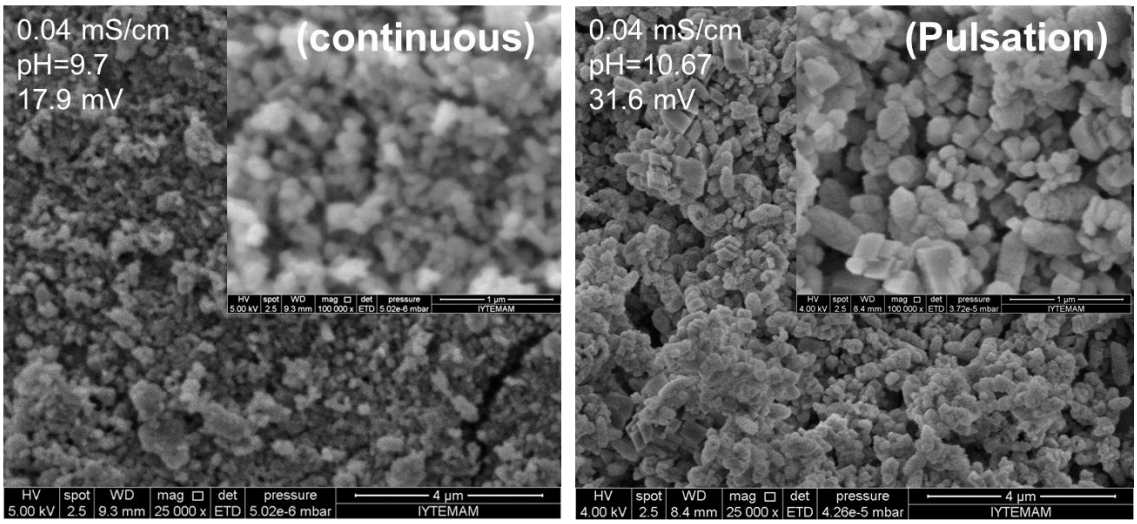

Figure 4.66. SEM images of precipitate obtained from different CO_2 injection way at high CO_2 flow rate (25000x and 100000x magnification).

4.9. Effect of $Ca(OH)_2$ Concentration on $CaCO_3$ Production with Pulsation

Effects of $Ca(OH)_2$ concentration on the $CaCO_3$ production were studied by pulsation method when CO_2 was injected into the solution by certain intervals and stopped for another time duration. Because the solubility of $Ca(OH)_2$ is about 25 mM at room temperature, the effect of low concentrations, below the solubility limit and high concentration, above the solubility limit, were studied. Concentration above the solubility limit will produced dissolved $Ca(OH)_2$ powders, which made the solution to be a slurry. Conductivity and pH values were given in Figure 4.67. As shown in figure, the conductivity of solution was started at 2.2 mS/cm, 6.68 mS/cm, 9.48 mS/cm and 9.56 mS/cm for 5 mM, 15 mM, 30 mM and 50 mM of $Ca(OH)_2$, respectively. The crystallization time was different for different concentration. Different pulsation and waiting periods for each concentration were applied differently for each experiment as shown in Table 3.1. For 15 mM $Ca(OH)_2$, precipitation time was very long due to the high waiting period (5 min) during pulsation. The pulsation figures could also affect the crystallization time.

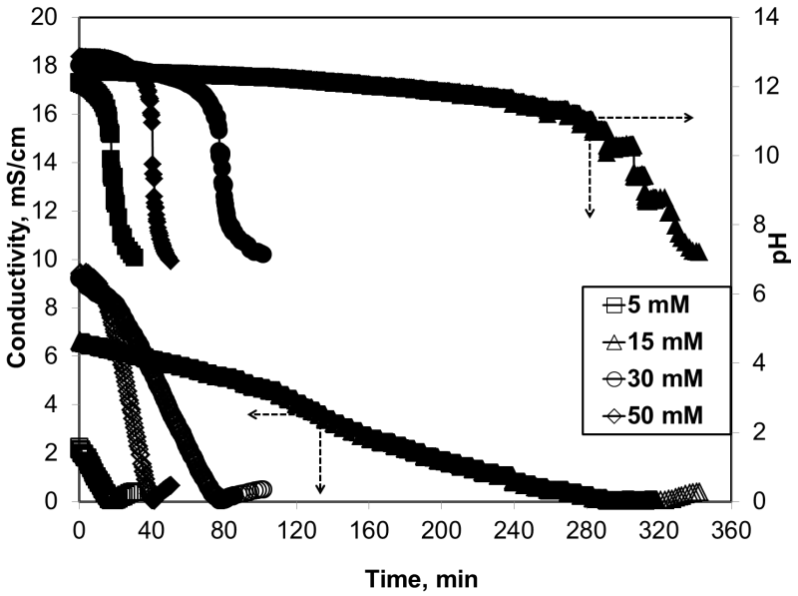

Figure 4.67. Change of pH and conductivity in the presence of low and high amounts of $Ca(OH)_2$ on the precipitation of CO_2. (Stirring rate: 750 rpm, CO_2 flow rate 420 ml/min).

Figure 4.68a-b shows the zeta potential and average particle size of particles obtained in the presence of low and high amounts of $Ca(OH)_2$. The zeta potential measurements showed a similar trend for each concentration. A sudden increased in conductivity was seen at the initial step of crystallization and a slight decrease were seen at the late stage of crystallization. The average particle size were seen to be higher for low concentration and higher concentrations of $Ca(OH)_2$ comparing to particle sizes obtained at 15 mM, which is close to the solubility limit. The $CaCO_3$ particles which a particle size larger than 1 μm were obtained from 5 mM and 30 mM of $Ca(OH)_2$. Submicron particles were obtained for 15 mM of $Ca(OH)_2$.

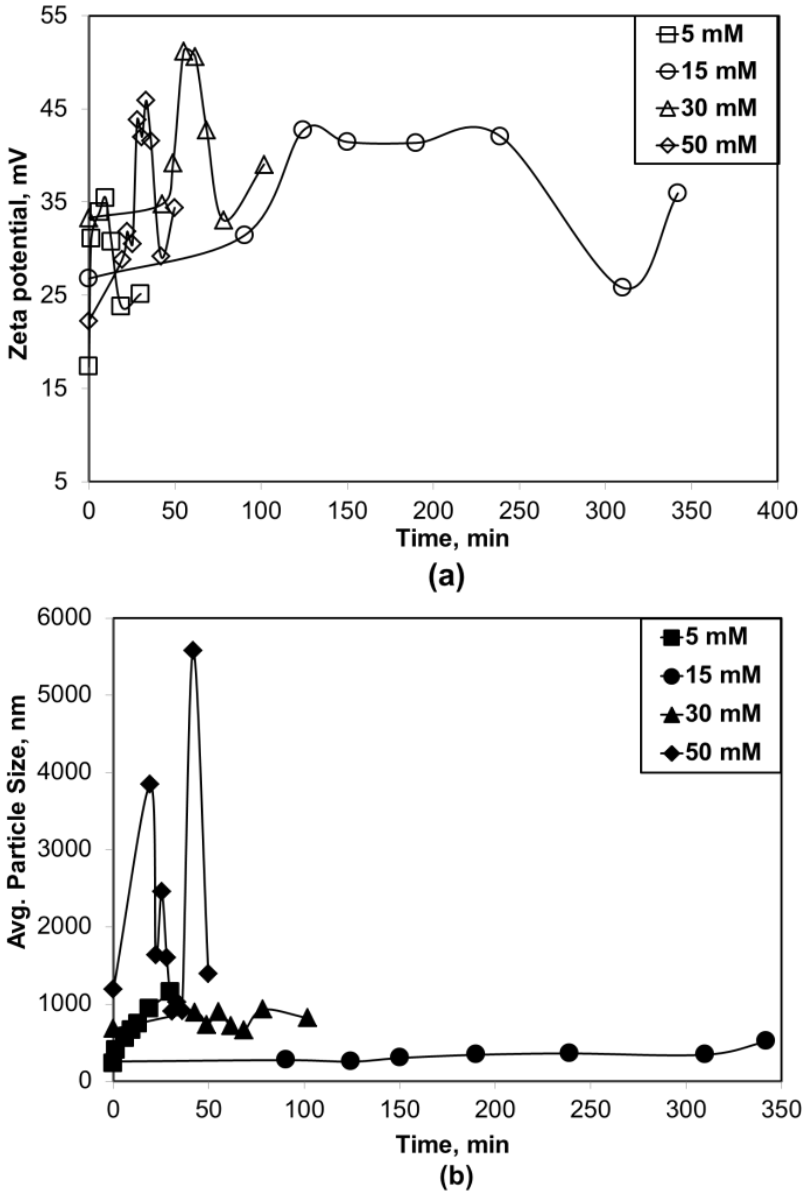

Figure 4.68. Change of (a) Zeta potential and (b) Average particle size of experiments in the presence of low and high amounts of $Ca(OH)_2$ on the precipitation of CO_2.

Figure 4.69 shows the SEM images of precipitate $CaCO_3$ particles, which were obtained from 5 mM of $Ca(OH)_2$. Before the CO_2 injection, at stage (0), there are small and large particles which were probably come from impurities. As soon as the CO_2 was injected into the solution, large cubic $CaCO_3$ particles (~500 nm) were produced at stages (1) and (2). Then, these particles converted into larger and individual cubic calcite particles at stages (3) and (4). When the reaction was completed at stage (6), individual calcite cubes were obtained. Finally, cubic calcite particles were formed and

also some defects were on the calcite surfaces as a result of decreasing pH nearly 7 at stage (7).

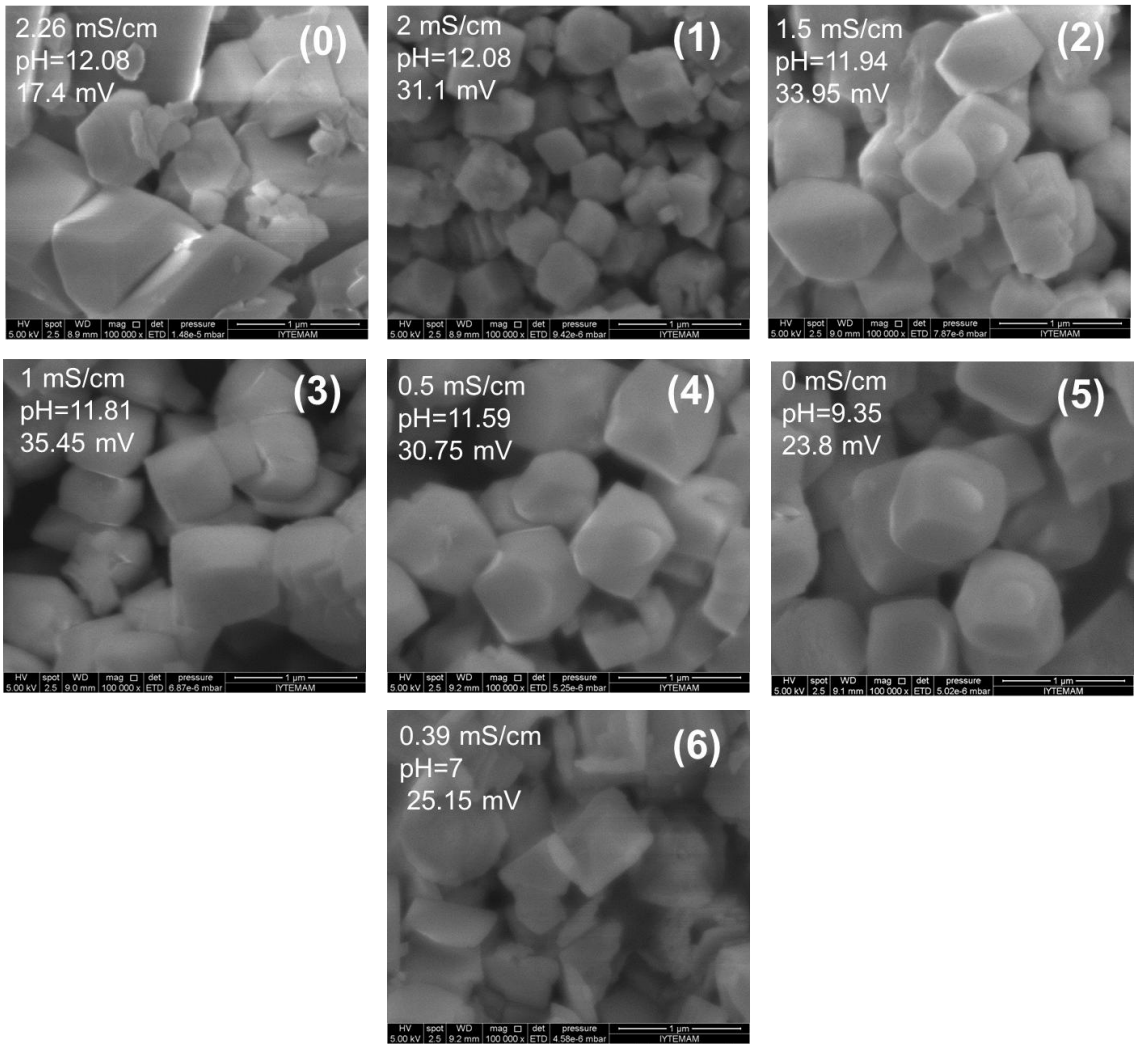

Figure 4.69. SEM images of precipitate according to advancement of reaction from 5 mM of $Ca(OH)_2$.

Figure 4.70 shows the SEM images of precipitated calcite particles, which were obtained from 15 mM of $Ca(OH)_2$. Before the CO_2 injection at stage (0), there were some particles obtained by centrifugation which were probably newly synthesized particles or inert particles from the $Ca(OH)_2$ purchased. As soon as the CO_2 was injected into the solution, spindle-like $CaCO_3$ particles were observed at stages (1) and (2). These particles were formed in a rice-like shape at stages (3), (4) and (5). At these stages, spindle-like particles were also converted into hollow and rectangular prism shapes during crystallization. This could be caused to dissolving of particles and

appearing some defects on the more energetic regions of the crystal. When the reaction was completed at stage (6), more individual crystal particles were formed in solution. At pH nearly 7, some defects have occurred on the crystal surfaces at stage (7).

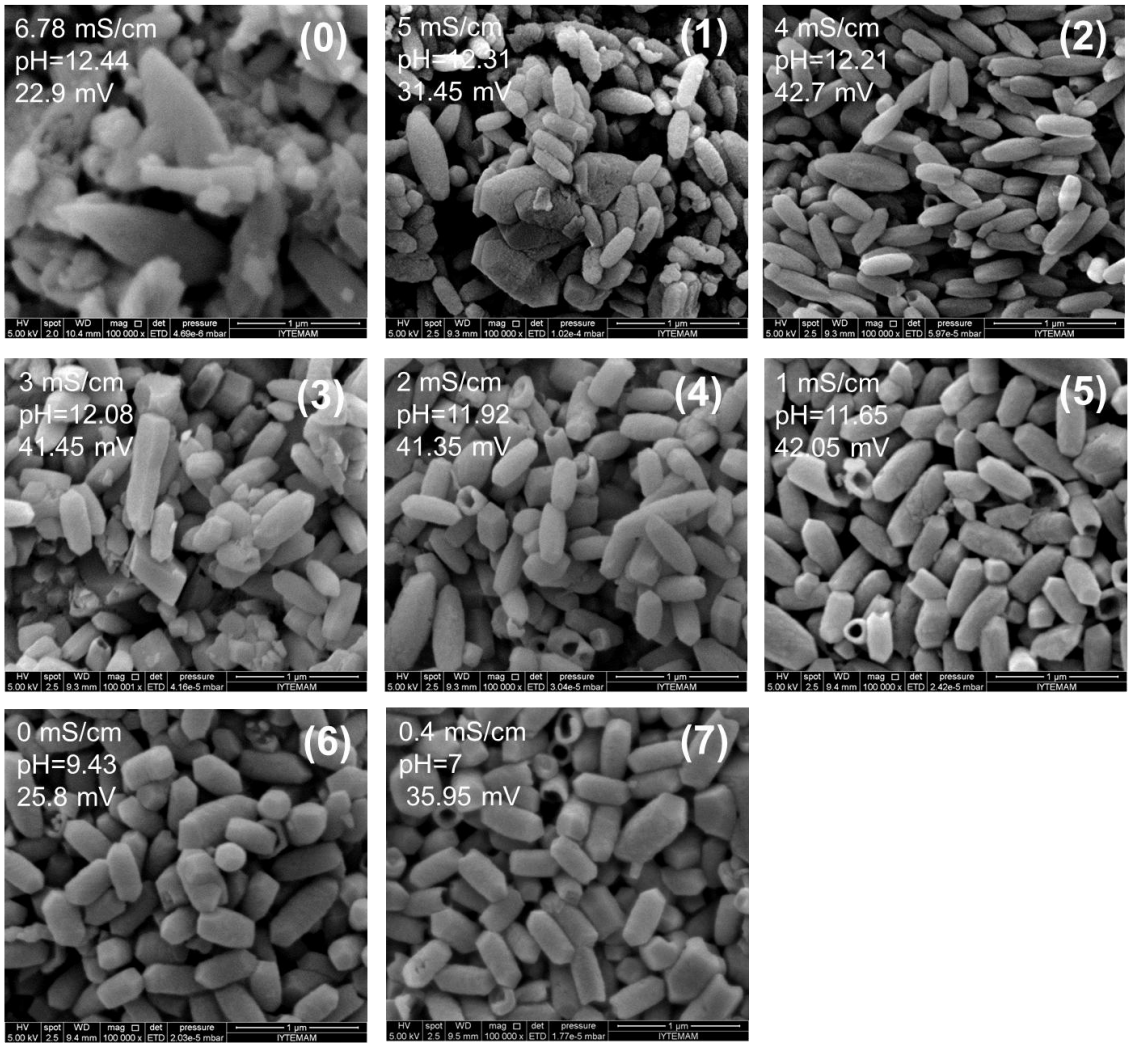

Figure 4.70. SEM images of precipitate according to advancement of reaction from 15 mM of $Ca(OH)_2$.

Figure 4.71 shows the SEM images of precipitated calcite particles, which were obtained from 30 mM of $Ca(OH)_2$. Before the CO_2 injection at stage (0), there were some newly formed small spindle-like particles. These particles could be formed in solution due to the intrusion of CO_2 into the $Ca(OH)_2$ solution and they may come from some impurities. As soon as the CO_2 was injected into the solution, spindle-like $CaCO_3$ particles were observed at stages (1), (2) and (3). These particles were converted into the cubic crystal form as conductivity and pH were both decreasing at stages (4), (5) and

(6). At these stages, spindle-like particles were obtained also due to the high $Ca(OH)_2$ concentration in solution. Such particle formation may also be observed due to non-dissolved $Ca(OH)_2$ particles. As a result, non-homogeneous particles were produced. When the reaction was completed at stage (6), beside spindle-like particles, cubic crystals were formed in solution. When pH was nearly 7, larger and submicron particles were observed at stage (7).

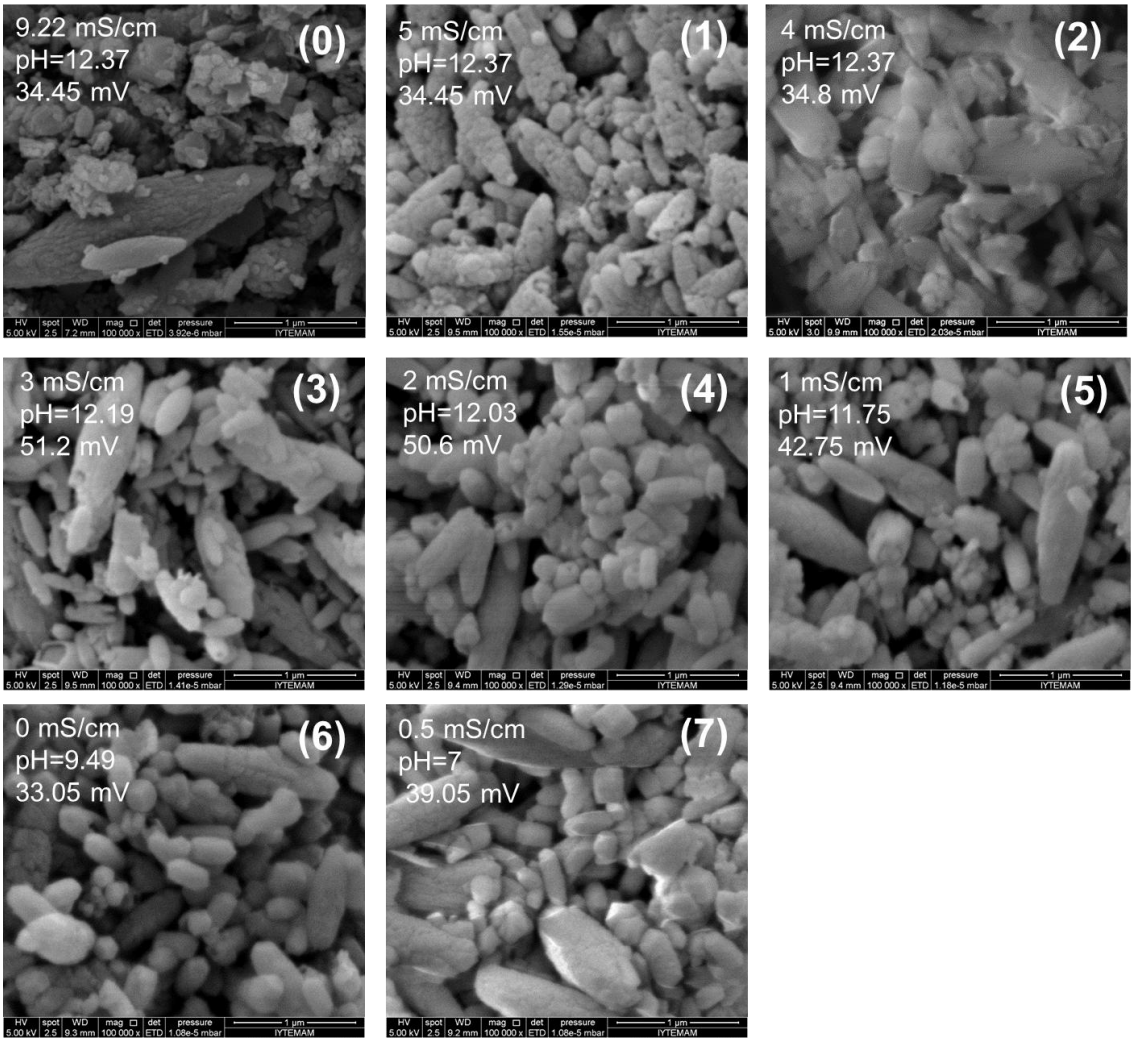

Figure 4.71. SEM images of precipitate according to advancement of reaction from 30 mM of $Ca(OH)_2$.

Figure 4.72 shows the SEM images of the precipitated calcite particles which were obtained from 50 mM of $Ca(OH)_2$. Before the CO_2 injection, at stage (0), there are large and small particles. These particles were seen to form on the non-dissolved $Ca(OH)_2$ particles and on some impurities such as $CaCO_3$. As soon as the CO_2 was

injected into the solution, spindle-like $CaCO_3$ particles were obtained at stages (1), (2) and (3). These particles were formed aggregates at stages (4), (5) and (6). At these stages, spindle-like particles were also observed due to the high $Ca(OH)_2$ concentration in solution. When the reaction was completed at stage (7), aggregated cubic crystals in submicron sizes were formed in solution. These particles were seen to be highly obtained aggregated. After this stage at pH nearly 7, smaller cubic particles were obtained due to the dissolution of particles at stage (7).

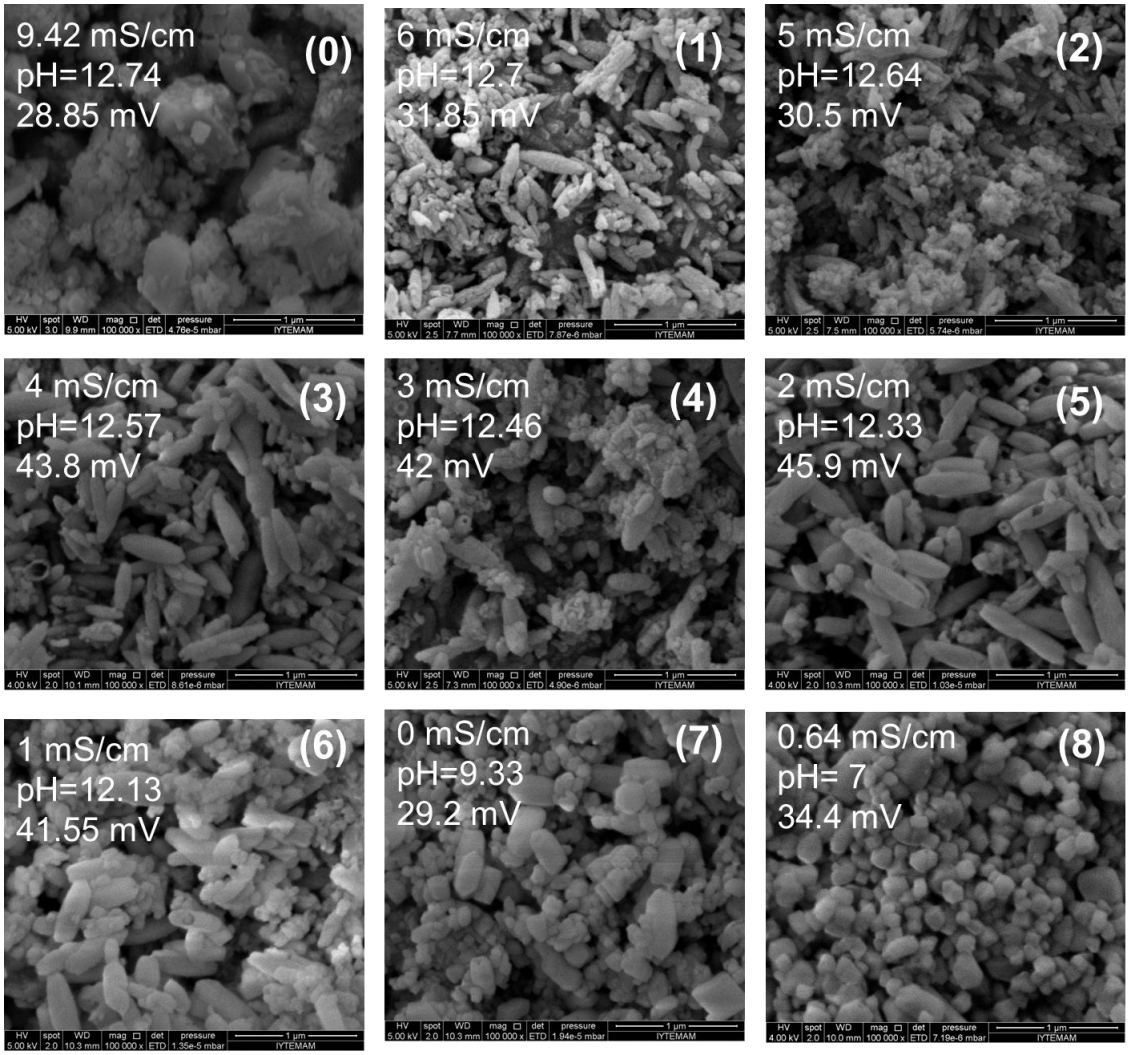

Figure 4.72. SEM images of precipitate according to advancement of reaction from 50 mM of $Ca(OH)_2$.

The SEM images of the precipitates which were obtained by pulsation method in the presence of low and high amounts of $Ca(OH)_2$ was compared in Figure 4.73. According to the SEM images, individual, mono-dispersed and nano-cubic particles

were obtained from 5 mM and 15 mM $Ca(OH)_2$. More aggregated and large spindle particles with heterogeneous size distribution were obtained from 30 mM and 50 mM $Ca(OH)_2$. These results showed that there was a strong effect of $Ca(OH)_2$ amount on the $CaCO_3$ precipitation. To obtain nano calcite particles, $Ca(OH)_2$ amount in solution must be near the solubility limit.

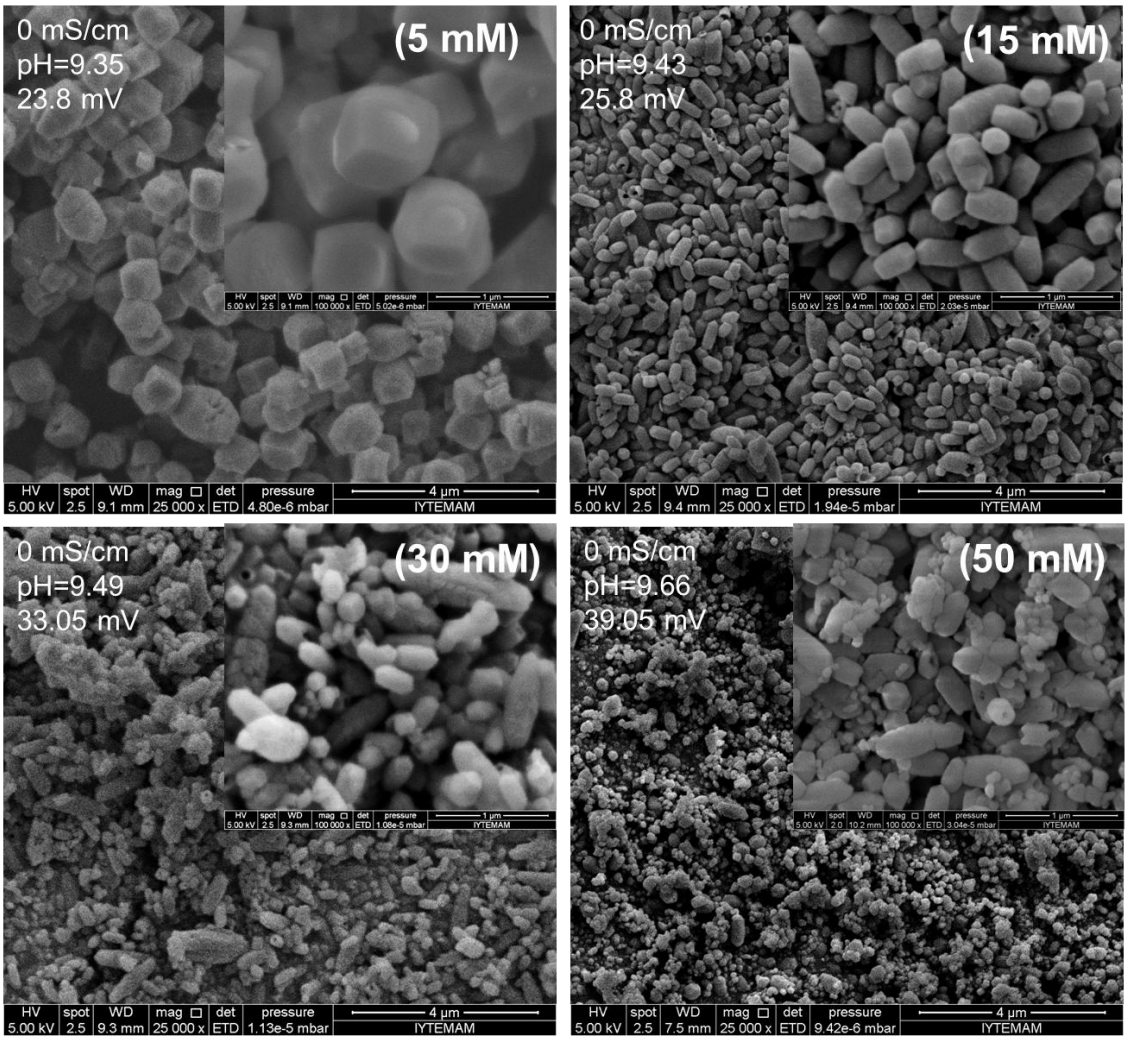

Figure 4.73. Effect of low and high amounts of $Ca(OH)_2$ on the shape and size of the precipitated $CaCO_3$.

Figure 4.74 shows the average particle size with $Ca(OH)_2$ concentration. As shown in the figure, the average particle size is a u-shape with $Ca(OH)_2$ concentration. Solubility limit of $Ca(OH)_2$ must be used to obtain particles in nano sizes in the carbonization method. The smallest particles seemed to be obtained at near the solubility limit of $Ca(OH)_2$. However, the particles could be obtained even much smaller at higher $Ca(OH)_2$ concentration as shown from Figure 4.73, but they are

highly aggregated. The particles produced the near solubility limit are in submicron sizes and highly homogeneous.

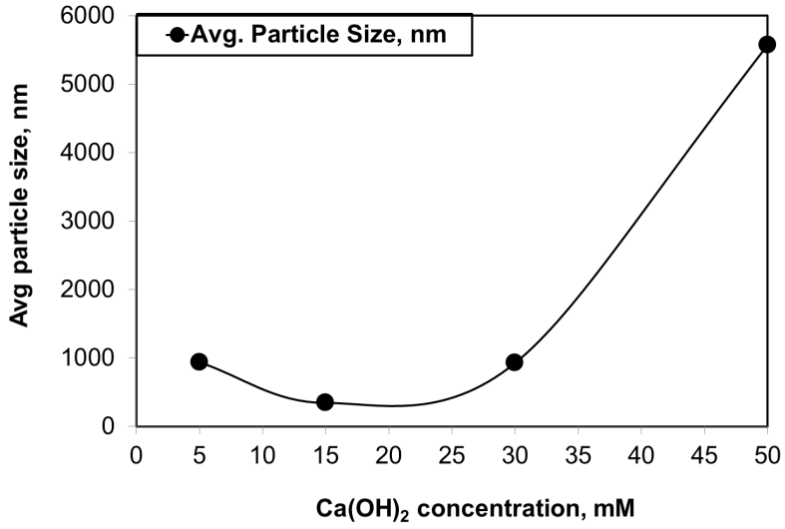

Figure 4.74. The average particle size change according to $Ca(OH)_2$ concentration.

The XRD patterns of the precipitates obtained from different $Ca(OH)_2$ concentration were shown in Figure 4.75. According to XRD patterns of the precipitates, the strong and sharp diffractions indicate that all samples were well characterized calcite particles. Also, there was no any different peak detected. Any impurity or any different $CaCO_3$ crystalline form was not detected.

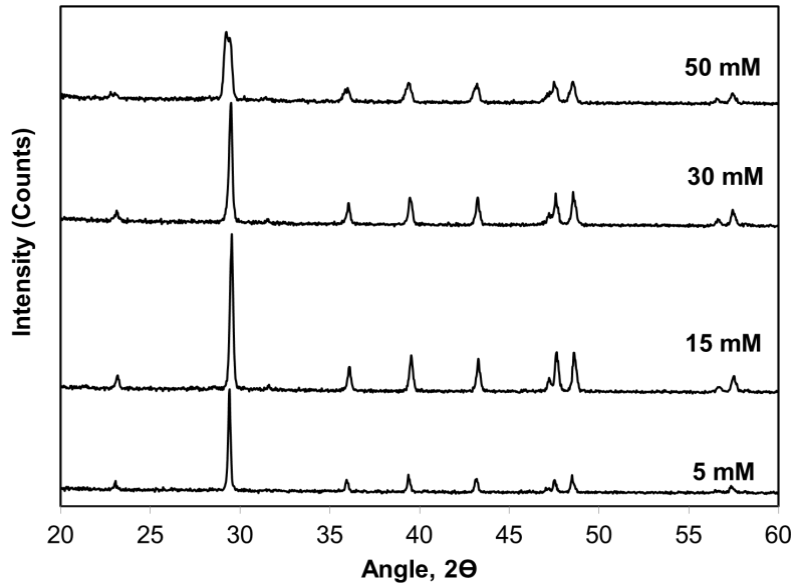

Figure 4.75. The XRD patterns of precipitated $CaCO_3$ from low to high amounts of $Ca(OH)_2$.

4.10. Effect of Jet Flow on $CaCO_3$ Crystallization in $Ca(OH)_2$ Slurry

"Jet flow" means providing a $Ca(OH)_2$ flow onto the CO_2 bubbles released from a helix pipe at high flow rate in a 12 L of $Ca(OH)_2$ solution. This new set-up was applied to prevent particles from aggregation at the crystallization size. Conductivity and pH values were shown in Figure 4.76. The experiment was completed faster due to the dispersion of CO_2 bubbles in the reactor.

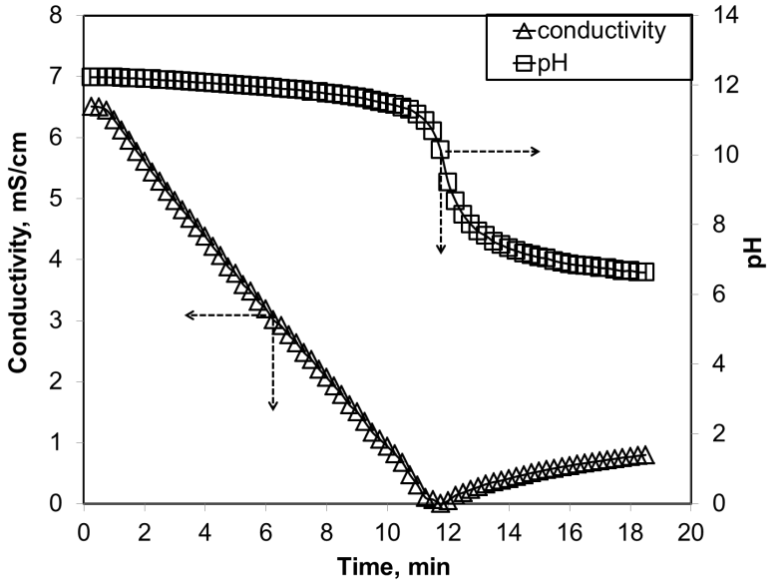

Figure 4.76. pH and conductivity change in presence of jet flow in the system

Figure 4.77 shows the zeta potential and average particle size of particles in the presence of jet flow in the system. As shown in the figure, the average particle size was in a submicron range during the crystallization varied from 200 to 400 nm. This was a positive result. This means that the nano size particles could be produced at high CO_2 flow rate by jet flow in a newly designed set-up. An increase in zeta potential was observed nearly +32 mV at the beginning of the reaction. At this period, the primary small calcite particles may be nucleated and dispersed in the solution. Then, a decrease in zeta potential was monitored below the +30 mV at the late stage of crystallization. At this period, small particles may come together and aggregated increasing the particle size. At the final stage of crystallization, the zeta potential was increased back to at +30 mV again.

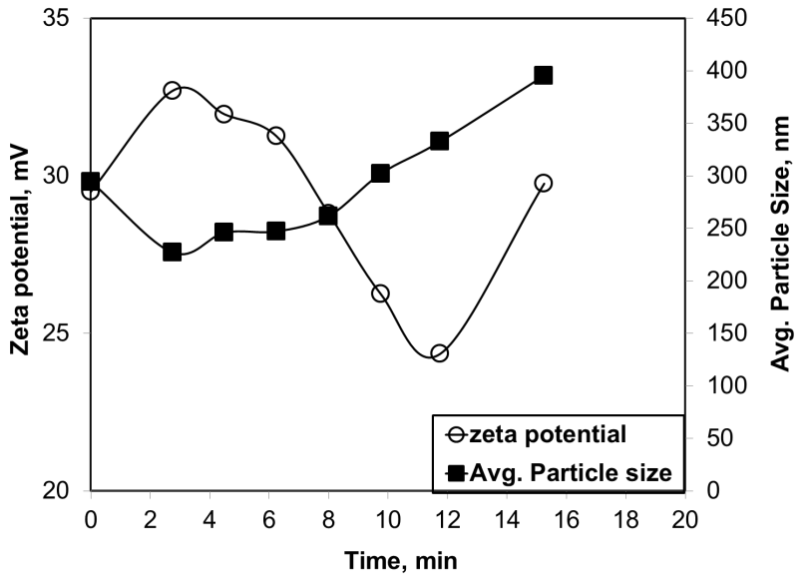

Figure 4.77. Change of zeta potential and average particle size of solution in presence jet flow in the system.

The SEM images of the precipitated calcite particles, which were produced in the presence of jet flow in the bubble reactor, were shown in Figure 4.78. Before the CO_2 injection at stage (0), there were newly produced small and large particles and already presence of impurities. As soon as the CO_2 was injected into the solution at stages (1) and (2), spindle-like $CaCO_3$ particles were formed. These particles were smaller in size and formed into rice-like particles at stage (3). Cubic $CaCO_3$ particles, hollow particles were also observed in solution at stages (4) and (5). When the reaction was completed at stage (6), individual, hollow calcite particles were obtained. Finally, aggregated particles with almost homogeneous size distribution were obtained at pH value of nearly 7 at stage (7).

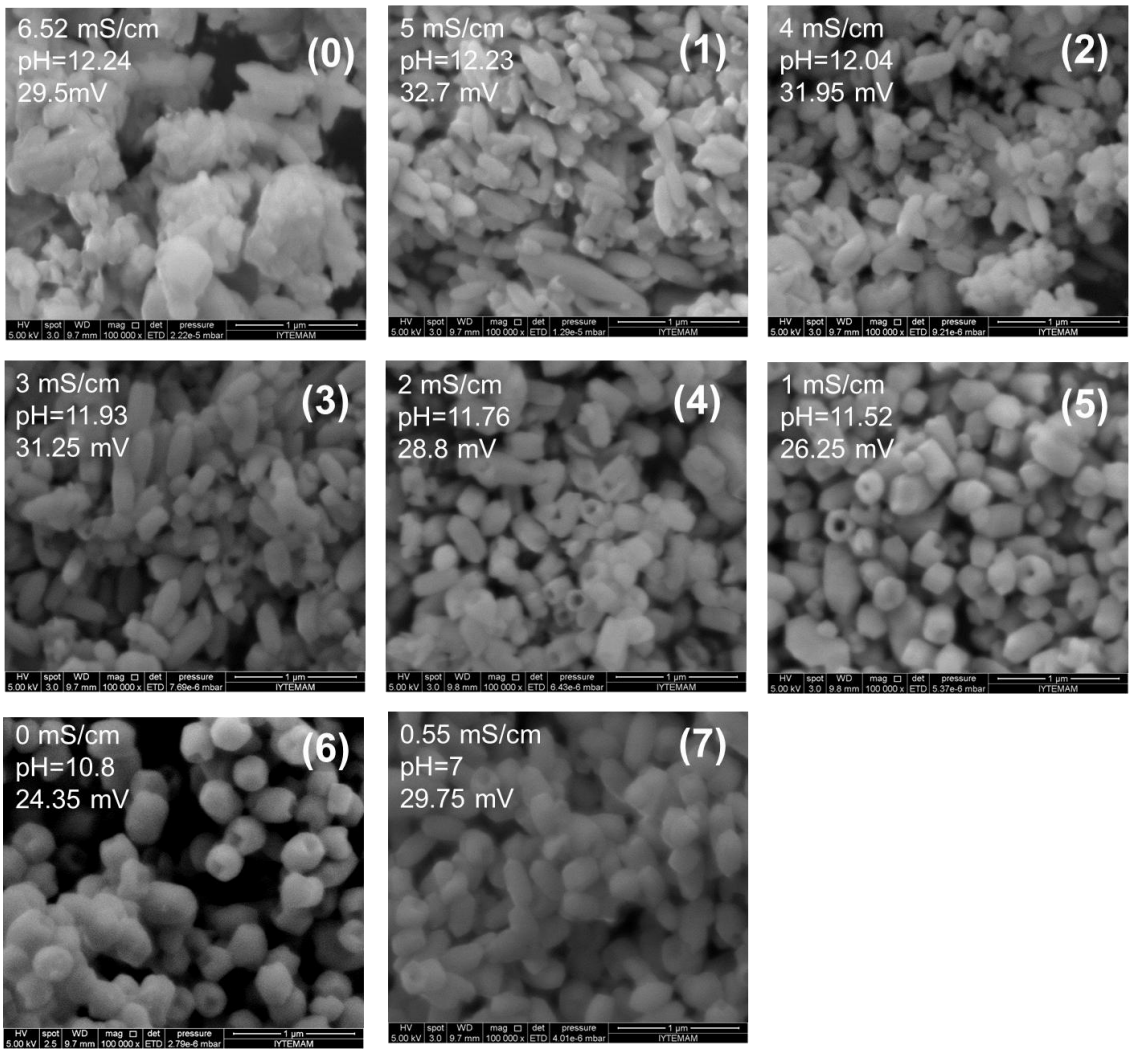

Figure 4.78. SEM images of particles according to advancement of reaction which was produced in presence jet flow in the system.

The SEM image of the precipitates obtained by the jet flow was shown in Figure 4.79. According to SEM images, individual, mono-dispersed and nano particles at approximately 200 nm were obtained from the newly developed bubble reactor. Aggregation of particles was little at high CO_2 flow rate and the size of particles were at below 200 nm.

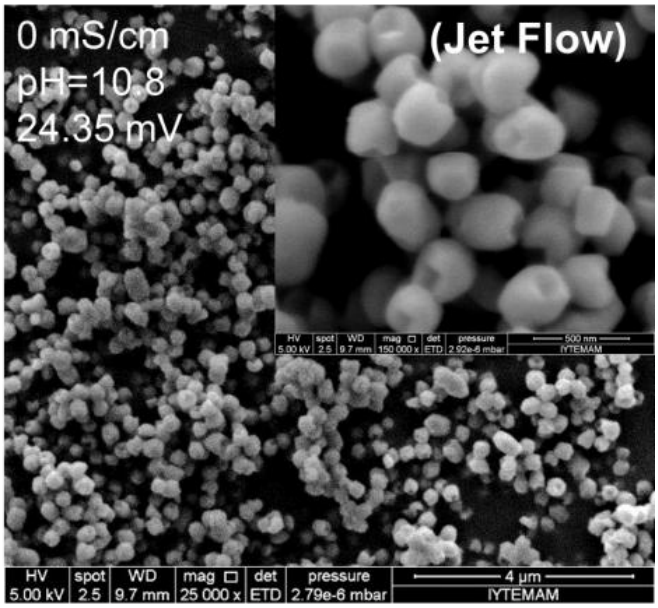

Figure 4.79. SEM images of particles which were produced in presence jet flow in the system.

The XRD patterns of the precipitates obtained from jet flow were shown in Figure 4.80. According to XRD patterns of precipitates, the strong and sharp diffractions indicate that all samples were well characterized calcite particles. Also, there was no any different peak detected. Any impurity or any different $CaCO_3$ crystalline forms were not detected.

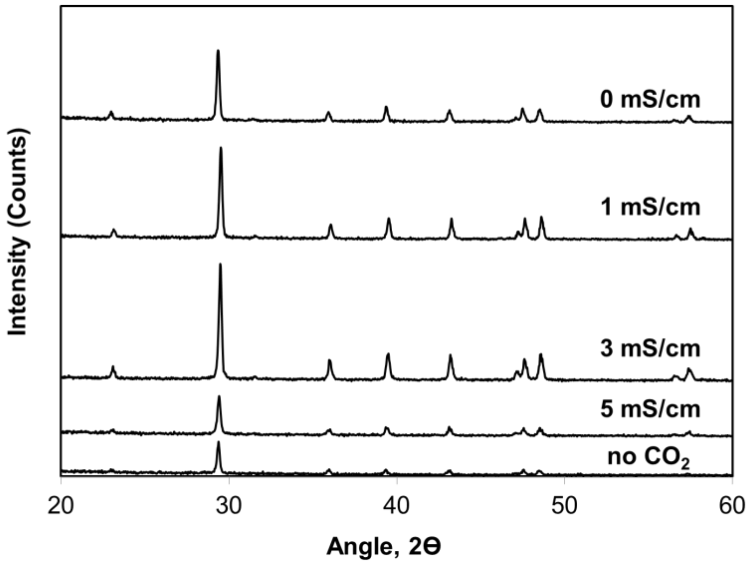

Figure 4.80. The XRD patterns of precipitated $CaCO_3$ in presence jet flow in the system.

4.11. Proposed Mechanism of the CaCO3 Crystal Production

The CO_2 injection method and CO_2 flow rate were found to be the most effective parameters for $CaCO_3$ formation for the carbonation process. Based on SEM the images of all precipitates and the findings in the literature, particles in different morphologies and different sizes can be produced by changing the CO_2 injection method and CO_2 flow rate. In fact, the production mechanism of $CaCO_3$ is highly depend on the contact area between the CO_2 gas and the $Ca(OH)_2$ solution. The injection of high CO_2 flow rate at the bottom of the reactor produced large number of bubbles in solution. The fast diffusion and dissolution of CO_2 caused the increase in the conversion of $Ca(OH)_2$ into $CaCO_3$ clusters which yielded an aggregation among particles. On the contrary, the injection of low CO_2 flow rate at the bottom of the reactor caused small number of bubbles in solution. The slow diffusion and reaction yielded low conversion of $Ca(OH)_2$ into the $CaCO_3$ clusters producing stabilized mono-dispersed rice-like particles The contact area and the contact time between CO_2 and $Ca(OH)_2$ adjusted to reach an optimal condition to obtain the nano calcite particles.

As soon as the CO_2 was injected into the solution, the crystallization reaction suddenly starts and amorphous $CaCO_3$ clusters were formed due to the ionic counterparts in the solution at the beginning of crystallization. Then, crystals were obtained as conductivity decreased almost linearly and pH slightly decreased to 10 or 9.

At this point, the morphology of the particles was orientated into a chain-like calcite form. Dispersed crystal structures were detected due to the resolution of particles with decreasing pH at nearly 7. According to contact area and contact time between gas and liquid two main forms are detected in particles morphology: chain like and cubic rhombohedral.

Figure 4.81 shows the rhombohedral nano calcite formation mechanism during crystallization. As shown in the SEM images, before the CO_2 injection at stage (0), there were large and small particles detected in small amounts as impurities. As the CO_2 was injected at stage (1) spindle-like $CaCO_3$ particles were formed in solution. The two ends were shown to be more energetic so that particles were grown faster through the edges that were happened through the sides. As crystallization progressed, the highly energetic ends started to dissolve and hollow particles were produced at stage (2). Then, the particles were transformed into almost cubic hallow particles as more dissolution occurred at stage (3). When the reaction was completed, at stage (4), the hollow particles were filled by dissolution and recrystallization mechanisms. Therefore, almost mono-dispersed nano calcite particles were achieved to produce in the semi-batch bubble reactor.

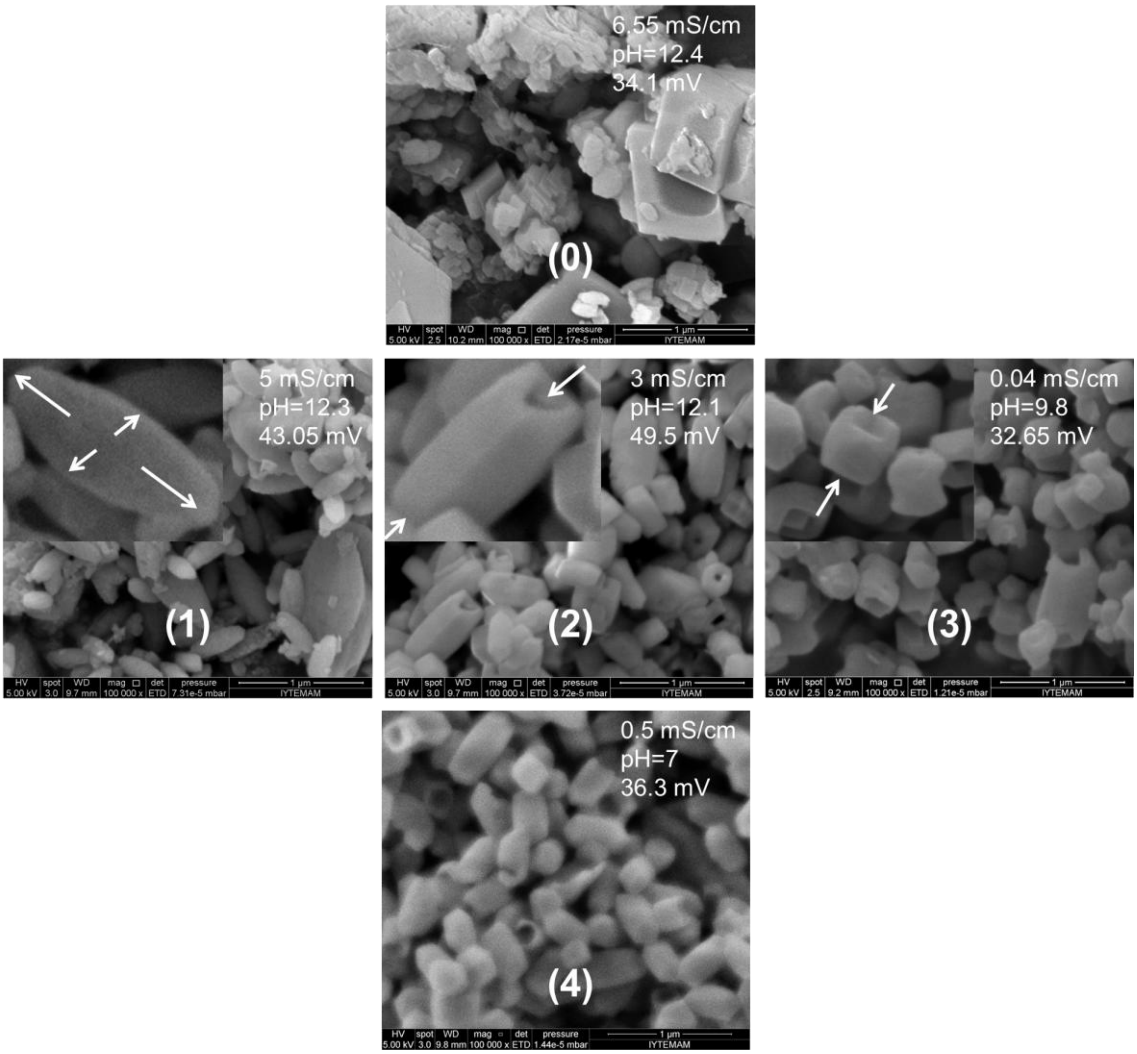

Figure 4.81. Rhombohedral cubic nano calcite formation mechanism according to advancement of reaction.

CHAPTER 5

CONCLUSIONS

Although nano $CaCO_3$ production methods and formation mechanisms have been still studied in the literature, a proven method has not been suggested to produce nano calcite in homogeneous size distribution and different morphologies. In this study, nano $CaCO_3$ particles were produced by carbonization method in different conditions in a newly designed semi batch bubble reactor. Also, mechanisms were proposed for nano calcite formation. Among the other polymorphs, stable calcite was the main product of $Ca(OH)_2$-H_2O-CO_2 crystallization. These crystals were produced in different sizes and morphologies by the semi batch bubble reactor. The size and morphology of particles and also crystallization time were highly depended on the contact area and contact time between CO_2 gas and the $Ca(OH)_2$ liquid. Different parameters were studied in the designed semi-batch bubble reactor to optimizing of stable nano calcite particles.

The individual calcite particles were produced in sizes between 150- 200 nm range with longer crystallization durations by the small interactions of gas-liquid reactants when the reaction rate was lower. Also, hollow calcite particles were obtained in the newly designed bubble reactor. Elongated chain-like particles were formed with shorter crystallization times due to aggregation of particles of about 50 nm in size. The aggregated particles were separated by pulsation method as the CO_2 was injected into the tank in certain time interval and waited for another time interval in order to stabilize the precipitated calcite particles in the reactor. The aggregation problem of smaller particles was also eliminated by removing of particles from jet flow in the slurry. Hollow nano calcite particles were thus produced by the jet flow assembly in the semi-batch bubble reactor was in the range of 150 nm.

Zeta potential values, which give information about the aggregation of particles, were above the +30 mV at the early stage of crystallization. When the crystallization was close to completion, zeta potential decreased to slightly below +30 mV levels. The average particle sizes were measured relatively higher before the CO_2 injection starts due to probably impurities from $Ca(OH)_2$ purchased. When the CO_2 was injected into the $Ca(OH)_2$ solution, initial particles formed were smaller. As the crystallization

progressed, particle sizes measured became bigger, however, the SEM images showed relatively smaller particles. The difference in particle size obtained between DLS measurements and SEM images was thought to come from slight aggregation among particles during the DLS measurements. SEM pictures showed some aggregated particles, but it must be kept in mind that some particles could naturally be aggregated during drying, before the SEM images were taken, due to creation of high forces between particles.

Effects of Na^+ ions were studied to stabilize the produced nano calcite particles and inhibit the aggregation between the particles in solution. High amount of NaCl helped to produce almost mono-dispersed calcite particles, although further study should be conducted for characterization of the system.

A simple $CaCO_3$ formation mechanism was proposed based on the experimental results. The formation of nano calcite particles starts with the formation of spindle-like particles in solution by attachment of ions to form clusters. Then, these clusters were aggregated into rice-like shape. As the crystallization progressed, the highly energetic ends were dissolved in solution and hollow nano calcite particles were formed. At the late stage of crystallization, the hollow particles were filled by dissolution recrystallization mechanism deformations were observed on particles when the pH was reduced to 7 at the very end of crystallization. By designing the semi-batch bubble reactor, hollow nano calcite particles were achieved to produce with almost homogeneous size distribution.

REFERENCES

Ariyaprayoon, J., leela-Adisorn, U., & Supsakulchaı, A. (2009). <Crystal Habit of CaCO3 Under Different Carbonation Methods>. *Journal of Metals, Materials and Minerals, 19*(2), 67-72.

Aylward;, G. H., Findlay;, T. J. V., Findlay;, T., & Aylward, G. (1999). *SI Chemical Data, 4th Edition*: Wiley.

Bastakoti, B. P., Guragain, S., Yokoyama, Y., Yusa, S., & Nakashima, K. (2011). Synthesis of hollow CaCO3 nanospheres templated by micelles of poly(styrene-b-acrylic acid-b-ethylene glycol) in aqueous solutions. *Langmuir, 27*(1), 379-384.

Bots, P., Benning, L. G., Rodriguez-Blanco, J.-D., Roncal-Herrero, T., & Shaw, S. (2012). Mechanistic Insights into the Crystallization of Amorphous Calcium Carbonate (ACC). *Crystal Growth & Design, 12*(7), 3806-3814.

Casanova, H., & Higuita, L. P. (2011). Synthesis of calcium carbonate nanoparticles by reactive precipitation using a high pressure jet homogenizer. *Chemical Engineering Journal, 175*, 569-578.

Chen, C. Y., Xia, M. Z., & Wang, F. Y. (2010). Influence of Three Organic Phosphonates on Calcite Crystal Growth. *Advanced Materials Research, 154-155*, 437-442.

Chen, J.-F., Wang, Y.-H., Guo, F., Xin-Ming, & Zheng, C. (2000). <Synthesis of Nanoparticles with Novel Technology: High-Gravity Reactive Precipitation>. *Industrial Engineering Chemical Research, 39*, 948-954.

Chen, X., Zhu, Y., Guo, Y., Zhou, B., Zhao, X., Du, Y., Wang, Z. (2010). Carbonization synthesis of hydrophobic CaCO3 at room temperature. *Colloids and Surfaces A: Physicochemical and Engineering Aspects, 353*(2-3), 97-103.

Cho, K., Chang, H., Kil, D. S., Kim, B.-G., & Jang, H. D. (2009). Synthesis of dispersed CaCO3 nanoparticles by the ultrafine grinding. *Journal of Industrial and Engineering Chemistry, 15*(2), 243-246.

Domingo, C., Loste, E., Gómez-Morales, J., García-Carmona, J., & Fraile, J. (2006). Calcite precipitation by a high-pressure CO2 carbonation route. *The Journal of Supercritical Fluids, 36*(3), 202-215.

Faatz, M., Gröhn, F., & Wegner, G. (2005). Mineralization of calcium carbonate by controlled release of carbonate in aqueous solution. *Materials Science and Engineering: C, 25*(2), 153-159.

Fakhrullin, R. F., Bikmullin, A. G., & Nurgaliev, D. K. (2009). Magnetically responsive calcium carbonate microcrystals. *ACS Appl Mater Interfaces, 1*(9), 1847-1851.

Flaten, E. M., Seiersten, M., & Andreassen, J.-P. (2010). Induction time studies of calcium carbonate in ethylene glycol and water. *Chemical Engineering Research and Design, 88*(12), 1659-1668.

Fu, S.-Y., Feng, X.-Q., Lauke, B., & Mai, Y.-W. (2008). Effects of particle size, particle/matrix interface adhesion and particle loading on mechanical properties of particulate–polymer composites. *Composites Part B: Engineering, 39*(6), 933-961.

Gao, Y., Liu, L., & Zhang, Z. (2009). <Mechenical Performance of Nano-CaCO3 Filled Polystyrene Composites>. *Acta Mechanica Solida Sinica, 22*(6), 554-562.

García-Carmona, J., Morales, J. G., & Clemente, R. R. g. (2003). Morphological control of precipitated calcite obtained by adjusting the electrical conductivity in the Ca(OH)2–H2O–CO2 system. *Journal of Crystal Growth, 249*(3-4), 561-571.

García Carmona, J., Gómez Morales, J., & Rodríguez Clemente, R. (2003). Rhombohedral–scalenohedral calcite transition produced by adjusting the solution electrical conductivity in the system Ca(OH)2–CO2–H2O. *Journal of Colloid and Interface Science, 261*(2), 434-440.

Gebauer, D., Volkel, A., & Colfen, H. (2008). Stable prenucleation calcium carbonate clusters. *Science, 322*(5909), 1819-1822.

Gu, W., Bousfield, D. W., & Tripp, C. P. (2006). Formation of calcium carbonate particles by direct contact of Ca(OH)2 powders with supercritical CO2. *Journal of Materials Chemistry, 16*(32), 3312.

Guo, H., Yu, J., & Cheng, B. (2006). Preparation and formation mechanism of wood-block-like calcite particles. *Journal of Solid State Chemistry, 179*(8), 2547-2553.

Hadiko, G., Han, Y. S., Fuji, M., & Takahashi, M. (2005). Synthesis of hollow calcium carbonate particles by the bubble templating method. *Materials Letters, 59*(19-20), 2519-2522.

Hadiko, G., Han, Y. S., Fuji, M., & Takahashi, M. (2006). Effect of Magnesium Ion on the Precipitation of Hollow Calcium Carbonate by Bubble Templating Method. *Key Engineering Materials, 317-318*, 65-68.

Hari, B., Ding, X., Guo, Y., Deng, Y., Wang, C., Li, M., & Wang, Z. (2006). Multigram scale synthesis and characterization of monodispersed cubic calcium carbonate nanoparticles. *Materials Letters, 60*(12), 1515-1518.

Hu, L., Dong, P., & Zhen, G. (2009). Preparation of active CaCO3 nanoparticles and mechanical properties of the composite materials. *Materials Letters, 63*(3-4), 373-375.

Ibrahim, A.-R., Vuningoma, J. B., Hu, X., Gong, Y., Hua, D., Hong, Y., Li, J. (2012). High-pressure gas–solid carbonation route coupled with a solid ionic liquid for rapid synthesis of rhombohedral calcite. *The Journal of Supercritical Fluids, 72*, 78-83.

Jiang, J., Liu, J., Liu, C., Zhang, G., Gong, X., & Liu, J. (2011). Roles of oleic acid during micropore dispersing preparation of nano-calcium carbonate particles. *Applied Surface Science, 257*(16), 7047-7053.

Jung, W. M., Kang, S. H., Kim, W.-S., & Choi, C. K. (2000). <Particle Morphology of Calcium Carbonate Precipitated by gas-liquid reaction in Couette-Taylor reactor>. *Chemical Engineering Science, 55*, 733-747.

Kadota, K., Yamamoto, T., Shimosaka, A., Shirakawa, Y., Hidaka, J., & Kouzu, M. (2011). Aggregation modeling of calcium carbonate particles by Monte Carlo simulation. *Journal of Nanoparticle Research, 13*(12), 7209-7218.

Kang, S. H., Hirasawa, I., Kim, W. S., & Choi, C. K. (2005). Morphological control of calcium carbonate crystallized in reverse micelle system with anionic surfactants SDS and AOT. *J Colloid Interface Sci, 288*(2), 496-502.

Kim, J. H., Ahn, J. W., Ko, S. J., Park, W. K., & Han, C. (2006). Inhibition Mechanism of Magnesium Ion on Carbonation Reaction with Ca(OH)₂ and CO₂. *Materials Science Forum, 510-511*, 990-993.

Konopacka-łyskawa, D., & Lackowski, M. (2011). Influence of ethylene glycol on CaCO3 particles formation via carbonation in the gas–slurry system. *Journal of Crystal Growth, 321*(1), 136-141.

Kontrec, J., Ukrainczyk, M., Babić-Ivančić, V., & Kralj, D. (2011). Synthesis of Calcium Carbonate by Semicontinuous Carbonation Method in the Presence of Dextrans. *Croatica Chemica Acta*, 25-32.

Lam, T. D., Hoang, T. V., Quang, D. T., & Kim, J. S. (2009). Effect of nanosized and surface-modified precipitated calcium carbonate on properties of CaCO3/polypropylene nanocomposites. *Materials Science and Engineering: A, 501*(1-2), 87-93.

Lieth, I. (1977). *Preparation and Crystal Growth of Materials with Layered Structures*. Holland: Kluwer Academic Publisher.

Lin, R.-y., Zhang, J.-y., & Bai, Y.-q. (2006). Mass transfer of reactive crystallization in synthesizing calcite nanocrystal. *Chemical Engineering Science, 61*(21), 7019-7028.

Lin, Y., Chen, H., Chan, C.-M., & Wu, J. (2010). The toughening mechanism of polypropylene/calcium carbonate nanocomposites. *Polymer, 51*(14), 3277-3284.

Liu, Q., Wang, Q., & Xiang, L. (2008). Influence of poly acrylic acid on the dispersion of calcite nano-particles. *Applied Surface Science, 254*(21), 7104-7108.

Liu, X., Zhu, B., Shao, Y., & Yang, X. (2010). Control of morphology and structure of calcium carbonate crystals by heparin. *Chinese Science Bulletin, 55*(11), 1107-1111.

Liu, X., Zou, Y., Cao, G., & Luo, D. (2007). The preparation and properties of biodegradable polyesteramide composites reinforced with nano-CaCO3 and nano-SiO2. *Materials Letters, 61*(19-20), 4216-4221.

López-Arce, P., Gómez-Villalba, L. S., Martínez-Ramírez, S., Álvarez de Buergo, M., & Fort, R. (2011). Influence of relative humidity on the carbonation of calcium hydroxide nanoparticles and the formation of calcium carbonate polymorphs. *Powder Technology, 205*(1-3), 263-269.

López-Periago, A. M., Pacciani, R., García-González, C., Vega, L. F., & Domingo, C. (2010). A breakthrough technique for the preparation of high-yield precipitated calcium carbonate. *The Journal of Supercritical Fluids, 52*(3), 298-305.

Martos, C., Coto, B., Peña, J. L., Rodríguez, R., Merino-Garcia, D., & Pastor, G. (2010). Effect of precipitation procedure and detection technique on particle size distribution of CaCO3. *Journal of Crystal Growth, 312*(19), 2756-2763.

Matsumoto, M., Fukunaga, T., & Onoe, K. (2010). Polymorph control of calcium carbonate by reactive crystallization using microbubble technique. *Chemical Engineering Research and Design, 88*(12), 1624-1630.

Montes-Hernandez, G., Fernández-Martínez, A., Charlet, L., Tisserand, D., & Renard, F. (2008). Textural properties of synthetic nano-calcite produced by hydrothermal carbonation of calcium hydroxide. *Journal of Crystal Growth, 310*(11), 2946-2953.

Montes-Hernandez, G., & Renard, F. (2011). Co-utilisation of alkaline solid waste and compressed-or-supercritical CO2 to produce calcite and calcite/Se0 red nanocomposite. *The Journal of Supercritical Fluids, 56*(1), 48-55.

Osman, M. A., Atallah, A., & Suter, U. W. (2004). Influence of excessive filler coating on the tensile properties of LDPE–calcium carbonate composites. *Polymer, 45*(4), 1177-1183.

Plank, J., Hoffmann, H., Schölkopf, J., Seidl, W., Zeitler, I., & Zhang, Z. (2009). Preparation and Characterization of a Calcium Carbonate Aerogel. *Research Letters in Materials Science, 2009*, 1-3.

Qian, K., Shi, T., Tang, T., Zhang, S., Liu, X., & Cao, Y. (2010). Preparation and characterization of nano-sized calcium carbonate as controlled release pesticide carrier for validamycin against Rhizoctonia solani. *Microchimica Acta, 173*(1-2), 51-57.

Rodriguez-Blanco, J. D., Shaw, S., & Benning, L. G. (2008). How to make 'stable' ACC: protocol and preliminary structural characterization. *Mineralogical Magazine, 72*(1), 283-286.

Rodriguez-Blanco, J. D., Shaw, S., & Benning, L. G. (2011). The kinetics and mechanisms of amorphous calcium carbonate (ACC) crystallization to calcite, via vaterite. *Nanoscale, 3*(1), 265-271.

Rodriguez-Blanco, J. D., Shaw, S., Bots, P., Roncal-Herrero, T., & Benning, L. G. (2012). The role of pH and Mg on the stability and crystallization of amorphous calcium carbonate. *Journal of Alloys and Compounds, 536*, S477-S479.

Sahebian, S., Zebarjad, S. M., Khaki, J. V., & Sajjadi, S. A. (2009). The effect of nano-sized calcium carbonate on thermodynamic parameters of HDPE. *Journal of Materials Processing Technology, 209*(3), 1310-1317.

Sant'Anna, S. S. e., Souza, D. A. d., & Araujo, D. M. d. (2008). Physico-chemical Analysis of Flexible Polyurethane Foams Containing Commercial Calcium Carbonate. *Materials Research, 11*(4), 433-438.

Shan, D., Wang, Y., Xue, H., & Cosnier, S. (2009). Sensitive and selective xanthine amperometric sensors based on calcium carbonate nanoparticles. *Sensors and Actuators B: Chemical, 136*(2), 510-515.

Sonawane, S. H., Gumfekar, S. P., Kate, K. H., Meshram, S. P., Kunte, K. J., Ramjee, L., . . . Ashokkumar, M. (2010). Hydrodynamic Cavitation-Assisted Synthesis of Nanocalcite. *International Journal of Chemical Engineering, 2010*, 1-8.

Sonawane, S. H., Shirsath, S. R., Khanna, P. K., Pawar, S., Mahajan, C. M., Paithankar, V., . . . Kapadnis, C. V. (2008). An innovative method for effective micro-mixing of CO2 gas during synthesis of nano-calcite crystal using sonochemical carbonization. *Chemical Engineering Journal, 143*(1-3), 308-313.

Sun, B.-C., Wang, X.-M., Chen, J.-M., Chu, G.-W., Chen, J.-F., & Shao, L. (2011). Synthesis of nano-CaCO3 by simultaneous absorption of CO2 and NH3 into CaCl2 solution in a rotating packed bed. *Chemical Engineering Journal, 168*(2), 731-736.

Tai, C. Y., & Chen, C.-k. (2008). Particle morphology, habit, and size control of using reverse microemulsion technique. *Chemical Engineering Science, 63*(14), 3632-3642.

Tsutsumi, A., Nieh, J.-Y., & Fan, L.-S. (1991). <Role of Bubble Wake in Fine Particle Production of Calcium Carbonate in Bubble Column systems>. *Industrial Engineering Chemical Research, 30*, 2328-2333.

Ukrainczyk, M., Kontrec, J., Babić-Ivančić, V., Brečević, L., & Kralj, D. (2007). Experimental design approach to calcium carbonate precipitation in a semicontinuous process. *Powder Technology, 171*(3), 192-199.

Varma, S., Chen, P.-C., & Unnikrishnan, G. (2011). Gas–liquid reactive crystallization for the synthesis of CaCO3 nanocrystals. *Materials Chemistry and Physics, 126*(1-2), 232-236.

Wan, P., Zhao, Y., Tong, H., Yang, Z., Zhu, Z., Shen, X., & Hu, J. (2009). The inducing effect of lecithin liposome organic template on the nucleation and crystal growth of calcium carbonate. *Materials Science and Engineering: C, 29*(1), 222-227.

Wang, C., Piao, C., Zhai, X., Hickman, F. N., & Li, J. (2010). Synthesis and character of super-hydrophobic CaCO3 powder in situ. *Powder Technology, 200*(1-2), 84-86.

Wang, Q., Zhang, X., Dong, W., Gui, H., Gao, J., Lai, J., Qiao, J. (2007). Novel rigid poly(vinyl chloride) ternary nanocomposites containing ultrafine full-vulcanized powdered rubber and untreated nano-sized calcium carbonate. *Materials Letters, 61*(4-5), 1174-1177.

Watanabe, H., Mizuno, Y., Endo, T., Wang, X., Fuji, M., & Takahashi, M. (2009). Effect of initial pH on formation of hollow calcium carbonate particles by continuous CO2 gas bubbling into CaCl2 aqueous solution. *Advanced Powder Technology, 20*(1), 89-93.

Wen, Y., Xiang, L., & Jin, Y. (2003). Synthesis of plate-like calcium carbonate via carbonation route. *Materials Letters, 57*(16-17), 2565-2571.

Wolthers, M., Nehrke, G., Gustafsson, J. P., & Van Cappellen, P. (2012). Calcite growth kinetics: Modeling the effect of solution stoichiometry. *Geochimica et Cosmochimica Acta, 77*, 121-134.

Wu, G., Wang, Y., Zhu, S., & Wang, J. (2007). Preparation of ultrafine calcium carbonate particles with micropore dispersion method. *Powder Technology, 172*(2), 82-88.

Xu, Y., Wang, C. Y., & Li, J. (2010). Biomimetic Synthesis of Hydrophobic Calcium Carbonate Nanoparticles In Situ. *Advanced Materials Research, 113-116*, 807-810.

Yang, K., Yang, Q., Li, G., Sun, Y., & Feng, D. (2006). Morphology and mechanical properties of polypropylene/calcium carbonate nanocomposites. *Materials Letters, 60*(6), 805-809.

Yang, X., Xu, G., Chen, Y., Wang, F., Mao, H., Sui, W., . . . Gong, H. (2009). CaCO3 crystallization control by poly(ethylene oxide)–poly(propylene oxide)–poly(ethylene oxide) triblock copolymer and O-(hydroxy isopropyl) chitosan. *Journal of Crystal Growth, 311*(21), 4558-4569.

Ye, Y. Q., & Chen, X. M. (2011). The Role of Crystal Control Agent in the Formation of Needlelike Calcium Carbonate Nano Particles. *Advanced Materials Research, 236-238*, 2150-2159.

Yuan, Q., Yang, Y., Chen, J., Ramuni, V., Misra, R. D. K., & Bertrand, K. J. (2010). The effect of crystallization pressure on macromolecular structure, phase evolution, and fracture resistance of nano-calcium carbonate-reinforced high density polyethylene. *Materials Science and Engineering: A, 527*(24-25), 6699-6713.